Quantitative Prediction of Uranium Speciation and Amidoxime Binding in Seawater from Advanced Simulation Techniques

Final Report

Project Number: NEUP-15-8536
Federal Grant Number: DE-NE0008397
Project Period: 10/1/2015 – 9/30/2018

Principal Investigator: Prof. De-en Jiang
Graduate Students: Chad Priest (Ph.D.), Nicole Onishi (Ph.D.)
Postdoc: Dr. Bo Li
Assistant Project Scientist: Dr. Runhong Huang
Visiting Students: Weihong Wu, Jingwei Zhou

Department of Chemistry
University of California, Riverside, CA 92521

Collaborator: Dr. Linfeng Rao
Lawrence Berkeley National Laboratory

December 29, 2018

Table of Contents

List of Figures

List of Tables

Executive Summary

The goal of this project was to quantitatively predict stability of uranium species and thermochemistry of uranium binding with amidoxime ligands in realistic seawater conditions. The specific aims of the project were: (i) determine the stable species of uranium and its solvation structure in realistic seawater conditions; also speciation and solvation of uranium's major competing species in seawater, vanadium; (ii) accurately predict the free energies (and thereby stability constants) of binding between uranium and amidoxime; (iii) accurately predict the reaction enthalpies and entropies of binding between uranium and amidoxime as well as between vanadium and amidoxime.

Main results and conclusions are as follows. First-principles molecular dynamic simulations found that the structure of the $Ca_2UO_2(CO_3)_3$ complex is very stable and that one Ca ion binds to the center $UO_2(CO_3)_3^{4-}$ anion stronger than the other Ca ion. This finding suggests that using time-resolved EXAFS spectra may confirm the asymmetry in binding of the two Ca ions in the aqueous $Ca_2UO_2(CO_3)_3$ complex. To consider the common ions, solvation of the $Ca_2UO_2(CO_3)_3$ complex in seawater was simulated by classical molecular dynamics simulation. It was found that the structure of the $Ca_2UO_2(CO_3)_3$ complex is very stable in the model seawater. A Na^+ ion was found to be closely associated with the $Ca_2UO_2(CO_3)_3$ complex by indirectly interacting with one axial oxygen atom of the UO_2 group bridged by a water molecule. In addition, the Na^+ ion interacts closely with one Ca^{2+} ion than the other. The present simulations revealed the key role of common ions such as Na^+ in impacting the solvation, structure, and apparent charge of the $Ca_2UO_2(CO_3)_3$ complex in seawater. The sequential processes of UO_2^{2+} binding with the three CO_3^{2-} groups and the two Ca^{2+} ions in pure water and in 0.1 M NaCl were simulated by classical molecular dynamics with both the non-constrained brute-force approach and umbrella sampling. The simulated free energies show excellent agreement with the experiment. The coordination structures of $UO_2(CO_3)_3^{4-}$ and $CaUO_2(CO_3)_3^{2-}$ were found to be significantly affected by the presence of Na^+ ions, leading to a monodentate binding of a carbonate group to U and a water molecule entering the first coordination shell of U.

To shed light on the binding between uranyl and glutardiamidoxime (H_2B), an important model and state-of-the-art ligand for seawater uranium extraction, a suite of computational methods was employed. From molecular dynamics (MD) simulations, it was found that the binding configurations of B^{2-} with uranyl favor the twofold distorted η^2 binding between the oximate ends ($C=N-O^-$) and U, while HB^- prefers the chelating mode for the oximate end with the neutral end being solvated by water. The free energies of sequential ligand binding to form UO_2B, $[UO_2B_2]^{2-}$, and $[UO_2(HB)B]^-$ were simulated with umbrella sampling and very good agreement with the experimental values was achieved, which corroborates the structural insights into the binding mode. State-of-the-art polymeric sorbents employ both amidoximate and carboxylate groups on the side chains to achieve optimal U uptake and selectivity, so we simulated the binding of a model amidoximate–carboxylate bifunctional ligand with uranyl. Classical MD and free-energy simulations in 0.5 M NaCl showed that the carboxylate group binds first to uranyl, leading to a loose intermediate state, and then, the amidoximate group binds, resulting in a more stable and tight chelate state. Binding of the second bifunctional ligand follows a similar process, and the two ligands prefer a trans configuration around the uranyl group. The simulated free energies indicate that the two bifunctional ligands bind with uranyl 14 kcal/mol stronger than the two ligands with only amidoximate groups, confirming an important synergy between amidoximate and carboxylate groups in binding uranyl.

When amidoxime-containing sorbents are deployed in the seawater, the amidoxime ligands will displace carbonate groups in $Ca_2UO_2(CO_3)_3$. To simulate this process, classical molecular dynamics combined with umbrella sampling were used to map the free-energy profiles for the displacement of the three carbonates in $Ca_2UO_2(CO_3)_3$ by the simple acetamidoximate (AO^-) and the more complex glutardiamidoximate (B^{2-}/HB^-) ligands in the 0.5 M NaCl aqueous solution. It was found that the two Ca^{2+} ions in $Ca_2UO_2(CO_3)_3$ can greatly facilitate the displacement of the first two carbonate groups which leave as the neutral $Ca^{2+}\ldots CO_3^{2-}$ ion pairs. Displacing the last carbonate needs the help of an additional Ca^{2+} ion. The presence of the Na^+ ions also helps mediate the carbonate departure. The overall displacement reaction is endergonic up to 13 kcal/mol, depending on the number of carbonates to be displaced, the amidoxime ligand type, and the presence of the additional Ca^{2+} ion.

Vanadium is a main competitor of uranium in binding with the amidoxime ligands. To determine the enthalpic vs entropic contributions in affecting U/V selectivity, we investigated the temperature dependence of the binding of the amidoxime ligands with uranyl and vanadate. We found that the binding of amidoxime ligands with vanadate is not very sensitive to the temperature change, while the binding of amidoxime ligands with uranyl is. We have analyzed in detail the temperature effect on the thermodynamics of binding and determined enthalpy and entropy contributions to the binding free energy by fitting the data in the van't Hoff equation. We further compared the simulated enthalpies and entropies with the recently published experimental data from PNNL based on the ORNL sorbents. It was found that uranyl complexation with the open-chain amidoxime is endothermic and has a large positive entropy change, in very good agreement with the experiment for both AF1 and AI8 sorbents. In contrast, vanadate complexation with the open-chain amidoxime is slightly exothermic and has a smaller positive entropy change, in good agreement with the experiment for the AI8 sorbent but different from that for the AF1 sorbent. Hence, our work suggests that use of the open-chain amidoxime at higher temperatures is an excellent way to increase U/V selectivity.

Our work has shown that molecular dynamics simulations are a powerful tool to yield structural, thermodynamic, and mechanistic insights into uranyl-ligand binding in aqueous solutions. These insights are useful in identifying the binding sites and driving force for the uranyl extraction chemistry based on model ligands. However, the ligand structures and conformations on the realistic sorbents are still unclear and could be quite different from the small model ligands. One approach to bridge this gap is to use oligomeric ligands in the simulations that better mimic the realistic sorbents. The other important direction is to combine MD simulation data with the EXAFS data to elucidate the binding sites for uranyl in polymeric sorbents.

Publications from this Award

1. Priest, C.; Tian, Z. Q.; **Jiang, D. E.*** "First-principles molecular dynamics simulation of the $Ca_2UO_2(CO_3)_3$ complex in water", **Dalton Trans.**, 45, 9812–9819 (2016).

2. Yue, Y.*; Zhang, C.; Tang, Q.; Mayes, R. ; Liao, W. P.; Liao, C.; Tsouris, C.; Stankovich, J. Chen, J.; Hensley, D.; Abney, C.; **Jiang, D. E.***; Brown, S.; Dai, S.* "A Poly(acrylonitrile)-Functionalized Porous Aromatic Framework Synthesized by Atom-Transfer Radical Polymerization for Extraction of Uranium from Seawater", **Ind. Chem. Eng. Res.**, 55, 4125-4129 (2016).

3. Wu, W. H.; Priest, C.; Zhou, J. W.; Peng, C. J.; Liu, H. L.; **Jiang, D. E.*** "Solvation of the $Ca_2UO_2(CO_3)_3$ Complex in Seawater from Classical Molecular Dynamics", **J. Phys. Chem. B**, 120, 7227-7233 (2016).

4. Li, B.; Zhou, J.; Priest, C.; **Jiang, D. E.*** "Effect of Salt on the Uranyl Binding with Carbonate and Calcium Ions in Aqueous Solutions", **J. Phys. Chem. B**, 121, 8171–8178 (2017).

5. Priest, C.; Zhou, J.; **Jiang, D. E.*** "Solvation of the vanadate ion in seawater conditions from molecular dynamics simulations", **Inorg. Chim. Acta**, 458, 39–44 (2017).

6. Priest, C.; Li, B.; **Jiang, D. E.*** "Uranyl-Glutardiamidoxime Binding from First Principles Molecular Dynamics, Classical Molecular Dynamics, and Free-Energy Simulations", **Inorg. Chem.**, 56, 9497–9504 (2017).

7. Li, B.; Priest, C.; **Jiang, D. E.* "**Displacement of carbonates from $Ca_2UO_2(CO_3)_3$ by amidoxime-based ligands from free-energy simulations", **Dalton Trans.**, 47, 1604–1613 (2018).

8. Priest, C.; Li, B.; **Jiang, D. E.*** "Understanding the Binding of a Bifunctional Amidoximate-Carboxylate Ligand with Uranyl in Seawater", **J. Phys. Chem. B**, 122, 12060–12066 (2018)

In Preparation:

9. Li, B.; Priest, C.; **Jiang, D. E.*** "Molecular dynamics simulations of functionalized oligomers for uranium extraction from seawater", to be submitted to **Dalton Trans.**

1 Introduction

1.1 Uranium extraction from seawater

The sustainability of nuclear energy depends on a long-term, continuous supply of uranium for centuries to come. Seawater provides the ultimate resource and reassurance due to the vast amount of dissolved uranium (~4.5 billion tons), despite its low concentration (~3 ppb). Amidoxime has been the ligand of choice for uranium extraction from seawater from previous trial-and-error screening.[1,2] However, progress toward a molecular-level understanding of uranium speciation and ligand binding had been slow to develop. The situation changed early this decade, when strong support of research on uranium from seawater by the Nuclear Energy Office led to a deeper understanding of uranium speciation in seawater and its ligand-binding chemistry. For example, researchers have experimentally quantified uranium speciation in seawater conditions and the binding strength of U(VI) with various amidoxime ligands.[3-8] Importantly, it has been showed that the prevailing assumption that the $UO_2(CO_3)_3^{4-}$ complex is the dominant species in seawater may be incorrect; instead, the results suggest that it should be the neutral $Ca_2UO_2(CO_3)_3(aq)$ species due to the overwhelming abundance of Ca^{2+} ions in seawater.[8,9] This latest result indicates how little we know about uranium speciation in seawater and that one must take into account the complex compositions of seawater (such as high levels of Na^+, Cl^-, Mg^{2+}, and Ca^{2+}) in understanding uranium speciation and extraction. It also demands a molecular-level understanding of the relative stability of a highly charged species such as $UO_2(CO_3)_3^{4-}$ *vs.* a neutral $Ca_2UO_2(CO_3)_3(aq)$ in an aqueous electrolyte solution. Further, a computational approach to understanding uranium complexation is necessary for the rational design of improved ligands that will lead to economical uranium extraction from seawater. Previous molecular modeling of uranium extraction has been mainly based on geometry-directed ligand design and gas-phase binding energetics from density functional theory coupled with a continuum solvation model.[10-13] These studies have provided valuable insights into the bonding structure and energetics. However, without explicit solvent, common ions in the solution, or finite-temperature sampling of the solvation structure, these methods cannot provide quantitative prediction of the detailed mechanism and thermochemistry of uranium speciation and binding with amidoxime ligands in the marine environments.

1.2 Modeling seawater condition and free energy calculation

State-of-the-art simulation techniques including classical molecular dynamics (CMD) accelerated by graphical processor unit (GPU), first principle molecular dynamics (FPMD), and free-energy calculations are employed to explicitly include water molecules and common seawater ions (such as Na^+, Cl^-, Mg^{2+}, and Ca^{2+}) in the simulations. These advanced simulation techniques coupled with recent developments in computing hardware now allow one to examine detailed molecular mechanisms and to predict their thermochemistry in complex liquid environments. The association constants of the binding-unbinding processes are calculated from the potential of mean force (PMF) profiles in the free energy calculations.

CMD has been extensively used to understand the uranyl solvation problem in pure water environment. The advantage of CMD is its fast speed of calculating the atomic interactions from force field, which is fitted from the potential energy surface of high level of theory *ab initio* calculations. In order to simulate the seawater condition, thousands of water molecules are required to solvate the limit number of common ions in the simulation box and hundreds of nanoseconds simulation time is necessary to sample the ions association process in a brute force run. This

computation burden is greatly alleviated by employing the GPU-accelerated CMD software package such as AMBER. The disadvantage of CMD is that its accuracy is determined by the empirical description of atomic interaction potential. FPMD calculates the atomic interaction from quantum mechanics which is more accurate, but the higher level of theory also limits its application to simple aqueous solution involving a few hundreds of atoms. In the present work, we combine their advantage by using FPMD to validate our CMD results such as the stability of the binding configurations.

MD-based free energy simulations such as umbrella sampling have been widely used in biophysics and biochemistry. The advantage of this type of technique is its improvement of sampling a system where ergodicity is hindered by the form of the system's energy landscape. Therefore, it is more suitable than the popular approach using DFT with implicit solvation model to determine the free energy change of uranium species in seawater, which requires considering the change of hydrogen network and distribution of the common ions.

Our present work is the first combination of the advantages of CMD, FPMD and MD-based free energy calculations to understand the molecular mechanisms of uranium extraction from seawater by targeting a quantitative prediction of the binding thermochemistry. Experimental measurements are also used to validate and improve our predictions in all the three objectives of this project, so that a computational protocol will be established to predict binding free energies for new ligands.

1.3 Project specific aims and tasks

The goal of this project was to quantitatively predict stability of uranium species and thermochemistry of uranium binding with amidoxime ligands in realistic seawater conditions. The **specific aims** of the project were: (i) determine the stable species of uranium and its solvation structure in realistic seawater conditions; also speciation and solvation of uranium's major competing species in seawater, vanadium; (ii) accurately predict the free energies (and thereby stability constants) of binding between uranium and amidoxime; (iii) accurately predict the reaction enthalpies and entropies of binding between uranium and amidoxime as well as between vanadium and amidoxime.

Using first principles and molecular mechanical approaches coupled with molecular dynamics and free energy calculations at experimental conditions, we carried out the following tasks and accomplished our specific aims:

Task 1. Determine stable speciation of uranium (VI) (Ch. 2, Ch. 3, and Ch.4) and vanadium (V) (Ch. 8) in seawater conditions with explicit water solvation and Na^+/Cl^- ions.

Task 2. Simulate the binding free energy and binding constant between the determined stable U(VI)/V(V) species with various amidoxime ligands (Ch. 5, Ch. 6, and Ch. 7)

Task 3. Compute entropies and enthalpies of uranium/vanadium binding with amidoxime ligands to dissect the role of enthalpy vs. entropy in dictating U/V selectivity (Ch. 9).

2 First-principles Molecular Dynamic Simulation of the $Ca_2UO_2(CO_3)_3$ Complex in Water

2.1 Introduction

In this chapter we studied the fundamentals about the structure of uranium complex in water. In aqueous solution, uranium exists as the stable oxocation with an oxidation state of U(VI), called uranyl – UO_2^{2+}. Early work has focused on prying into the prominent equilibrium species bound to uranyl complex in seawater[14] and suggested the anionic $[UO_2(CO_3)_3]^{4-}$ complex to be the dominant species in seawater. However, over the past two decades experimental data has shifted the consensus to cation-balanced complexes.[8,9,15-17] Concentrations of magnesium (Mg^{2+}) and calcium (Ca^{2+}) in seawater are overwhelmingly larger than the concentration of U(VI), so the ternary Ca-UO_2-CO_3 or Mg-UO_2-CO_3 exists predominately in seawater. The complexation of Ca^{2+} with $[UO_2(CO_3)_3]^{4-}$ has been validated experimentally by Bernhard et al.[16] and Kelly et al.[17] with extended X-ray absorption fine structure (EXAFS) spectroscopy. Most recently, Rao et al.[9] examined the thermodynamics of uranium in seawater and the complexation between Ca/Mg and $[UO_2(CO_3)_3]^{4-}$. They concluded that in seawater pH (8.2) $Ca_2UO_2(CO_3)_3$ accounts for 58% of the total uranium in the solution while $CaUO_2(CO_3)_3^{2-}$ and $MgUO_2(CO_3)_3^{2-}$ account for 18% each and $[UO_2(CO_3)_3]^{4-}$ accounts for only 6%.[9] In addition, Rao et al. studied binding of U(VI) with various types of ligands and the subsequent leaching process.[5-7,18-20] In addition, the stability constant for the speciation of calcium is larger than magnesium.[9]

On the theoretical and computational side, work has been done on the binding of UO_2^{2+} with ligands using a cluster model[7,10-12,21] and on the structure and dynamics of $[UO_2(CO_3)_3]^{4-}$ in aqueous environment using molecular dynamic simulations (MD).[22-25] Hofer et al. examined the structure and dynamics of $[UO_2(CO_3)_3]^{4-}$ in water using quantum mechanical charge field molecular dynamics (QMCF-MD).[22,23] Kerisit et al. investigated the structure and dynamics of $Ca_2UO_2(CO_3)_3$ in aqueous solution with classical MD simulations based on non-polarizable force fields.[24] Given the highly charged nature of Ca^{2+} ions and $[UO_2(CO_3)_3]^{4-}$, polarization may be important in describing the interaction between Ca^{2+} ions and $[UO_2(CO_3)_3]^{4-}$ and between the complex and the water molecules. First principles MD at the electronic structure would be desirable, as the polarization effect is taken into account automatically. However, no such work has been done on $Ca_2UO_2(CO_3)_3$ in aqueous solution, to the best of our knowledge.

The present work seeks to describe the structure and solvation of $Ca_2UO_2(CO_3)_3$ in water using first principles MD based on density functional theory (DFT-MD for short) for the first time. Our goal is to provide a fundamental baseline understanding of the structure and solvation of $Ca_2UO_2(CO_3)_3$ in water in terms of Ca-$UO_2(CO_3)_3$ and Ca-water interactions. The other goal is to compare with the previous EXAFS data and classical MD simulations.

2.2 Computational methods

First-principles molecular dynamic simulations based on density functional theory (DFT-MD) and Born–Oppenheimer approximation was carried out using Vienna Ab-initio simulation package with plane wave basis and periodic boundary conditions.[26,27] The Kohn-Sham equations are solved with the all-electron projected augmented wave (PAW) method.[28,29] We have chosen the Perdew-Burke-Ernzerhof (PBE) functional of the generalized-gradient approximation (GGA) for electron exchange and correlation.[30] PBE is one of the most popular GGA functionals, providing a balanced description for diverse molecules and materials, instead of being designed for a special class of molecules or interactions. In the case of liquid water, it has been shown that the PBE functional can describe well the peak positions in the radial distribution functions of g_{OO} and g_{OH} for the liquid structure of water but it overestimates the peak heights, in comparison with

the experiment, leading to over-structuring.[31,32] Using hybrid functionals together with van der Waals interactions can soften the water structure, giving a better agreement with the experiment. But hybrid functionals are usually about two orders of magnitude more expensive than a pure DFT method such as GGA-PBE. We think that PBE is a reasonable choice in balancing accuracy and efficiency.

The MD calculations were carried out at 298 K in a canonical NVT ensemble for a periodic cubic box that contains one $Ca_2UO_2(CO_3)_3$ complex in a fixed number of water molecules. Three concentrations were examined: 0.53 M, 0.43 M, and 0.36 M, corresponding to one $Ca_2UO_2(CO_3)_3$ complex in a periodic box containing 100, 125, and 150 water molecules, respectively; the corresponding simulation box sizes and densities are also compared in Table 1. Here we note that since there is only one complex in the simulation box for the three concentrations, this approach cannot probe the correlations between complexes but severs more to test the potential presence of size artifacts. We determined the densities from constant-pressure classical MD simulations using force-field parameters from a previous study.[24] The temperature was kept constant via Nose-Hoover thermostat. A Verlet algorithm was used to integrate Newton's equation of motion with a time step of 1 femtosecond. After equilibration at 298 K for 15 ps, another 15 ps of production run was followed. Graphical visualization and analysis of the liquid structure packing of the uranium complex was examined with VMD.[33]

Table 2-1 Three concentrations of $Ca_2UO_2(CO_3)_3$, the corresponding water molecules in the simulation boxes, the box sizes, and the densities, examined in the present work.

Concentration (M)	Water Molecules	Simulation Box Size (Å)	Density (g/cm^3)
0.36	150	17.5	1.14
0.43	125	16.7	1.17
0.53	100	15.7	1.21

2.3 Results and discussion

2.3.1 Interaction between calcium and carbonate

The most important structural feature of the $Ca_2UO_2(CO_3)_3$ species is the binding between the two Ca ions and the $[UO_2(CO_3)_3]^{4-}$ ion. This interaction is mediated by the carbonate groups. As shown in Fig. 1, the three carbonate groups bind to the uranyl group on the equatorial plane in a bidentate mode; this structural model has been established from the crystal structure of the naturally occurring mineral Liebigite $[Ca_2UO_2)(CO_3)_3{\cdot}11H_2O]$,[34] fitting of the EXAFS data,[16,17] and quantum mechanical modeling.[21] There are three different oxygens in the uranium complex: the two axial oxygens (O_{ax}) triple-bonded to U in the uranyl structure,[35] six equatorial carbonate oxygens (O_{eq}) that are bonded to U, and three distal carbonate oxygens (O_{dis}) not directly interacting with U. The two Ca^{2+} ions bind to the carbonate groups on the same plane; each Ca^{2+} ion binds to two equatorial oxygen atoms from two neighboring carbonate groups. In our DFT-MD simulations, interaction of the Ca ions to the $[UO_2(CO_3)_3]^{4-}$ complex was monitored by the four Ca-O_{eq} distances (dashed lines in Fig. 1): Ca1-O1, Ca1-O2, Ca2-O3, and Ca2-O4.

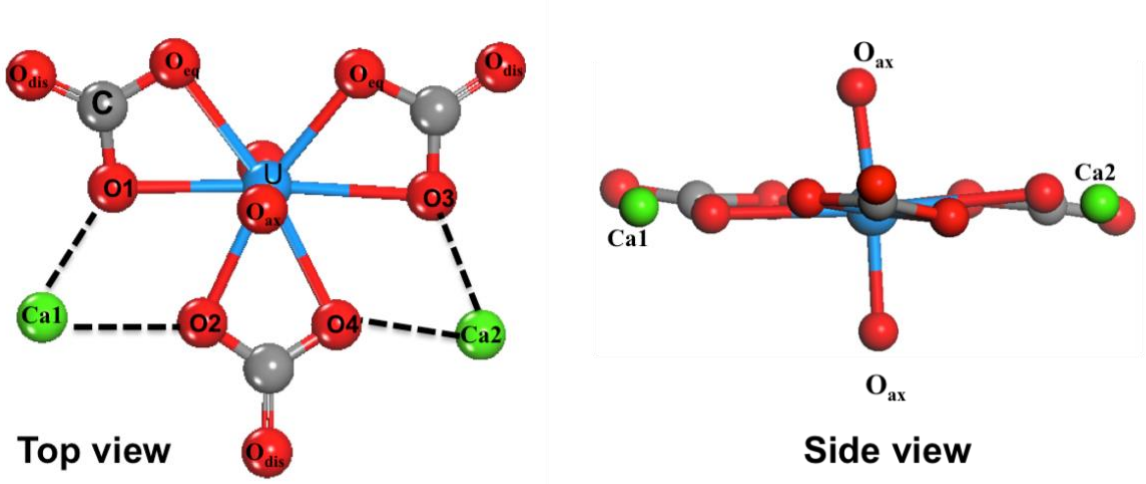

Figure 2-1 Top view and side view of the $Ca_2UO_2(CO_3)_3$ complex in water.

We placed an initial structure of the uranium complex as shown in Figure 2-1 into a periodic water box at a concentration of 0.53 M. After equilibration at 298 K, a production run of 15 ps was used for statistical analysis. Figure 2-2 shows the four Ca-O_{eq} distances during the 15 ps production trajectory. One can see that Ca1-O1 and Ca1-O2 distances exhibit fluctuations around 2.45-2.50 Å (Figure 2-2a), while Ca2-O3 and Ca2-O4 around 2.35-2.40 Å (Figure 2-2b). So in our simulation timeframe, the $Ca_2UO_2(CO_3)_3$ complex is very stable and maintains steady Ca-O_{eq} distances about 2.45 Å with a standard deviation of about 0.12 Å. Another important observation is that there is asymmetry between the two Ca ions: Ca2 binds to $[UO_2(CO_3)_3]^{4-}$ stronger than Ca1, as evidenced by the shorter average Ca2-O_{eq} distance (2.37 Å; Figure 2-2b) than Ca1-O_{eq} (2.47 Å; Figure 2-2a). Here we note that initially, we placed the $Ca_2UO_2(CO_3)_3$ complex randomly inside a water box. To test the robustness of the asymmetric structure, we tried several different initial configurations of water solvation around the $Ca_2UO_2(CO_3)_3$ complex and found that they always equilibrated to the asymmetric configuration after about 5 ps.

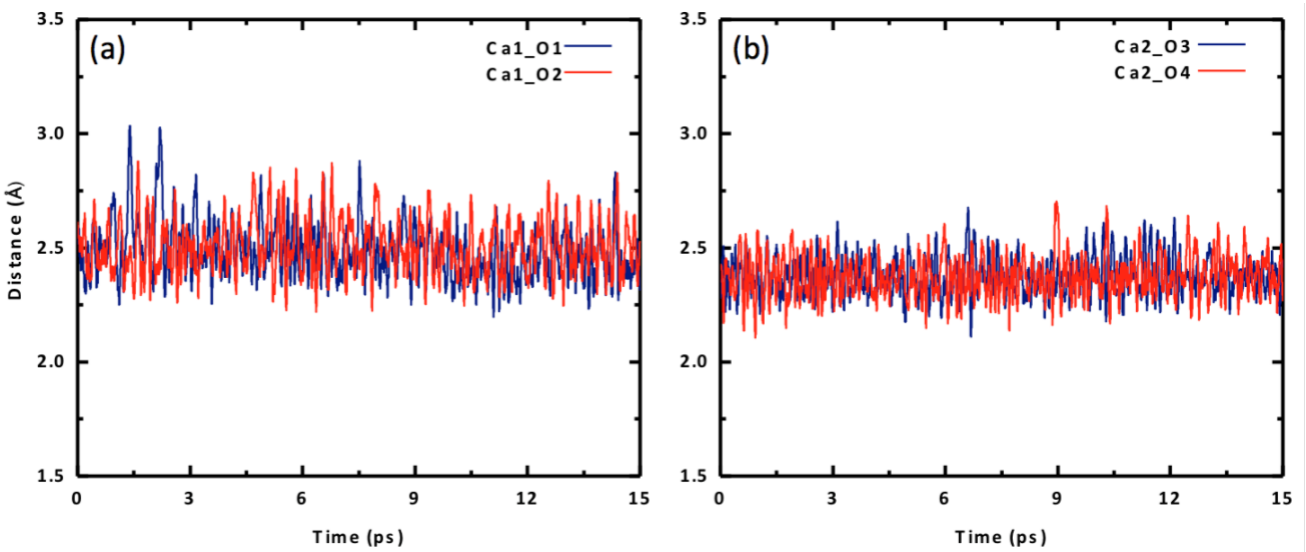

Figure 2-2 Change of Ca-O distances with time for the $Ca_2UO_2(CO_3)_3$ complex in water (0.55 M): (a) Ca1-O1 and Ca1-O2; (b) Ca2-O3 and Ca2-O4. See **Figure 2-1** for atom labels.

To further examine the difference between the two Ca ions, we plot the radial distribution function (RDF) of carbonate O_{eq} atoms around each of the two Ca ions in Fig. 3. One can see that the stronger binding Ca^{2+} has a narrower and higher O_{eq} distribution (Fig. 3b), while the weaker Ca^{2+} has a broader and lower O_{eq} distribution (Fig. 3a). In addition, there is a slight difference between the two O_{eq} atoms binding to each Ca^{2+}. For Ca1, Ca1-O1 is slightly shorter than Ca1-O2; for Ca2, Ca2-O3 is slightly shorter than Ca2-O4.

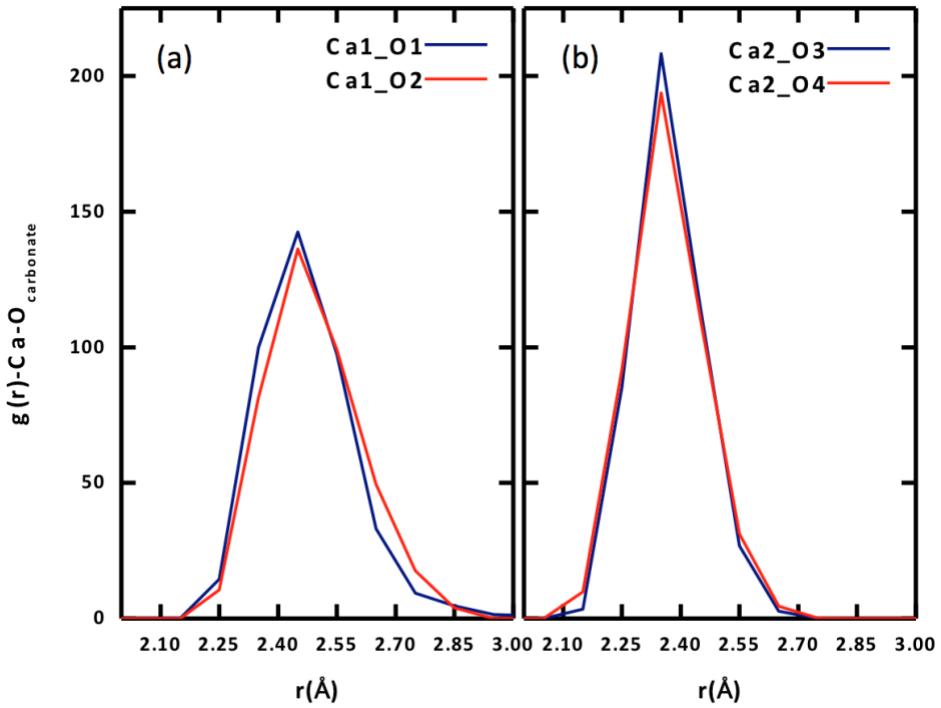

Figure 2-3 Radial distribution functions of equatorial carbonate oxygen (O_{eq}) around each Ca ion of the $Ca_2UO_2(CO_3)_3$ complex in water (0.55 M): (a) Ca1; (b) Ca2. See **Figure 2-1** for atom labels.

To confirm the stability of the $Ca_2UO_2(CO_3)_3$ complex and the asymmetry of the two Ca^{2+} ions, we further simulated two lower concentrations (0.43 M and 0.36 M) and found the same conclusions. The $Ca_2UO_2(CO_3)_3$ complex in the two lower concentrations is also stable in our simulation timeframe, as shown by the steady maintaining of the binding of the two Ca^{2+} ions with the $[UO_2(CO_3)_3]^{4-}$ complex. More interestingly, we found that the asymmetry between the two Ca^{2+} ions also persists in the two lower concentrations, indicating that this is likely an intrinsic feature of the $Ca_2UO_2(CO_3)_3$ complex in water. Figure 2-4 displays the four Ca-O_{eq} distances as a function of the U concentration. Both the asymmetry between the two Ca^{2+} ions and the small difference between the two O_{eq} atoms for each Ca^{2+} ions are evident.

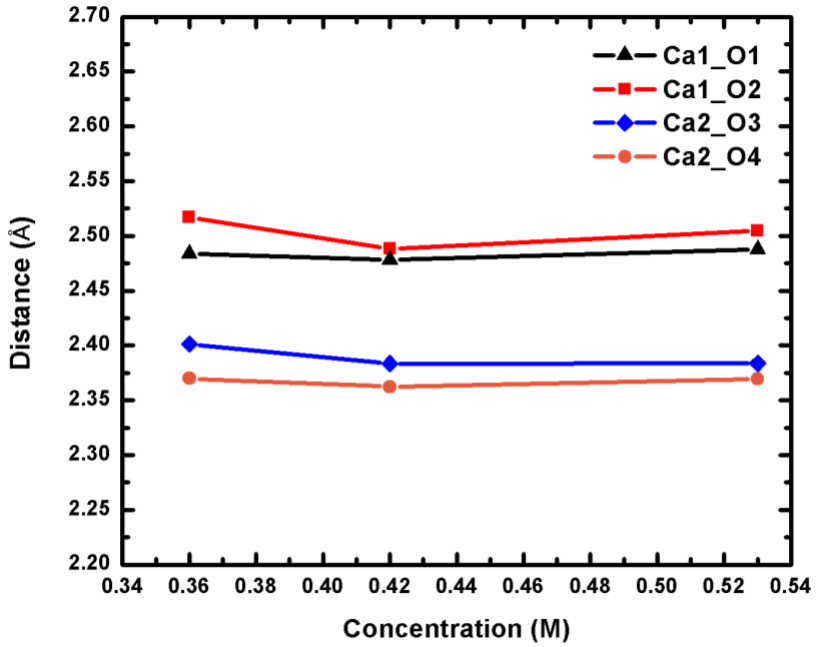

Figure 2-4 Change of the four Ca-O_{eq} distances of the $Ca_2UO_2(CO_3)_3$ complex in water at three different concentrations. See Figure **2-1** for atom labels. The distances are averages over 15ps trajectories

2.3.2 Interaction between calcium and water

The interaction between calcium and carbonate in the $Ca_2UO_2(CO_3)_3$ complex is the most important information that we obtained from our DFT-MD simulations. The asymmetry between the two Ca^{2+} ions must be closely related to the water molecules around the $Ca_2UO_2(CO_3)_3$ complex. We now analyze the interaction between the two Ca^{2+} ions and the water molecules. Figure 2-5 shows radial distribution functions (RDFs) of oxygen atoms from the water molecules around the two Ca^{2+} ions both separately and together. One can see that the solvation shell around Ca1 has an average Ca-O_{water} distance of 2.45 Å (with a standard deviation of 0.12 Å) and the integrated RDF (with a cutoff at 3.0 Å) gives coordination number of five; in other words, there are five molecules around Ca1 in addition to the two O_{eq} atoms from two carbonate groups. On the other hand, Ca2 has four water molecules in the solvation shell with an average Ca-O_{water} distance of 2.35 Å (with a standard deviation of 0.09 Å). So together, the average coordination number of the two Ca^{2+} ions is 4.5 in terms of water molecules. We further examined the RDF of water oxygens around Ca^{2+} ions for the two lower concentrations and found the same trend of five water molecules around Ca1 and four water molecules around Ca2. In comparison, previous classical MD simulations predicted that both calcium ions have five water molecules in the first hydration shell,[24] similar to the case of Ca1 in our simulation.

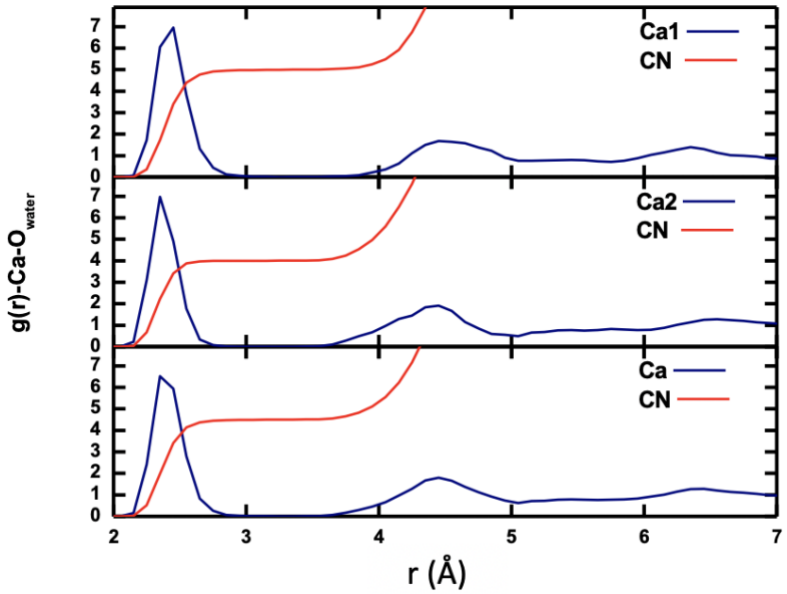

Figure 2-5 Radial distribution function (blue) and its integration (coordination number, CN; red) of water oxygen atoms around Ca1 and Ca2 separately (top two panels) and together (bottom panel), for 0.55 M $Ca_2UO_2(CO_3)_3$ in water.

2.3.3 Solvation environments of the two calcium ions

From the discussion of the $Ca_2UO_2(CO_3)_3$ complex in water above, we can clearly see that the difference between the two Ca ions is reflected in both the Ca-carbonate and the Ca-water interactions. The two interactions are in fact correlated: Ca1 has weaker binding with the $[UO_2(CO_3)_3]^{4-}$ complex, five molecules in the solvation shell, and a total of seven coordination bonds; Ca2 has stronger binding with the $[UO_2(CO_3)_3]^{4-}$ complex, four molecules in the solvation shell, and a total of six coordination bonds. Ca2 has a tighter solvation shell, so both average Ca2-O_{water} and Ca2-$O_{carbonate}$ distances are shorter than Ca1-O_{water} and Ca1-$O_{carbonate}$ distances, respectively.

What causes the asymmetry of binding and solvation between the two Ca ions in the $Ca_2UO_2(CO_3)_3$ complex? To answer this question, we analyzed the solvation environment of the complex from the views of Ca-carbonate, Ca-water, and carbonate-water interactions together, as shown in Figure 2-6. One can see that there are three water molecules in the equatorial plane coordinating to Ca2, instead of two in the case of Ca1. The reason why Ca2 can have one more water in the equatorial plane is that two of the three water molecules (water1 and water2 in Figure 2-6) are interacting with both Ca1 and the carbonates. From Fig. 6, one can see that both water1 and water2 form hydrogen bonding (hb1 and hb2) with the two distal oxygen atoms of the two carbonate groups. These two hydrogen bonds pull water1 and water2 closer to the $Ca_2UO_2(CO_3)_3$ complex, thereby leaving space for a third water molecule to enter the equatorial plane. In other words, it is the hydrogen-bonding network around the $Ca_2UO_2(CO_3)_3$ complex that leads to the difference in solvation and binding between the two Ca ions. We further examined the two lower concentrations and found the same solvation environment around the $Ca_2UO_2(CO_3)_3$ complex that confirmed the role of the hydrogen-bonding network in differentiating the two Ca ions in the $Ca_2UO_2(CO_3)_3$ complex.

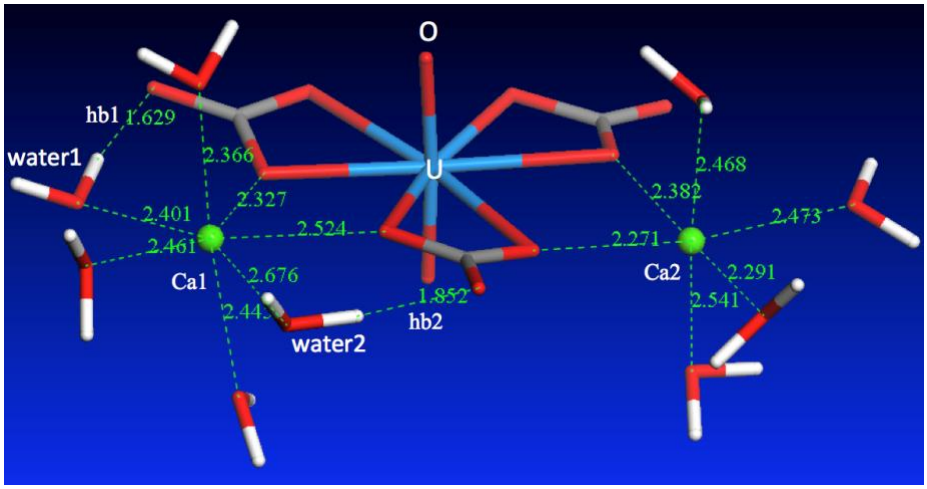

Figure 2-6 A snapshot of the $Ca_2UO_2(CO_3)_3$ complex in water at 0.53 M, showing only the water molecules directly interacting with the two Ca ions; hb1 and hb2 denote hydrogen bonding between the two water molecules (water1 and water2) and the two distal oxygen atom.

To further explain the asymmetry between the two Ca ions, we added a schematic drawing (Figure 2-7) of the equatorial plane around U. One can see that Ca1 is coordinated by both water1 (W1) and water2 (W2), while W1 is hydrogen bonded to O5 of carbonate1 (C1) and W2 is hydrogen bonded to O6 of carbonate2 (C2). As a result, the hydrogen bonding pulls the two carbonate groups closer (indicated by the two black arrows), so Ca1 is "squeezed" a little further away from O1 and O2. On the other hand, the O3-U-O4 angle becomes wider (indicated by the red double arrow), thereby allowing Ca2 to come closer to O3 and O4. Another way to think about this is via carbonate1. If Ca1 and Ca2 were symmetric in binding, the hydrogen bonding around carbonate1 (C1) would be symmetric. But as shown in Figure 2-7, the hydrogen bonding around carbonate-1 is asymmetric that eventually leads to the asymmetry in binding between Ca1 and Ca2.

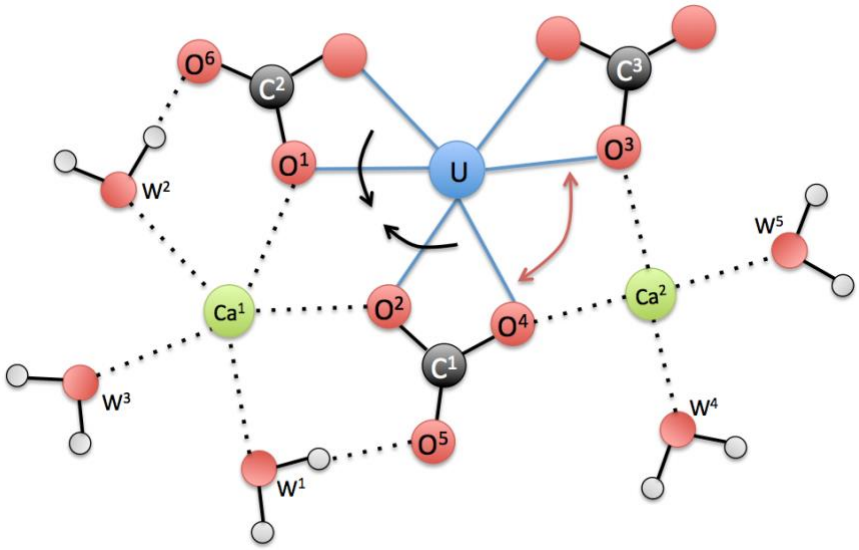

Figure 2-7 A schematic view of the equatorial plane around U for the $Ca_2UO_2(CO_3)_3$ complex in water. W stands for water.

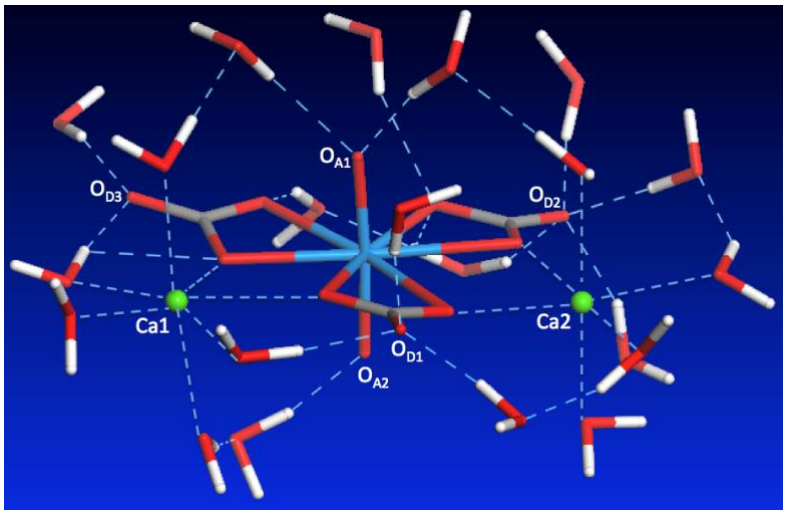

Figure 2-8 A snapshot of the first solvation shell of water molecules around the $Ca_2UO_2(CO_3)_3$ complex.

2.3.4 Solvation environments of the whole complex

The discussion above shows the importance of the hydrogen-bonding network in dictating the complex geometry. To further analyze this network, we examined the first solvation shell of the whole complex, namely, the water molecules in direct interaction with the complex. Since we have analyzed the water solvation around the two Ca ions, here we focus our discussion on the carbonate and uranyl oxygens. One can see from Figure 2-8 that the top uranyl oxygen (O_{A1}) has two water molecules hydrogen-bonded to it, while the bottom uranyl oxygen (O_{A2}) has one. Moreover, one can see strong solvation of the carbonate distal oxygens by water: O_{D1} is hydrogen-bonded by three water molecules, O_{D2} by four, O_{D3} by two. In addition, the two carbonate equatorial oxygens not interacting with the Ca ions are also solvated by water. Together with the water molecules around the two Ca ions, we found that there are 21 molecules in the first solvation shell. This large solvation shell indicates the necessity of using explicit solvation model to address structure, thermodynamics, and chemistry of the aqueous $Ca_2UO_2(CO_3)_3$ complex.

2.3.5 Ca-U distances

Besides speciation studies based on thermodynamics,[8,9,16] the most direct characterization of the $Ca_2UO_2(CO_3)_3$ complex in water has been EXAFS studies of the coordination shells around the central U atom.[16,17] Since the Ca-U distance is a key piece of information available from fitting the EXAFS spectra, we examined in detail the Ca-U distances for the $Ca_2UO_2(CO_3)_3$ complex in water.Figure 2-9 shows the RDF of Ca ions around the U atom at three different concentrations. One can see that the asymmetry between the two Ca ions is also reflected in the Ca-U distances: the stronger-binding Ca2 is about 4.05 Å away from U and has a narrower distribution of the Ca2-U distance (standard deviation: 0.10 Å), while the weaker-binding Ca1 is about 4.15 Å away from U (standard deviation: 0.12 Å) and has a broader distribution of the Ca1-U distance. In addition, the three concentrations show very consistent distributions of Ca-U distances.

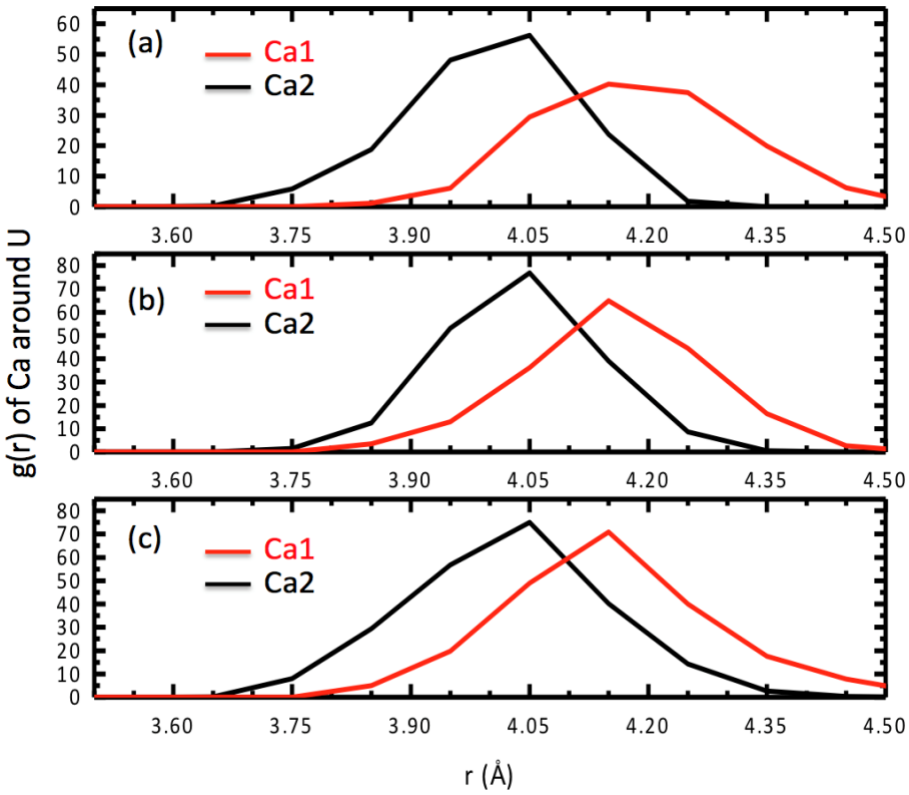

Figure 2-9 Radial distribution functions of Ca ions around the U atom for three different concentrations of $Ca_2UO_2(CO_3)_3$ in water: (a) 0.53; (b) 0.43; (c) 0.36 M.

Table 2-2 Comparison of key distances (in Å) for the $Ca_2UO_2(CO_3)_3$ complex in water among the present DFT-MD simulation, previous EXAFS data, and previous molecular-mechanical MD (MM-MD) simulations

Method	U-O_{eq}	U-O_{ax}	U-O_{dis}	U-Ca	U-C	Reference
DFT-MD[a]	2.45 ± 0.12	1.85 ± 0.04	4.15 ± 0.14	4.07 ± 0.15	2.85 ± 0.10	p.w.
EXAFS-1	2.45 ± 0.01	1.78 ± 0.01	4.11 ± 0.07	4.02 ± 0.02	2.89 ± 0.01	17
EXAFS-2	2.44 ± 0.07	1.81 ± 0.03	4.22 ± 0.04	3.94 ± 0.09	2.90 ± 0.02	16
MM-MD-1	2.43	1.83	3.97	4.00	2.88	24
MM-MD-2i[b]	2.41	n/a	n/a	4.12	n/a	37
MM-MD-2ii[c]	2.41	n/a	n/a	4.18-4.84	n/a	37

[a]Present work (p.w.) for the concentration of 0.36 M: the distances are the peak positions in the radial distribution functions; the error bars are the standard deviations of the distances averaged over 15ps trajectories. [b]A modified force field for calcite was used for the carbonate ion (ref. 37). [c]The AMBER GAFF force field was used for the carbonate ion (ref. 37). n/a: not provided in the reference.

2.3.6 Comparison with the literature

To our knowledge, the present study is the first DFT-MD simulation of the $Ca_2UO_2(CO_3)_3$ complex in water. It would be very informative to compare the present DFT-MD results with previous experiments and molecular-mechanical MD simulations (MM-MD) based on empirical force fields. For comparison with the experiment, we focus mainly on the liquid-phase EXAFS analysis on the structure of the $Ca_2UO_2(CO_3)_3$ complex from Kelley et al.[17] and Bernhard et al.[16] In the model fitting of the EXAFS spectra, they assumed that the two U-Ca distances are the same. To directly compare with their data, we therefore computed the total RDF of Ca ions around U and obtained an average Ca-U distance of about 4.07 Å at the peak of the RDF. Table 2-2 compares our DFT-MD simulation with the EXAFS data (EXAFS-1 from Kelley et al.[17] and EXAFS-2 from Bernhard et al.[16]) and the MM-MD simulations[24,36] for the key distances, including the U-Ca distance. One can see that the DFT-MD results are in good agreement with experiment. Our U-Ca distance is closer to the value from Kelley et al. (4.02 Å) than the one from Bernhard et al. (3.94 Å). Compared with the MM-MD simulation from Kerisit and Liu (MM-MD-1),[24] our DFT-MD simulation gives a U-O_{dis} distance much closer to the experiment. Compared with the MM-MD simulation from Doudou et al. (MM-MD-2),[36] our DFT-MD simulation yields a U-Ca distance in better agreement with the experiment.

2.3.7 Implications of the present findings

As we discussed above, a key finding from the present DFT-MD simulation is the asymmetry between the two Ca ions in the $Ca_2UO_2(CO_3)_3$ complex. A key issue here is whether and how often the two Ca ions can switch their bonding environments, namely, from Ca1-weak binding/Ca2-strong binding to Ca1-strong binding/Ca2-weak binding. Such switching will be closely related to water exchange in the first solvation shell of the Ca ions. In our limited simulation timeframe (~50 ps), we did not observe such switching. This implies that our brute-force DFT-MD is unlike to address this issue due to its limited accessible timescale that is too short in comparison with the timescale of such switching. We are currently pursuing two lines of research to address this issue that will be published in the near future: (a) DFT-MD coupled with metadynamics to estimate the free-energy profile of such switching; (b) classical MD based on force fields to increase the timescale to about ~100 ns.

Despite the limited timescale of the present DFT-MD simulation, our finding of the asymmetry between the two Ca ions in the aqueous $Ca_2UO_2(CO_3)_3$ complex in the timescale of 10 to 100ps may be confirmed by time-resolved EXAFS that can measure the variation in bond length in ps timescale.[37] Here we suggest an experiment to use time-resolved EXAFS to measure the Ca-U distances of the aqueous $Ca_2UO_2(CO_3)_3$ complex at ps snapshots. Another implication from our finding concerns dissociation of $Ca_2UO_2(CO_3)_3$ to $CaUO_2(CO_3)_3^{2-}$. Rao et al. found that in seawater conditions, $Ca_2UO_2(CO_3)_3$ and $CaUO_2(CO_3)_3^{2-}$ account for 58% and 18% of total U(VI), respectively.[9] In other words, $Ca_2UO_2(CO_3)_3$ is in equilibrium with $CaUO_2(CO_3)_3^{2-}$ and free Ca^{2+} in seawater. Our finding suggests that Ca1 is much more likely to break away from $Ca_2UO_2(CO_3)_3$ than Ca2, to form $CaUO_2(CO_3)_3^{2-}$. This information will be useful for studies of the mechanism of $Ca_2UO_2(CO_3)_3$ dissociation with or without an attacking ligand. We plan to also use DFT-MD coupled with metadynamics to examine the free-energy profile of the dissociation mechanism. We suspect that there may exist some intermediate states of the $Ca_2UO_2(CO_3)_3$ complex before it becomes $[CaUO_2(CO_3)_3]^{2-}$ and free Ca^{2+}. For example, one likely configuration can have one Ca ion coordinating to one equatorial and one distal oxygen from the same carbonate group, while the other Ca ion coordinating "normally" to two equatorial oxygens of two different carbonate groups.

2.4 Conclusion

We have simulated the neutral $Ca_2UO_2(CO_3)_3$ complex in water using first principles molecular dynamics based on density functional theory (DFT-MD). Three concentrations (0.53, 0.43, and 0.36 M) feasible to DFT-MD simulations were examined. In the accessible timescale (~ 30 ps), we found that the structure of the $Ca_2UO_2(CO_3)_3$ complex is very stable where the two Ca ions bind to the carbonate groups on the same equatorial plane. We found that one Ca ion binds to the center $UO_2(CO_3)_3^{4-}$ anion stronger than the other Ca ion. This asymmetry of binding between the two Ca ions is reflected in several aspects: the stronger binding Ca has shorter $Ca\text{-}O_{carbonate}$ bonds, shorter Ca-U distance, and four coordinating water molecules, while the weaker binding Ca has longer $Ca\text{-}O_{carbonate}$ bonds, longer Ca-U distance, and five coordinating water molecules. This finding suggests that using time-resolved EXAFS spectra may confirm the asymmetry in binding of the two Ca ions in the aqueous $Ca_2UO_2(CO_3)_3$ complex, since our DFT-MD simulation shows in general good agreement in terms of key distances with the EXAFS experiments.

3 Solvation of the $Ca_2UO_2(CO_3)_3$ Complex in Seawater from Classical Molecular Dynamics Simulations

3.1 Introduction

Previous discussion offered us insights into the structure of the uranyl carbonate species in pure water. However, in seawater, there are large concentrations of salt ions such as Na^+ and Cl^- whose impact on the solvation of $Ca_2UO_2(CO_3)_3$ has not been addressed before in simulation. This knowledge would be useful in designing polymer sorbents to be deployed in seawater. In fact, a recent marine testing of a polymer fiber sorbent after 56 day seawater exposure showed that a significant amount of Na^+ ions was retained in the sorbent.[38] So it is of great importance to illuminate the impact of salt on the solvation of $Ca_2UO_2(CO_3)_3$ in seawater.

The present work seeks to simulate $Ca_2UO_2(CO_3)_3$ in seawater via classical MD simulation, by including Na^+ and Cl^- ions explicitly in our model. In Sec. 3.2, we explain the interaction potential parameters to describe the whole system and the simulation details. In Sec. 3.3, we show our simulation results and focus discussion on the interaction and distribution of Na^+ and Cl^- ions around the $Ca_2UO_2(CO_3)_3$ complex. We conclude in Sec. 3.4 that the Na^+ and Cl^- ions interact very differently with the uranyl complex.

3.2 Computational methods

3.2.1 Force field parameters

Our simulation used parameters from Guilbaud and Wipff who developed force field parameters for the UO_2^{2+} cation and fitted it to the hydration energies of uranyl in aqueous solution[39,40] with the water model TIP3P, a rigid three-site model similar to SPC/E.[41] Kerisit et al. chose the SPC/E model for water in their simulation of the uranyl complex in water.[24] Here we selected the SPC/E model for consistency with the previous work from Kerisit et al. Several different potential models for the carbonate ion exist, either as ions in solution or in the vicinity of carbonate mineral surfaces.[42,43] In addition, the force constant for the carbonate (O-C-O) angles was adjusted so that the overall structure of the tricarbonate complex was reproduced well in the uranyl equatorial plane.[36] The ion parameters based on the SPC/E water model were used for Ca^{2+},[44] Na^+,[45] and Cl^-.[45] The potential parameters for modeling the interactions between Ca^{2+} and water as well as between Ca^{2+} and carbonate were of the Buckingham potential form from de Leeuw and Park.[44] For all other types of atom-atom van der Waals interactions, the Lorentz-Berthelot combination rules [$\varepsilon_{ij} = (\varepsilon_{ii}\varepsilon_{jj})^{1/2}$ and $\sigma_{ij} = (\sigma_{ii}+\sigma_{jj})/2$] were used for the Lennard-Jones parameters between different types of atoms.

3.2.2 Molecular dynamics simulation

Two systems were considered in our MD simulations: (1) $Ca_2UO_2(CO_3)_3$ in pure water and (2) $Ca_2UO_2(CO_3)_3$ in seawater. The simulation cells contained 1000 water molecules at zero applied pressure in the NPT ensemble (constant number of particles, constant pressure, and constant temperature) using the LAMMPS package.[46] For the initial configuration of the first system, we placed an initial structure of the uranium complex as shown in Fig. 1 into a periodic water box. For the initial configuration of the second system, 10 Na^+ and 10 Cl^- ions were randomly placed in the first system to create the simulated seawater with a concentration of Na^+ 10.7 g/kg.[47] The volume of the box was ~31×31×31 $Å^3$ with 3D periodic boundary conditions and the cutoff was set as 12 Å for all non-bonded interactions. The long-range electrostatic interaction was calculated by means of Ewald summation with a 12-Å cutoff for the real space forces.[48] The Ewald sum parameters were chosen to achieve a relative error smaller than 10^{-6} for the electrostatic energy.

The initial structure of each system was first minimized with 1000 steps of the steepest descent method and then the system was heated up from 100K to 300K for 100 ps with a time step of 1 fs. Then the system was equilibrated for 50 ns at 300 K, followed by a 50 ns production run from which the trajectory was sampled every 10 ps for analysis; the temperature was kept constant via the use of the Nosé -Hoover thermostat[49] and the geometry of the water molecules was held fixed using the SHAKE algorithm.[50]

To evaluate the long-timescale dynamics of the system, we ran a 600 ns simulation via GPU-accelerated AMBER 14.0 package,[51] using the same parameters and setup as in the CPU-based LAMMPS MD simulation described in the preceding paragraph.

3.2.3 Quantum chemistry calculation

To validate the force field, quantum chemistry calculations were performed via the Gaussian 09 suite of programs.[52] The geometry of the complex was fully optimized with the B3LYP functional.[53,54] The LANL2DZ basis set, which uses effective-core potentials to describe the inner core orbitals, was employed for uranium,[55] while for the remaining atoms 6-31G(d) was applied.[56] During geometry optimizations, no symmetry or geometry constraint was imposed. Frequency calculations performed at the same theoretical level indicated that the structure obtained corresponds to energetic minima without imaginary frequency.

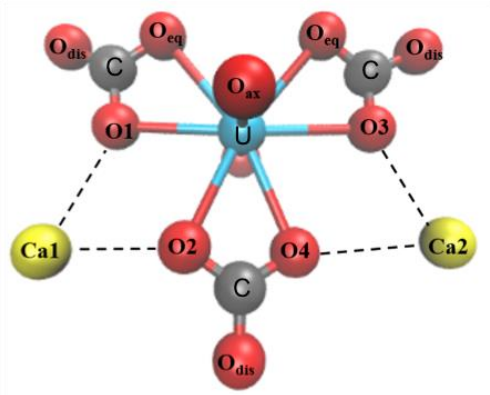

Figure 3-1 The structure of the $Ca_2UO_2(CO_3)_3$ complex in water.

3.3 Results and discussion

The most important structural feature of the $Ca_2UO_2(CO_3)_3$ species is the binding between the two Ca^{2+} ions and the $[UO_2(CO_3)_3]^{4-}$ ion (Figure 1). The three carbonate groups bind to the uranyl group on the equatorial plane in a bidentate mode and the two calcium ions are in the plane of the carbonate ions and bound to two oxygen atoms from two neighboring carbonate groups, consistent with the crystal structure of the naturally occurring mineral Liebigite $[Ca_2(UO_2)(CO_3)_3 \cdot 11H_2O]$[34] and fitting of the EXAFS data.[16,17] Before we simulate this complex in seawater (Sec. 3.3.3), we first validate our force field (Sec. 3.3.1) and compare our simulation in pure water with previous simulations and experiments (Sec. 3.3.2).

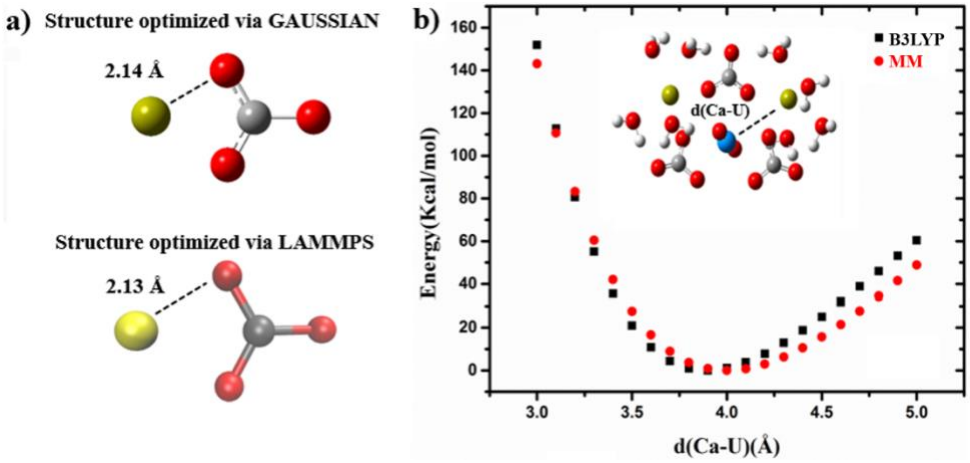

Figure 3-2 Comparison between Gaussian (B3LYP) and LAMMPS (force field, FF): (a) Ca^{2+} and carbonate interaction; (b) the potential energy surface of the $Ca_2UO_2(CO_3)_3$ in a water cluster as a function of the U-Ca distance. Color code: U, yellow; C, grey; O, red; H, white.

3.3.1 Validation of the force field

To validate our force field, we compared our force field parameters (MM) and the quantum mechanical (QM) calculations for Ca^{2+} and carbonate interaction: the Ca-O distance (2.14 Å) from our force field is close to that of QM calculation (2.13 Å) (Figure 3-2a). To further validate our parameters, the potential energy surface of the $Ca_2UO_2(CO_3)_3$ in a water cluster was scanned as a function of the U-Ca distance for both our force-field parameters and the B3LYP method (Figure 3-2b). One can see that the two curves agree quite well, though the difference becomes more apparent at larger U-Ca distances. The discrepancy may be due to the fact that we used the formal charge +2 for the Ca^{2+} ion and ignored charge transfer and polarization between Ca^{2+} and $[CaUO_2(CO_3)_3]^{2-}$ in the force-field curve, while they are included in the B3LYP curve. This deficiency of the force field approach is expected to be less an issue for the Na^+ ion due to its smaller formal charge.

3.3.2 The structure of the $Ca_2UO_2(CO_3)_3$ complex in pure water

To further test our force-field parameters, we investigated the $Ca_2UO_2(CO_3)_3$ complex in pure water since there are quite a few previous experimental and computational studies that we can compare our work with. Table 3-1 compares the key distances in the $Ca_2UO_2(CO_3)_3$ complex among the present classical MD work (MM-MD-1), classical MD from Kerisit et al. (MM-MD-2),[24] DFT-MD from Priest et al.,[57] quantum mechanical charge field MD (QMCF-MD) from Tirlor and Hofer,[27] and two EXAFS studies from Kelley et al.[58] (EXAFS-1) and Bernhard et al.[16] (EXAFS-2). One can see that the general agreement among the different MD simulations is quite good for U-O_{eq}, U-Ca, and U-C distances. Although both MM-MD simulations underestimate the U-O_{dis} distance in comparison with DFT-MD and the experiments, our U-O_{dis} distance (3.95 Å) is consistent with that from Kerisit et al. (3.97 Å). So this could be a deficiency of the force-field parameters that need to be improved further. Since this distance is not essential in comparison with the other distances, we consider our current force field parameters good enough for our purpose of exploring the solvation of the $Ca_2UO_2(CO_3)_3$ complex in water.

Table 3-1 Comparison of key distances (in Å) for the $Ca_2UO_2(CO_3)_3$ complex in water among the present molecular-mechanical MD simulation (MM-MD-1) with previous DFT-MD simulation, QMCF-MD, MM-MD simulation (MM-MD-2), and EXAFS data.

Method	U-O_{eq}	U-O_{ax}	U-O_{dis}	U-Ca	U-C	Ref.
MM-MD-1	2.45	1.85	3.95	4.05	2.85	p.w.
MM-MD-2	2.43	1.83	3.97	4.00	2.88	24
DFT-MD	2.45 ± 0.12	1.85 ± 0.04	4.15 ± 0.14	4.07 ± 0.15	2.85 ± 0.10	58
QMCF-MD	2.47	1.73	-	4.04	2.93	23
EXAFS-1	2.45 ± 0.01	1.78 ± 0.01	4.11 ± 0.07	4.02 ± 0.02	2.89 ± 0.01	17
EXAFS-2	2.44 ± 0.07	1.81 ± 0.03	4.22 ± 0.04	3.94 ± 0.09	2.90 ± 0.02	16

Figure 3-3 shows radial distribution functions (RDFs) of oxygen atoms from the water molecules around the two Ca^{2+} ions both separately and together. One can see that the solvation shell around Ca1 has an average Ca-O distance of 2.35 Å and the integrated RDF gives coordination number of five. On the other hand, Ca2 has four water molecules in the solvation shell with an average Ca-O distance of 2.25 Å. So together, the average coordination number of the two Ca^{2+} ions is 4.5 in terms of water molecules. This asymmetry between the two Ca^{2+} ions is consistent with the previous DFT-MD simulation.[57]

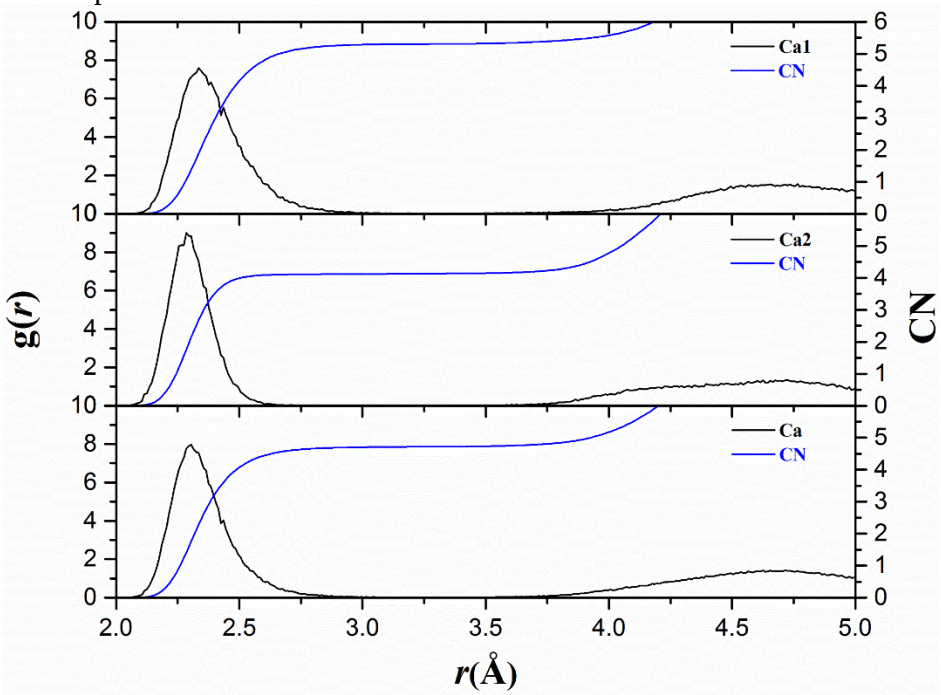

Figure 3-3 Radial distribution function (left axis; black) and its integration (coordination number, CN; right axis; blue) of water oxygen atoms around Ca1 and Ca2 separately (top two panels) and together (bottom panel).

3.3.3 The structure of the $Ca_2UO_2(CO_3)_3$ complex in seawater

The force field validation and the comparison with previous simulations and experiments of the $Ca_2UO_2(CO_3)_3$ complex in pure water discussed above gave us confidence in the force field parameters in our simulation. Now we apply these parameters to simulate the $Ca_2UO_2(CO_3)_3$ complex in seawater which has not been done before. To model the seawater, here we focus on

Na^+ and Cl^- ions which are the most abundant in the seawater. To mimic seawater salinity,[47] we added 10 Na and 10 Cl ions in our 1000-water simulation box that contains one $Ca_2UO_2(CO_3)_3$ complex.

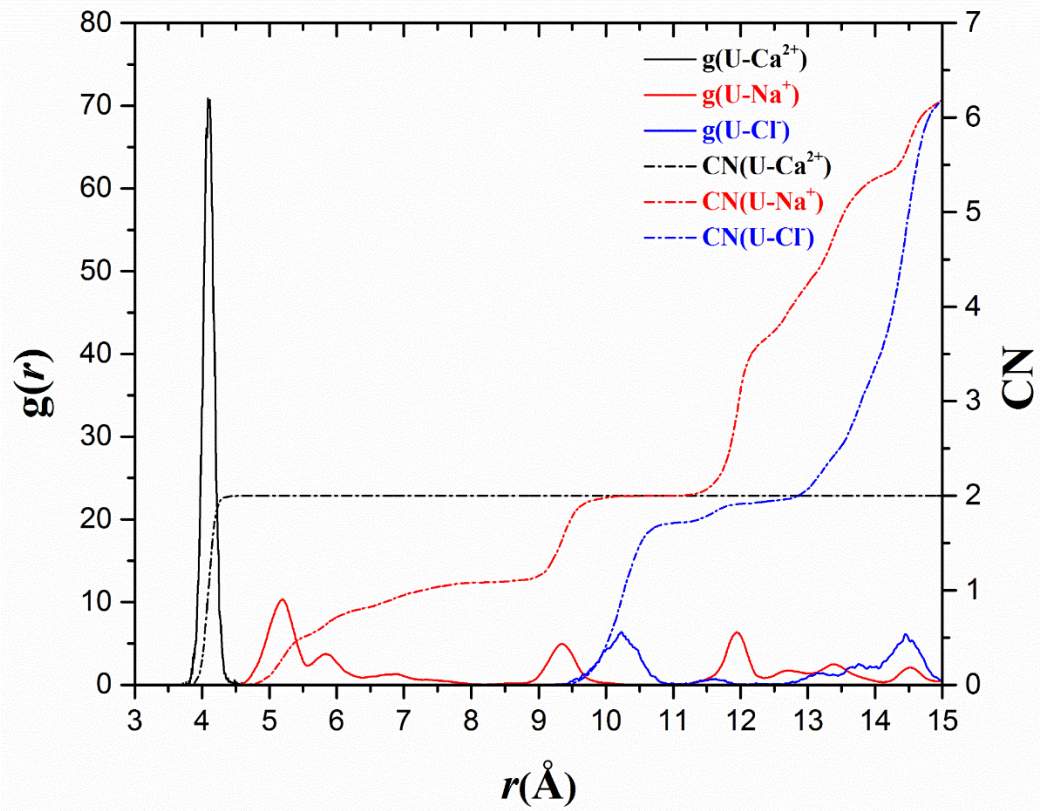

Figure 3-4 Radial distribution functions (left axis) and coordination numbers (CN; right axis) of Ca^{2+} (black), Na^+ (red), and Cl^- (blue) around U.

3.3.3.1 Na^+ and Cl^- ions around the $Ca_2UO_2(CO_3)_3$ complex

We first examine the stability of the complex in seawater. We found that in our simulation time frame (100 ns) the structure of the $Ca_2UO_2(CO_3)_3$ complex is stable in the saline water, as evidenced by the sharp peak at about 4.05 Å in the RDF of Ca around U (Figure 3-4). So we have further confirmed the stability of the $Ca_2UO_2(CO_3)_3$ complex in seawater. Figure 3-4 also shows the RDFs of Na^+ and Cl^- ions around the $Ca_2UO_2(CO_3)_3$ complex. One can see that the distribution of Na^+ and Cl^- ions are not the same: some Na^+ ion is close to the $Ca_2UO_2(CO_3)_3$ complex with a mean Na-U distance of about 5.25 Å. In contrast, the Cl^- ion is much further away from U and the closest average U-Cl distance is about 11 Å. The coordination number of Na around U suggests that there is one Na^+ ion that is very close to U (within 6.0 Å). To locate the close-by Na^+ ion, we analyzed some snapshots of the trajectory. Figure 3-5 shows such a typical snapshot. One can see that the Na^+ ion interacts with the complex indirectly through a water bridge (top arrow in Figure 3-5) to one of the two axial O atoms of the uranyl group. This interaction is also shown schematically in Figure 3-6a.

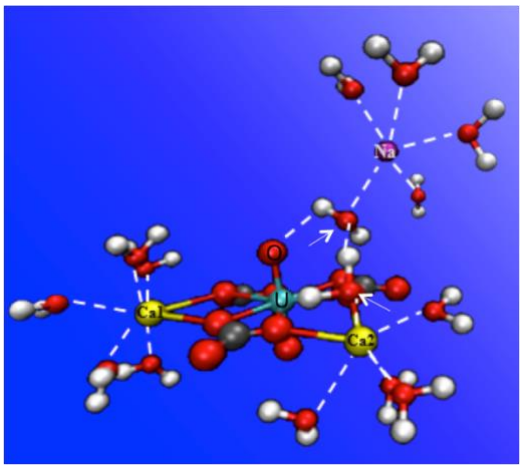

Figure 3-5 A snapshot of the $Ca_2UO_2(CO_3)_3$ complex in seawater, showing only water molecules directly interacting with the two Ca^{2+} ions and the Na^+ ion. Arrows indicate the bridging water molecules.

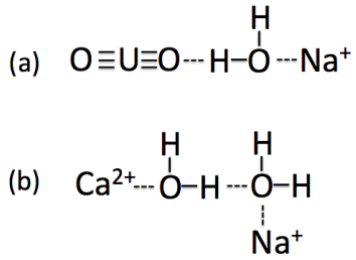

Figure 3-6 Schematics of (a) how the Na^+ ion interacts with the uranyl group; (b) how the Na^+ ion interacts with one Ca^{2+} ion of the $Ca_2UO_2(CO_3)_3$ complex.

3.3.3.2 The interaction of the Na^+ ion with Ca in $Ca_2UO_2(CO_3)_3$

The snapshot in Figure 3-5 also suggests that the close-by Na^+ ion is closer to Ca2 ion than Ca1. This interaction is also mediated via hydrogen bonding through two water molecules (indicated by the two arrows in Figure 3-5) and schematically in Figure 3-6b. In other words, the solvation environments around the two Ca^{2+} ions of the $Ca_2UO_2(CO_3)_3$ complex in seawater are not the same. To further examine this finding, we plot the RDFs of Na^+ ions around the two Ca^{2+} ions separately (Figure 3-7). Indeed, one can see that the mean distance between Ca2 and Na is much shorter than that between Ca1 and Na. The coordination number of Na around Ca2 is two within a sphere of 7.5 Å.

To analyze the impact of the Na^+ ions on the solvation of the $Ca_2UO_2(CO_3)_3$ complex, we show the RDFs of Ca around U in both pure water (Figure 3-8a) and seawater (Figure 3-8b). One can see that the distribution of Ca1 around U is similar to that of Ca2 in pure water, with an average U-Ca distance of 4.05 Å. However, the distribution of Ca1 around U is narrower and higher than that of Ca2 in seawater; the distance between U and Ca1 at 4.05 Å is shorter than that between U and Ca2 at 4.25 Å. In other words, the closer interaction between Ca2 and Na (Figure 3-5 and Figure 3-7) in seawater makes the interaction between Ca2 and U weaker. Hence, the presence of Na^+ ions makes the asymmetry in binding of the two Ca^{2+} ions in the complex even greater.

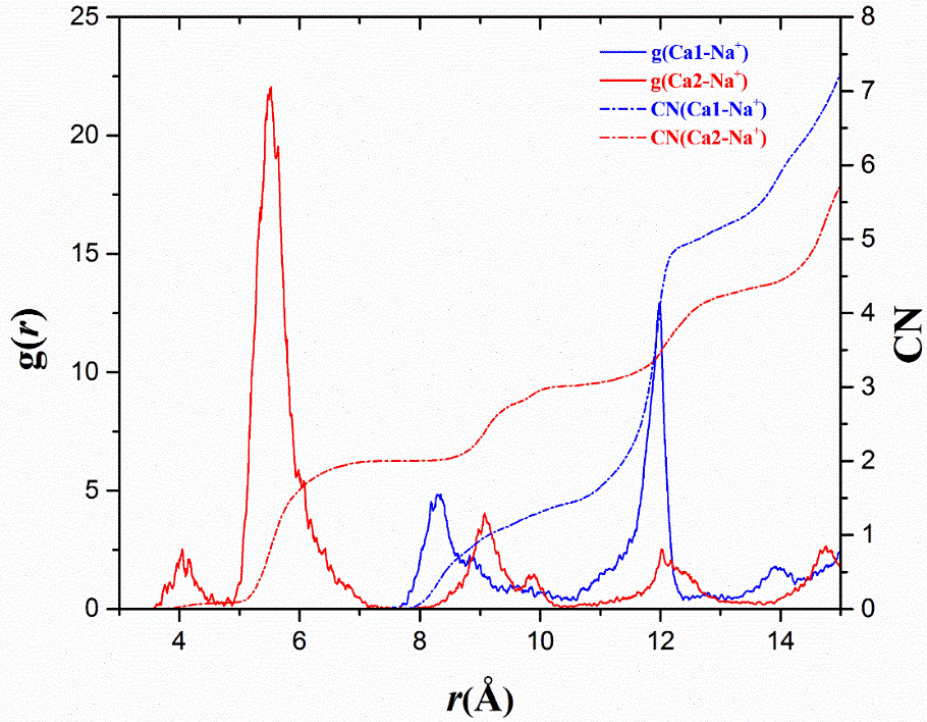

Figure 3-7 Radial distribution functions (left axis; solid lines) and the coordination numbers (CN; right axis; dotted line) of Na around Ca1 (blue) and Ca2 (red).

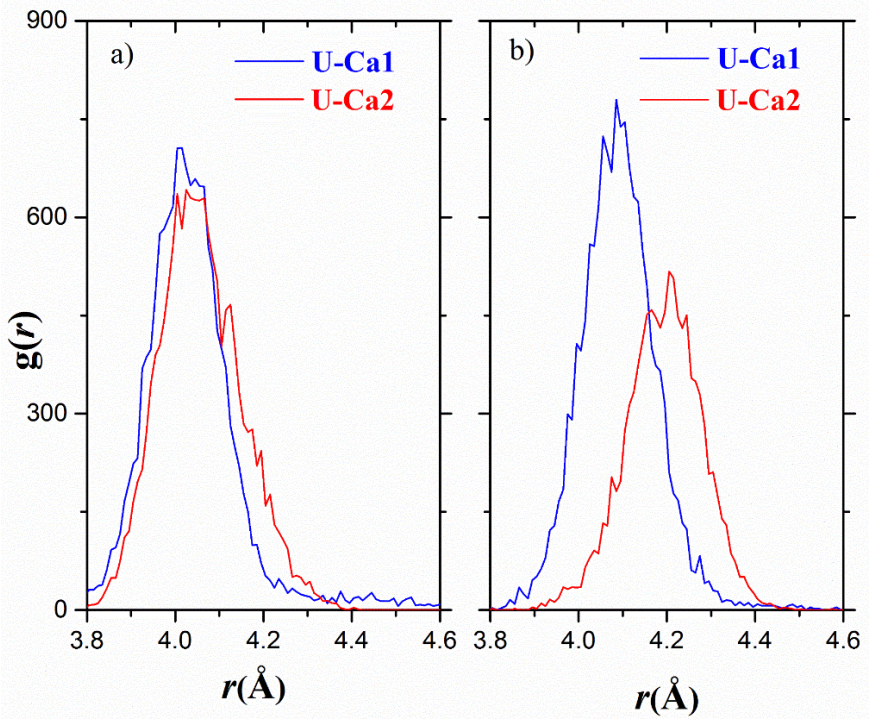

Figure 3-8 Radial distribution function of Ca1 (blue) and Ca2 (red) around U: (a) in pure water; (b) in seawater.

3.3.3.3 Switching of the Na^+ ion between the Ca^{2+} ions in $Ca_2UO_2(CO_3)_3$.

To find out the residence time of the Na^+ ion around one Ca^{2+} ion, we ran a 600ns GPU-accelerated MD simulation (Figure 3-9). We found that the Na^+ ion can switch between Ca1 and Ca2 with a lifetime of about 300 ns. So over a long time (microseconds or longer), the two Ca^{2+} ions would look the same to the close-by Na^+ ion. But with time-resolved experimental techniques such as time-resolved EXAFS that can observe bond length changes on the ps timescale,[37] one would be able to see the difference between the Ca^{2+} ions.

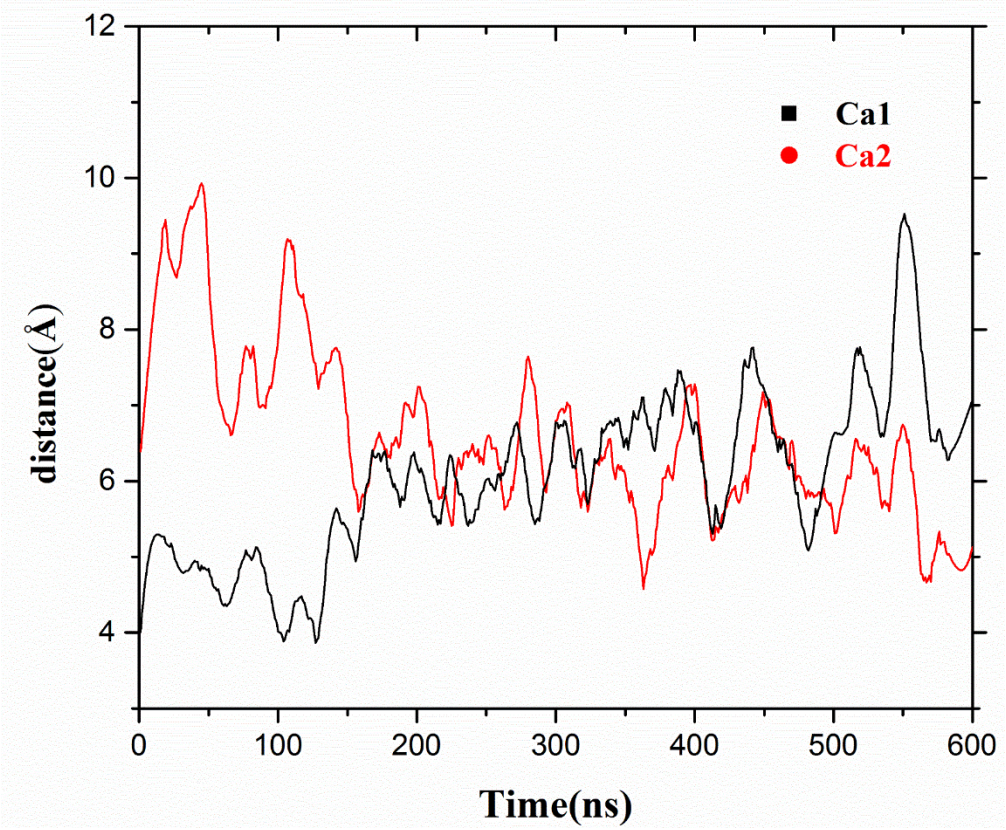

Figure 3-9 Change of the Ca1-Na (black) and Ca2-Na (red) distances with time during the 600-ns dynamics of the $Ca_2UO_2(CO_3)_3$ complex in seawater; the Na^+ ion here refers to the close-by Na^+ ion as shown in Figure **3-5**.

3.3.4 Implications of our simulation results.

The present simulations of the $Ca_2UO_2(CO_3)_3$ complex in seawater have several interesting implications. First, our work shows that there is one Na^+ ion close-by to the complex, so the whole complex can be viewed as a $Na[Ca_2UO_2(CO_3)_3]$ cation of +1 charge. This indicates that a negatively charged sorbent could more effectively attract the complex for binding. Indeed, the amidoxime-grafted polymer sorbent is usually preconditioned with a strong base such as KOH before deployment, which deprotonates the functional groups and renders them anionic.[59] Second, the close-by Na^+ ion also makes the two Ca^{2+} ions very different in binding inside the complex. Especially, the Ca^{2+} ion closely interacting with the Na^+ ion will become easier to break away from the whole complex. We are currently simulating this process for a future publication.

3.4 Summary and conclusions

We have simulated the $Ca_2UO_2(CO_3)_3$ complex in seawater by classical molecular dynamics simulation. We found that the structure of the $Ca_2UO_2(CO_3)_3$ complex is very stable in the model seawater. A Na^+ ion was found to be closely associated with the $Ca_2UO_2(CO_3)_3$ complex at a U-Na distance of 5.25 Å, while the Cl ion is at least 11 Å away from U. The Na^+ ion interacts indirectly with one axial oxygen atom of the UO_2 group bridged by a water molecule. In addition, the Na^+ ion interacts closely with one Ca^{2+} ion than the other. The present simulations revealed the key role of common ions such as Na^+ in impacting the solvation, structure, and apparent charge of the $Ca_2UO_2(CO_3)_3$ complex in seawater. This knowledge will be useful in understanding the chemistry of uranium recovery from the sea by sorbents.

4 Effect of Salt on the Uranyl Binding with Carbonate and Calcium Ions in Aqueous Solutions

4.1 Introduction

Known the structural properties of uranium complex in pure water and seawater, in this chapter we start to study the formation of $Ca_2(UO_2)(CO_3)_3$ complex from UO_2^{2+}, CO_3^{2-}, and Ca^{2+} in seawater condition. Although the free energies of binding between CO_3^{2-} and UO_2^{2+} have been obtained previously from classical MD,[60] the role of NaCl and the free energies of further binding with Ca^{2+} have not been simulated before. Hence our main goal is to reveal and understand the influence of NaCl on the binding process and free energies. We hypothesize that the presence of Na^+ ions can greatly impact the binding of UO_2^{2+}, CO_3^{2-}, and Ca^{2+} ions as well as the solvation, structure, and relative stability of $UO_2(CO_3)_3^{4-}$, $CaUO_2(CO_3)_3^{2-}$ and $Ca_2UO_2(CO_3)_3$ species in water. Endrizzi and Rao[9] have shown from their experiments that the binding free energies of UO_2^{2+} with CO_3^{2-} and Ca^{2+} ions change from pure water to 0.1 M NaCl solution, but there is a lack of understanding at the molecular level how the Na^+ ions impact the binding process in terms of the solvent-shared ion pair (SSHIP), solvent-separated ion pair (SSIP), and contact-ion pair (CIP).

To test our hypothesis, we employ molecular dynamics (MD) simulations combined with umbrella sampling to obtain free energy of binding and to reveal the atomistic mechanism of the complete binding processes of CO_3^{2-} and Ca^{2+} with UO_2^{2+} to form the $Ca_2(UO_2)(CO_3)_3$ complex in 0.1 M NaCl, in comparison with in pure water.

4.2 Computational methods

4.2.1 Simulation systems and force field parameters

One UO_2^{2+}, three CO_3^{2-}, and two Ca^{2+} ions, which were apart from each other, were added into a periodic water box of 2,000 water molecules. To simulate the effect of ionic strength, we also considered a different water box where at least four Na^+ and Cl^- ions with additional ones to neutralize the system were added to reach a concentration of 0.1 M, very similar to the experimental condition of ionic strength.[9] The original TIP3P model[41] was employed for the water molecules. The force field parameters of the solute molecules (UO_2^{2+} and CO_3^{2-}) were chosen from the recent study of Kerisit and Liu,[60] in which the calculated association constants of uranyl with carbonates excellent agree with experimental measurements.[61] Since Kerisit and Liu's parameters were paired the SPC/E water model, we compared the compatibility of their parameters with the original TIP3P water model and found that the two water models yield very similar structure of uranyl in water and bind free energy of UO_2^{2+} and CO_3^{2-} (see the Supporting Information). The Na^+ and Cl^- ions were modeled with the parameterization of Joung and Cheatham.[45] We chose the parameters for Ca^{2+} from the work of Rahaman et al.[62-36]

4.2.2 Classical molecular dynamics simulations

Classical molecular dynamics (CMD) simulations were carried out for each prepared system by employing the Amber14 molecular simulation package.[51] First, 4,000 cycles of minimization (2,000 cycles of steepest descent and 2,000 cycles of conjugate gradient) were carried out to relax the solvent, while all the solute atoms were constrained by a potential of 3,000 kcal/(mol/Å). Second, another minimization stage was conducted with the solute atoms constrained by 500 kcal/(mol/Å). Third, 4000 cycles of energy minimization (2,000 cycles of steepest descent and 2,000 cycles of conjugate gradient) were carried out without any constraint. Next, the system was gradually heated from 0 to 300 K over a period of 50 ps, followed by another

100 ps of *NPT* MD simulations to relax the system to its equilibrium density, which is close to 1.0 g/cm^3, with the target temperature of 300 K and the target pressure of 1.0 atm. Afterward, at least 5 ns of *NPT* MD simulation with a target temperature of 300 K was performed for production run. All the simulations were accomplished by applying the GPU-accelerated *pmemd* program[51] in Amber14. A time step of 1.0 fs was used for all the simulations. The SHAKE algorithm[50] was applied to constrain all hydrogen-containing bonds with a tolerance of 10^{-5}. The Berendsen thermostat method[63] was used to control the system temperature and a cutoff of 12 Å was set for both van de Waals (vdW) and the real-space part of electrostatic interactions. A continuum model correction implemented in Amber 14 for energy and pressure was used for the long range vdW correction. Long range electrostatics were calculated using Particle mesh Ewald (PME)[64] with the Ewald coefficient of 0.22664 Å^{-1} for the reciprocal part and a cubic spline switch function for the direct sum.

4.2.3 Umbrella sampling

The umbrella sampling technique[65,66] was employed to map out the free energy profiles of the binding of CO_3^{2-} and Ca^{2+} ions with UO_2^{2+}. The U-C distance was chosen as the reaction coordinate (RC) for the binding of CO_3^{2-} ions with UO_2^{2+} to form $UO_2(CO_3)_3^{4-}$, while the U-Ca distance was chosen as the RC for the binding of Ca^{2+} ions with $UO_2(CO_3)_3^{4-}$. For each binding process, CMD simulations were performed with a series of biasing harmonic potential (50 kcal mol^{-1} Å^{-2}) along the RC from 12.7 Å down to 2.2 Å with about 50 ~ 65 simulation windows. 2 ns MD simulation was carried out for each window with the second half being sampled for production. Then the simulation data for all windows of each system were collected to determine the probability distributions along the RC and further pieced together by the weighted histogram analysis method (WHAM)[67,68] to generate the potential of mean force (PMF, i.e., free energy profile). The statistical uncertainties in the PMF and hence in the binding free energies (Table 4-1 and Table 4-2) are evaluated by performing Monte Carlo bootstrapping at each pin. From the PMF, we then obtain the binding free energy using the approach of Chialvo et al.[60,69] In this approach, the PMF obtained from umbrella sampling, denoted as $W_{AC}(r)$, was first converted to the radial distribution function of ions pair in the infinite dilution limit, $g_{AC}^{\infty}(r)$, using the following equation:

$$W_{AC}(r) = -kT \ln g_{AC}^{\infty}(r), \tag{4.1}$$

where k is Boltzmann constant and T is the temperature. The equilibrium constant K_a for association of the anion-cation pair in the infinite-dilution is then computed by integrating $g_{AC}^{\infty}(r)$:

$$K_a = 4\pi \int_{r_{min}}^{r_{max}} g_{AC}^{\infty}(r)\, r^2 dr, \tag{4.2}$$

where r_{min} and r_{max} define the distance range of the association process. We then compute $\Delta G = -RT \ln K_a$. To estimate the error introduced to our calculation of ΔG based on the assumption of infinite dilution or activity coefficients are equal to one, we applied the specific ion interaction theory[61,70] to assess the activity coefficients and the correction to K_a. The activity coefficients in 0.1 M NaCl are estimated to be: $\gamma_{UO_2CO_3} = 1$, $\gamma_{UO_2^{2+}} = 0.86$, and $\gamma_{CO_3^{2-}} = 0.80$. These will lead to a correction factor of 1.45 to K_a and an error of –0.9 kJ/mol to ΔG. Since this error is smaller than the average difference between our simulation and the experiment (~3 kJ/mol), we did not include this correction in our computed ΔG.

4.3 Results and discussion

Our key hypothesis is that the presence of Na^+ ions can greatly impact the binding of UO_2^{2+}, CO_3^{2-}, and Ca^{2+} ions as well as the solvation, structure, and relative stability of $UO_2(CO_3)_3^{4-}$,

$CaUO_2(CO_3)_3^{2-}$ and $Ca_2UO_2(CO_3)_3$ species in water. To reveal the role of Na^+ ions, we will show in detail the comparison of the binding of UO_2^{2+}, CO_3^{2-}, and Ca^{2+} ions between in 0.1 M NaCl and in pure water.

4.3.1 Role of 0.1 M NaCl in CO_3^{2-} binding with UO_2^{2+}

Figure 4-1 compares the spontaneous process of binding between one UO_2^{2+} and three CO_3^{2-} groups in 0.1 M NaCl and in pure water. One can see that in pure water, the first CO_3^{2-} group approaches and binds to the UO_2^{2+} very quickly at about 11 ns, due to the strong electrostatic attraction. Interestingly, the second and third CO_3^{2-} groups bind at about the same time around 15 ns. In contrast, the U-C distances experience large fluctuation in the 0.1 M NaCl solution, before the first CO_3^{2-} binding with the UO_2^{2+} at the time of 22 ns, followed by the very quick second and third CO_3^{2-} binding events. The presence of Na^+ and Cl^- ions seems to slow down the binding process of between CO_3^{2-} and UO_2^{2+}. This slowdown can be understood from the additional electrostatic interactions between Na^+ and CO_3^{2-} as well as between UO_2^{2+} and Cl^-, which have to be overcome when CO_3^{2-} binds to UO_2^{2+}, even though the presence of Na^+ and Cl^- ions reduced the dielectric screening between CO_3^{2-} and UO_2^{2+} leading to a stronger binding. Next we examine the thermodynamics of CO_3^{2-} and UO_2^{2+} binding.

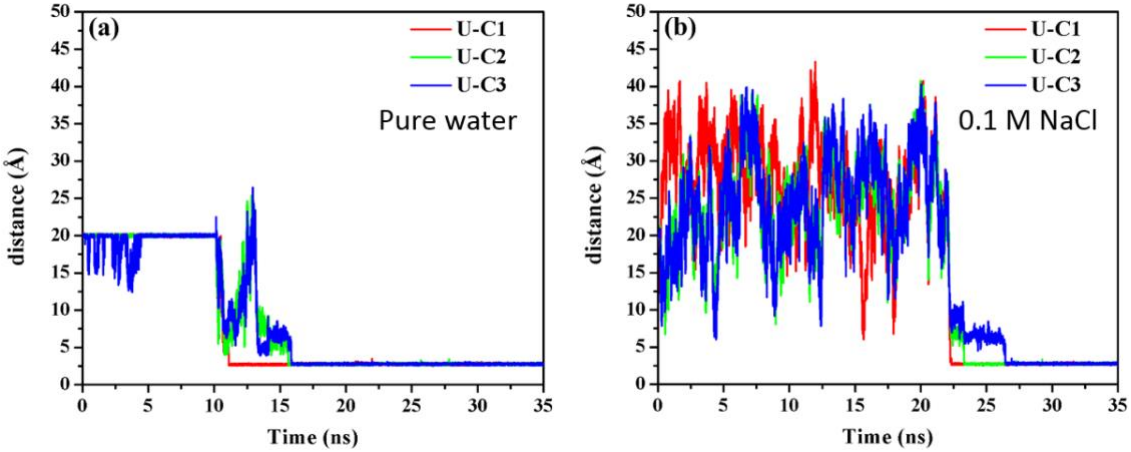

Figure 4-1 Non-restrained molecular dynamics simulations of initially far-apart UO_2^{2+} and three CO_3^{2-} groups as monitored by the three U-C distances: (a) in pure water; (b) in 0.1 M NaCl.

Figure 4-2 compares the complete potential of mean force (PMF) profiles for the sequential binding of the three CO_3^{2-} binding to UO_2^{2+} in 0.1 M NaCl with in pure water. As can be seen, in both pure water and 0.1 M NaCl, the three CO_3^{2-} groups could bind to UO_2^{2+} spontaneously with a large free-energy gain, yet the association process varies with the presence of Na^+ and Cl^- ions and the increasing number of CO_3^{2-} groups. In pure water, the three binding events share the similar mechanism: the shallow minimum between 6 and 8 Å corresponds to the solvent-separated ion pair (SSIP) and the deeper minimum between 4 and 6 Å to the solvent-shared ion pair (SSHIP), while the contact-ion pair (CIP) at 3.4–3.6 Å and 2.9–3.0 Å represents the mono- and bidentate binding states of CO_3^{2-} with UO_2^{2+}, respectively. These results are in agreement with a previous study.[60] Figure 4-3a, Figure 4-3b, and Figure 4-3c show some snapshots of the solvent-separated ion pairs in pure water where the ion interaction is mediated by the hydrogen bonds of water molecule, while in 0.1 M NaCl, the ion pairing is mediated the Na^+ ion interacting with the CO_3^{2-} group and the complex (Figure 4-3d, Figure 4-3e, and Figure 4-3f).

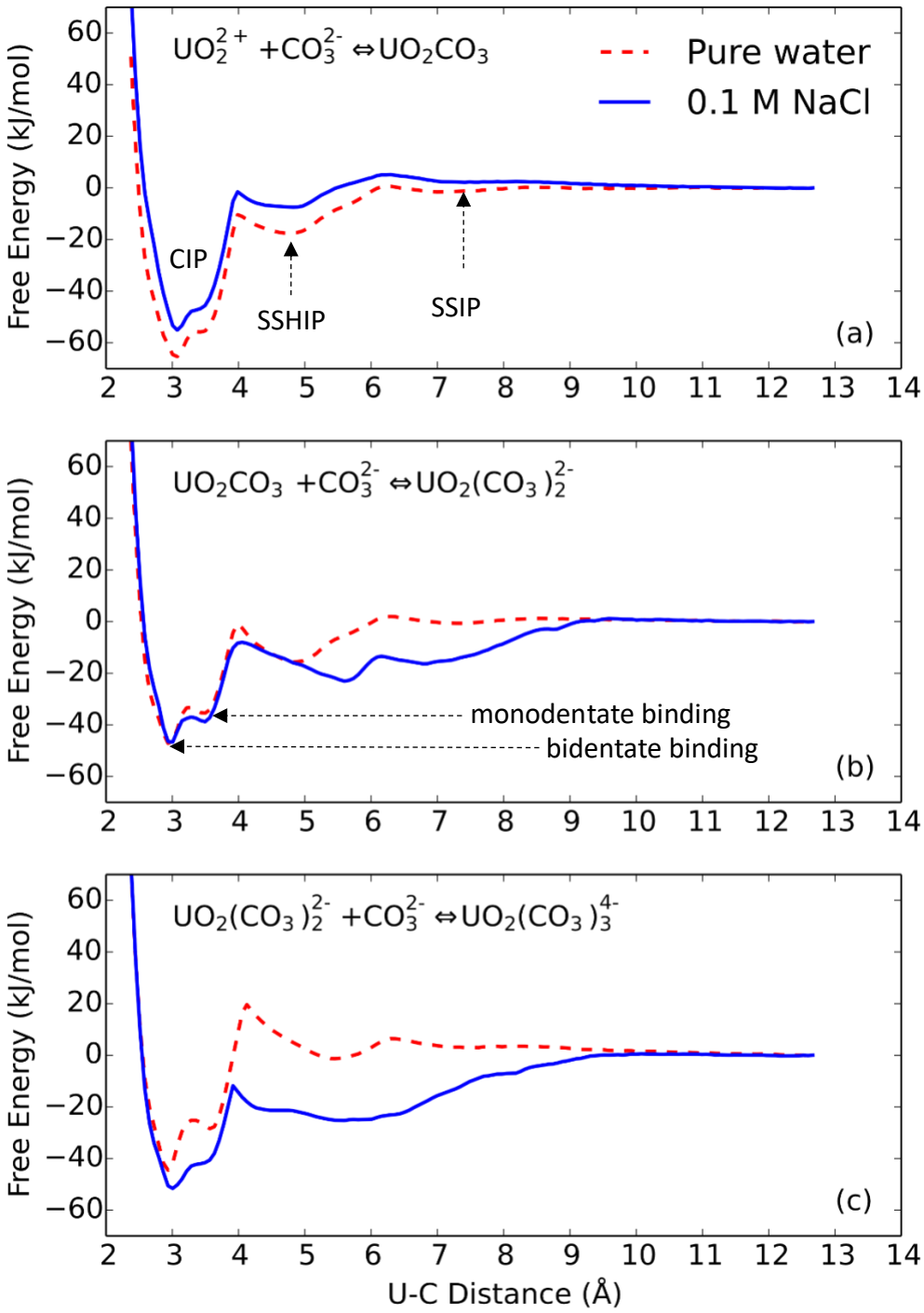

Figure 4-2 The potential of mean force profiles (i.e., free-energy profiles) of the sequential binding of the first (a), second (b) and third (c) CO_3^{2-} group to UO_2^{2+} along the reaction coordinate defined as the distance between the U atom and the C atom of the approaching CO_3^{2-}: red dashed line, in pure water; blue solid line, in 0.1 M NaCl. In (a) for the pure water case, positions of solvent-shared ion pair (SSHIP), solvent-separated ion pair (SSIP), and contact-ion pair (CIP) are indicated.

In binding the first carbonate, the calculated binding free energy decreases from –59.8 kJ/mol in pure water to –49.4 kJ/mol in 0.1 M NaCl (Table 4-1), due to screening of the attraction between UO_2^{2+} and CO_3^{2-} by Na^+ and in good agreement with the experimental data from –56.8 kJ/mol in pure water to –51.8 kJ/mol in 0.1 M NaCl.[9] Na^+ also slightly affected the binding of the second carbonate (Figure 4-3e), but due to the neutral nature of UO_2CO_3, its binding free energy with CO_3^{2-} is not affected by the presence of Na^+ and Cl^- ions, as shown in both our simulation (–35.6 kJ/mol) and experiment (–38.1 kJ/mol) in Table 4-1. Na^+ has a great impact on the binding of the third CO_3^{2-}, as it significantly reduces the repulsion between $UO_2(CO_3)_2^{2-}$ and CO_3^{2-} by being between them (Figure 4-3f); the calculated binding free energy changes from –27.1 kJ/mol in pure water to –35.5 kJ/mol in 0.1 M NaCl (Table 4-1), in good agreement with the experiment from -29.9 kJ/mol to -34.8 kJ/mol and indicating a stronger binding in 0.1 M NaCl than in pure water. In addition, Figure 4-1c shows that the barrier from the SSHIP (at about 5.8 Å) to the CIP (at about 3 Å) decreases from about 20 kJ/mol in pure water to about 10 kJ/mol in 0.1 M NaCl.

Table 4-1 Simulated free energy (ΔG) of CO_3^{2-} and UO_2^{2+} under pure water (I=0) and 0.1 M NaCl (I=0.1) conditions, in comparison with the experimental data.[9]

Reaction	I (mol/L)	Simulation (kJ/mol) ΔG	Experiment (kJ/mol) ΔG ± δ	Error (kJ/mol) Sim - Exp
$UO_2^{2+} + CO_3^{2-} = UO_2(CO_3)$ (aq)	0.1	-49.4	-51.8±0.2	2.4
	0	-59.8	-56.8±0.2	-3.0
$UO_2(CO_3)$ (aq) + $CO_3^{2-} = UO_2(CO_3)_2^{2-}$	0.1	-35.6	-38.1±0.5	2.5
	0	-35.6	-38.1±0.5	2.5
$UO_2(CO_3)_2^{2-} + CO_3^{2-} = UO_2(CO_3)_3^{4-}$	0.1	-35.5	-34.8±0.6	-0.7
	0	-27.1	-29.9±0.6	2.8

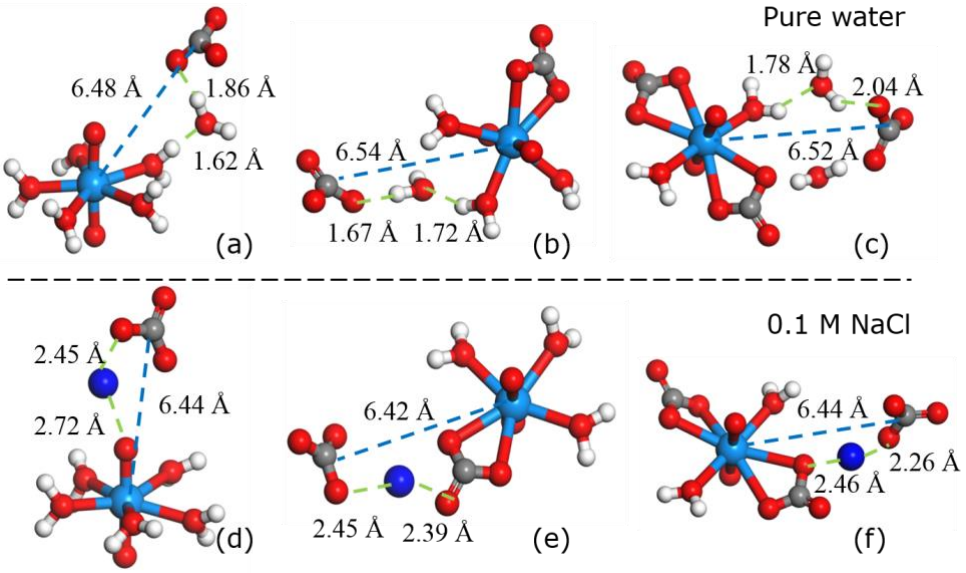

Figure 4-3 Snapshots of ion pairs. In pure water: (a) CO_3^{2-} and UO_2^{2+}; (b) CO_3^{2-} and UO_2CO_3; (c) CO_3^{2-} and $[UO_2(CO_3)_2]^{2-}$. In 0.1 M NaCl: (d) CO_3^{2-} and UO_2^{2+}; (e) CO_3^{2-} and UO_2CO_3; (f) CO_3^{2-} and $[UO_2(CO_3)_2]^{2-}$. Color code: U, light blue; O, red; C, grey; Na, dark blue; H, white.

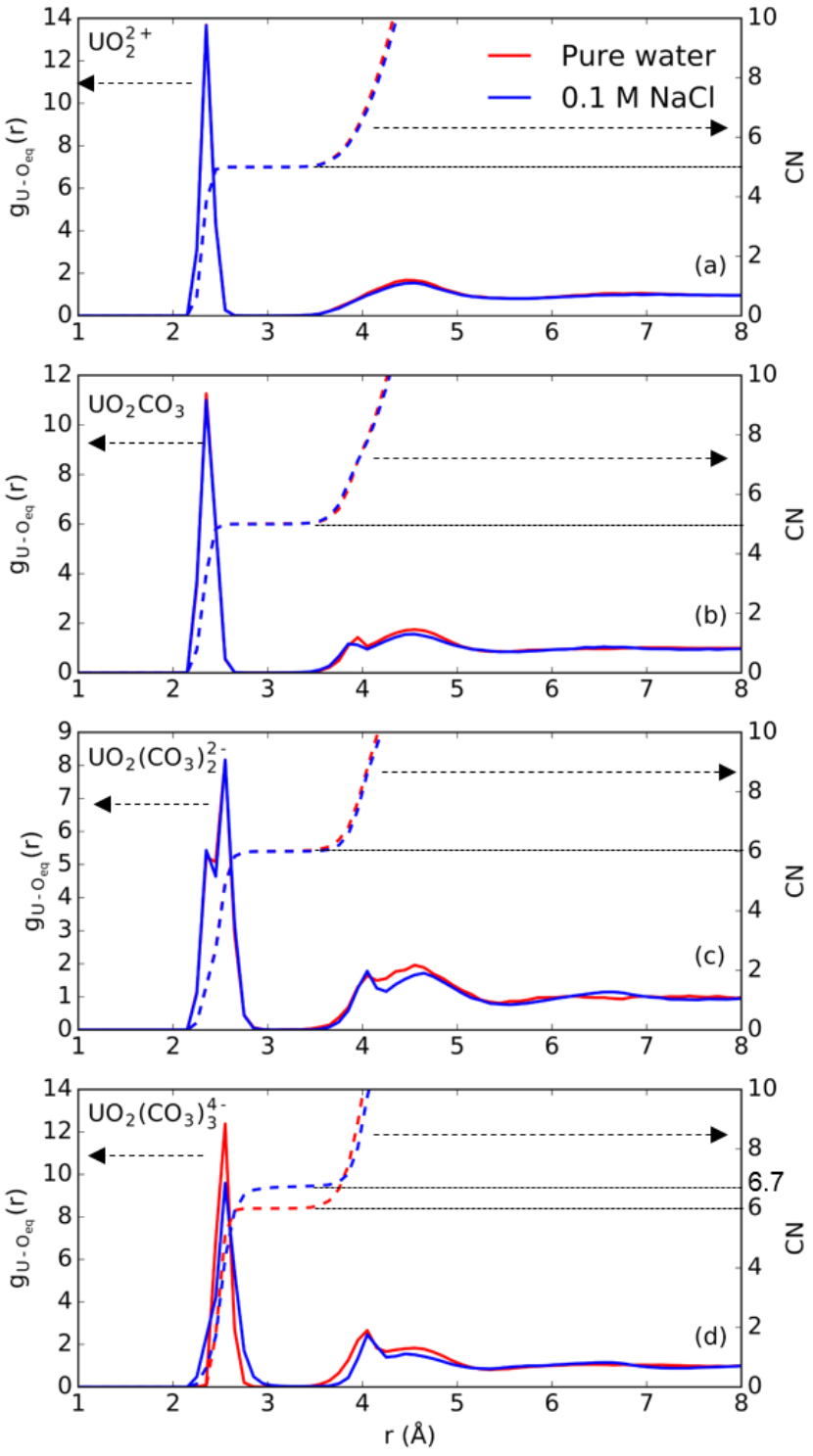

Figure 4-4 The radial distribution function (solid lines) and coordination number (CN; dashed lines) of the oxygen atoms (except the uranyl oxygens) around U in pure water (in red color) and 0.1 M NaCl (in blue color): (a) UO_2^{2+}; (b) $UO_2(CO_3)$; (c) $[UO_2(CO_3)_2]^{2-}$; (d) $[UO_2(CO_3)_3]^{4-}$.

4.3.2 Role of Na^+ ions in Coordination of CO_3^{2-} groups around UO_2^{2+}

We first examine the impact of Na^+ ions in water coordination. From Figure 4-4, one can see that the biggest difference between 0.1 M NaCl and pure water happens to $UO_2(CO_3)_3^{4-}$, while there is little difference for UO_2^{2+}, UO_2CO_3 and $UO_2(CO_3)_2^{2-}$. Figure 4-4a shows that before CO_3^{2-} binding to the UO_2^{2+}, the total coordination number (CN) of O (excluding the two axial O atoms of the uranyl group) around U is five. This corresponds to the five equatorial water molecules, of which the average U-O_{water} distance is 2.34 Å. The CN of O atoms around U remains at five after the first carbonate binding and the averaged U-O_{eq} distance is slightly elongated to 2.35 Å (Figure 4-4b), contributed by the exchange of two water molecules with CO_3^{2-}. The different contribution of water and carbonates to the equatorial O around U is more clearly seen from Figure 4c, in which two CO_3^{2-} groups are bound with UO_2^{2+}. The RDFs have two peaks in the first coordination shell, corresponding to the average U-O_{water} distance of 2.34 Å and U-$O_{carbonate}$ distance of 2.54 Å. Meanwhile the total coordination numbers contributed by water and carbonate groups yield six: $UO_2(H_2O)_2(CO_3)_2^{2-}$, in agreement with the extended X-ray absorption fine-structure (EXAFS).[71]

Figure 4-4d shows that the solvation structure of $UO_2(CO_3)_3^{4-}$ is very different in pure water and in 0.10 M NaCl. In pure water, all the three carbonate groups coordinate with uranium in a bidentate mode (Figure 4-5a), yielding an equatorial coordination number of six. But in 0.1 M NaCl, we found that carbonate groups switch between monodentate and bidentate binding configurations, with an average total coordination number of ~5.7, while an additional water in the first coordination shell, leading to a total coordination number of ~6.7 (Figure 4-4d); a snapshot of the coordination is shown in Figure 4-5b which shows that a Na^+ ion closely interacts with two carbonate groups, causing one of them to have the monodentate binding with U instead of bidentate.

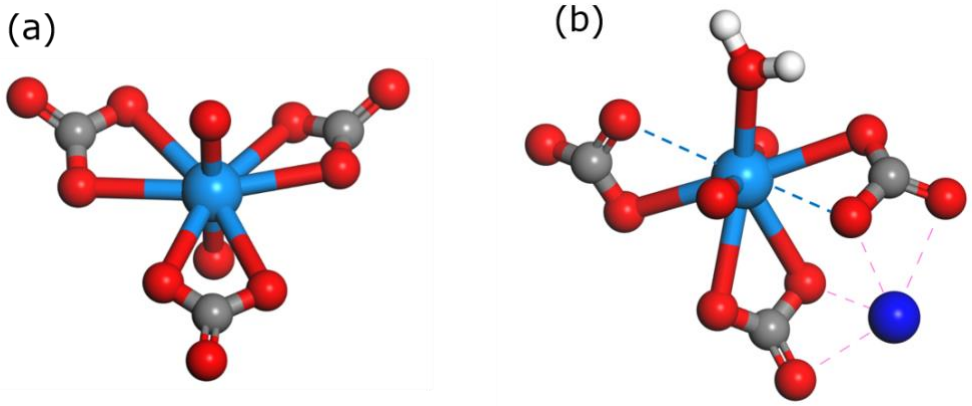

Figure 4-5 Typical configuration of $UO_2(CO_3)_3^{4-}$ in pure water (a) and in 0.1 M NaCl (b). Color code: U, light blue; O, red; C, grey; Na, dark blue; H, white.

4.3.3 Impact of 0.1 M NaCl on $UO_2(CO_3)_3^{4-}$ binding with Ca^{2+}

We first examine the dynamics of $UO_2(CO_3)_3^{4-}$ binding with two Ca^{2+} ions located 20 Å away, using the non-restrained, brute-force molecular dynamics to simulate the impact of 0.1 M NaCl. As shown in Figure 4-6, one can see in pure water that the approaching and binding of the two Ca^{2+} to $UO_2(CO_3)_3^{4-}$ is a very smooth process with small fluctuation in the U-Ca distances and the binding happens sequentially at 7.5 ns and 15 ns. In 0.1 M NaCl, the U-Ca distances show greater fluctuation and the binding happens almost simultaneously at about 40 ns.

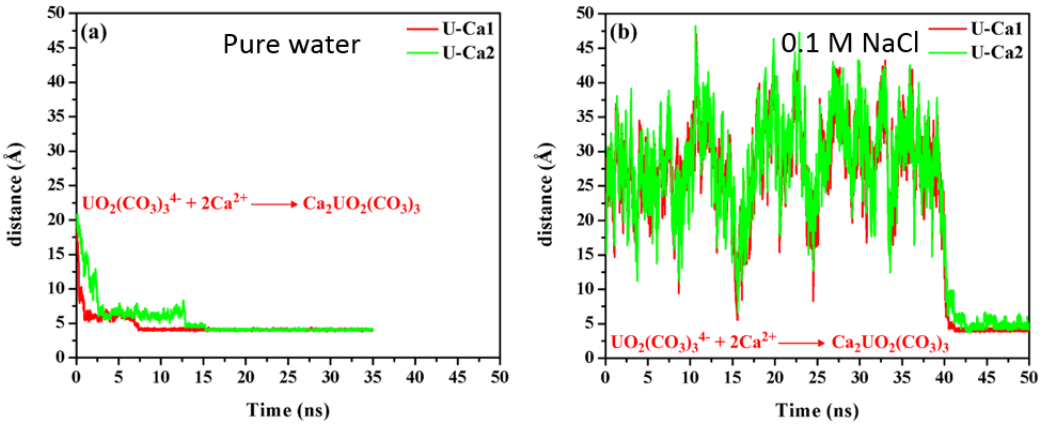

Figure 4-6 Non-restrained, brute-force molecular dynamics simulations of initially far-apart $UO_2(CO_3)_3^{4-}$ and two Ca^{2+} ions as monitored by the two U-Ca distances: (a) in pure water; (b) in 0.1 M NaCl.

We further determined the complete free-energy profiles for the two Ca^{2+} ions binding to $UO_2(CO_3)_3^{4-}$. As shown in Figure 7, no matter in pure water or 0.1 M NaCl, the two Ca^{2+} ions bind with $UO_2(CO_3)_3^{4-}$ favorably with a close-to-zero barrier. All the binding processes are exergonic, while it is less so in 0.1 M NaCl than in pure water. Table 2 shows that the calculated binding free energy changes from -36.9 kJ/mol in pure water to -20.0 kJ/mol in 0.1 M NaCl for the first Ca^{2+} ion binding and from -22.3 kJ/mol in pure water to -14.7 kJ/mol in 0.1 M NaCl for the second Ca^{2+} ion binding, all in good agreement with the experiment. Apparently, the presence of 0.1 M NaCl reduces the electrostatic attraction between of $UO_2(CO_3)_3^{4-}$ and Ca^{2+} ions.

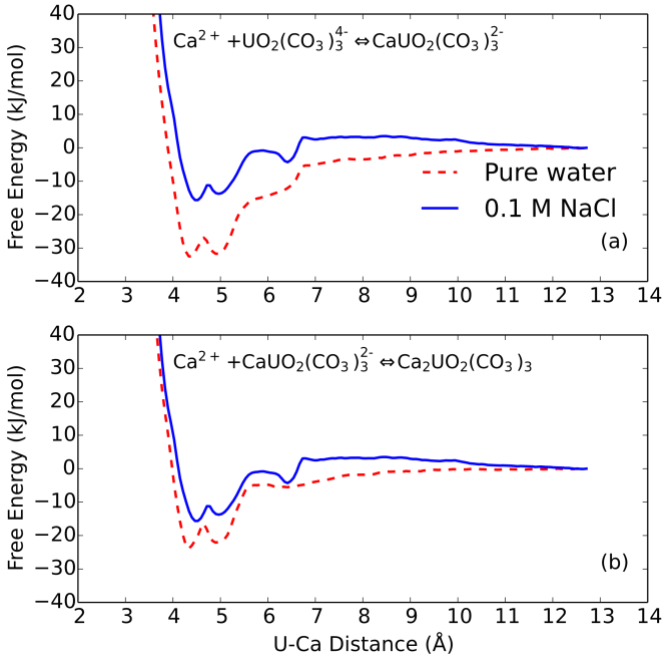

Figure 4-7 The potential of mean force profiles (i.e., free energy profiles) of the sequential binding of the first (a) and the second (b) Ca^{2+} ions to $UO_2(CO_3)_3^{4-}$ along the reaction coordinate defined as the distance between the U atom and the approaching Ca^{2+} ion: red dashed line, in pure water; blue solid line, in 0.1 M NaCl.

Table 4-2 Simulated free energy (ΔG) of $UO_2(CO_3)_3^{4-}$ and Ca^{2+} complexation in pure water (I=0) and 0.1 M NaCl (I=0.1) conditions, in comparison with the experimental data.[9]

Reaction	I (mol/L)	Simulation (kJ/mol) ΔG	Experiment (kJ/mol) ΔG ± δ	Error (kJ/mol) Sim - Exp
$Ca^{2+} + UO_2(CO_3)_3^{4-} = CaUO_2(CO_3)_3^{2-}$	0.1	-20.0	-19.5±0.3	-0.5
	0	-36.9	-29.5±0.3	-7.4
$Ca^{2+} + CaUO_2(CO_3)_3^{2-} = Ca_2UO_2(CO_3)_3$ (aq)	0.1	-14.7	-17.1±0.4	2.4
	0	-22.3	-21.9±0.4	-0.4

Figure 4-7 shows that there are three free-energy minima along the path of Ca^{2+} ions binding to $UO_2(CO_3)_3^{4-}$. The one near 4.3 Å corresponds to the Ca^{2+} ion between two carbonates that bind to U in a bidentate mode (Figure 4-8a and Figure 4-8b), while the one near 4.9 Å corresponds to the Ca^{2+} ion interacting with one carbonate that bind to U in a bidentate mode (Figure 4-8a). The minimum near 6.4 Å corresponds to the Ca^{2+} ion interacting with one carbonate that bind to U in a monodentate mode (Figure 4-8b).

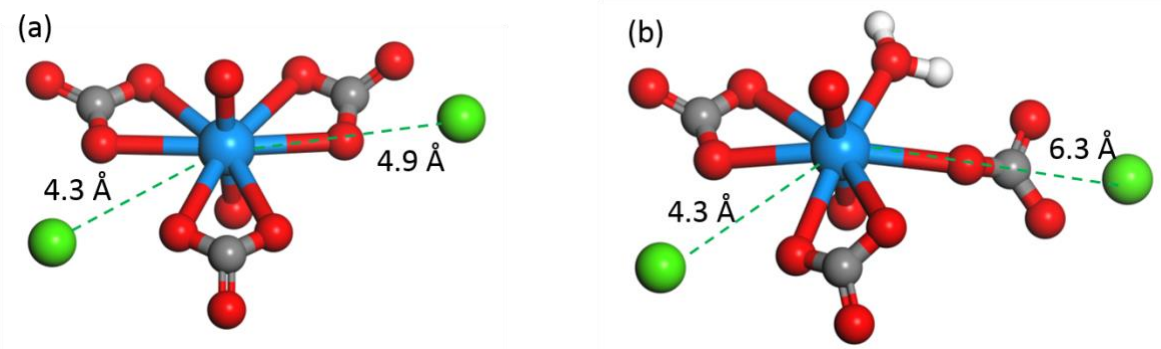

Figure 4-8 Key U-Ca distances with which the Ca-uranyl complex structures locate at the local minimums of free energy profile: (a) 4.3 and 4.9 Å; (b) 4.3 and 6.3 Å. Color code: U, light blue; O, red; C, grey; Na, dark blue; H, white.

4.3.4 Impact of Na^+ ions on Solvation of $Ca(UO_2)(CO_3)_3^{2-}$ and $Ca_2(UO_2)(CO_3)_3$

The impact of Na^+ ions is often reflected in the water coordination, so we first compare the water solvation around $Ca(UO_2)(CO_3)_3^{2-}$ and $Ca_2(UO_2)(CO_3)_3$. The RDF plot (Figure 4-9a) shows that the total CN of O around U in the $Ca(UO_2)(CO_3)_3^{2-}$ complex is 6 in pure water (see Figure 4-10a for the most probably structure) but increases to about 6.5 in 0.1 M NaCl. From the most representative structure of the $Ca(UO_2)(CO_3)_3^{2-}$ complex in 0.1 M NaCl (Figure 4-10b), one can see that one of the two carbonates coordinating with Ca^{2+} is tilted out of the equatorial plane around U and becomes monodentate. This is caused by the presence of a close-by Na^+ ion; as a result, a water molecule is allowed to enter the first coordination shell (Figure 4-10b), leading to a CN greater than 6.

When the second Ca^{2+} ion binds to the $Ca(UO_2)(CO_3)_3^{2-}$ complex the total CN of equatorial oxygen around uranium remains at 6 in both pure water and 0.1 M NaCl (Figure 4-9b). The bidentate coordinated structures of the tricarbonate coordination (Figure 4-10c and Figure 4-10d) are quite stable in the production run (5 ns) with the occurrence probability of 83%. This indicates that binding with two Ca^{2+} ions stabilize the binding between UO_2^{2+} and the three CO_3^{2-} groups in

both pure water and 0.1 M NaCl. In $Ca(UO_2)(CO_3)_3^{2-}$, the Na^+ ion distorts one CO_3^{2-} group from bidentate to monodentate binding (Figure 4-10b); with the additional stabilization by the second Ca^{2+} ion, now the three carbonates remain bidentate binding in $Ca_2(UO_2)(CO_3)_3$, while the presence of Na^+ enhance the asymmetry of the binding of Ca^{2+} ions as shown in Figure 4-10b.

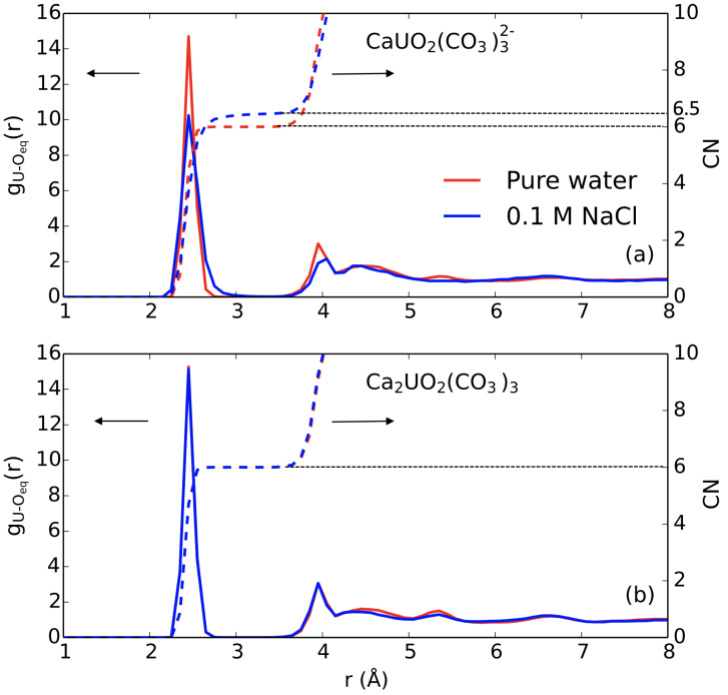

Figure 4-9 The radial distribution function (solid lines) and coordination number (CN; dashed lines) of the oxygen atoms (except the uranyl oxygens) around U atom in pure water (red color) and 0.1 M NaCl (blue color): (a) $Ca(UO_2)(CO_3)_3^{2-}$; (b) $Ca_2(UO_2)(CO_3)_3$.

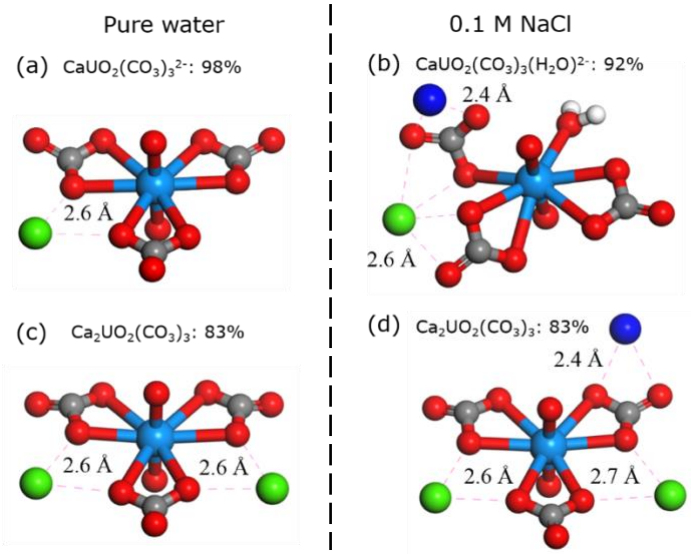

Figure 4-10 The most probable structures of $CaUO_2(CO_3)_3^{2-}$ and $Ca_2UO_2(CO_3)_3$ in pure water and in 0.1 NaCl. Percentage value indicates the probability of the structure. Some $O_{carbonate}$–Ca^{2+} and $O_{carbonate}$–Na^+ distances are shown. Color code: U, light blue; O, red; C, grey; Na, dark blue; H, white.

4.3.5 *Competition of Na^+ ions and Ca^{2+} ions for binding with $UO_2(CO_3)_3^{4-}$*

Although it is well known that $Ca_2UO_2(CO_3)_3$ is the main species of uranium in seawater, the role of Na^+ ions in $Ca_2UO_2(CO_3)_3$ formation as discussed above does prompts the question how competitive Na^+ ions are in binding with $UO_2(CO_3)_3^{4-}$ in comparison with Ca^{2+}. To address this question, we first consider each association reaction separately: $\Delta G_1 = -9.8$ kcal/mol for Eq. (4.3) and $\Delta G_2 = -20.0$ kcal/mol for Eq. (4.4):

$$Na^+ + UO_2(CO_3)_3^{4-} = NaUO_2(CO_3)_3^{3-} \quad (4.3)$$

$$Ca^{2+} + UO_2(CO_3)_3^{4-} = CaUO_2(CO_3)_3^{2-} \quad (4.4).$$

Eq. (4.5) below is the competing reaction and its $\Delta G_3 = \Delta G_1 - \Delta G_2 = 10.2$ kcal/mol. We computed the $[NaUO_2(CO_3)_3^{3-}]/[CaUO_2(CO_3)_3^{2-}]$ ratio at equilibrium in 298 K seawater by using ΔG_3 and $[Ca^{2+}] = 0.01$ M and $[Na^+] = 0.46$ M. We found the ratio to be 1.71×10^{-6}; in other words, the binding of Na+ with $UO_2(CO_3)_3^{4-}$ is negligible.

$$Na^+ + CaUO_2(CO_3)_3^{2-} = NaUO_2(CO_3)_3^{3-} + Ca^{2+} \quad (4.5)$$

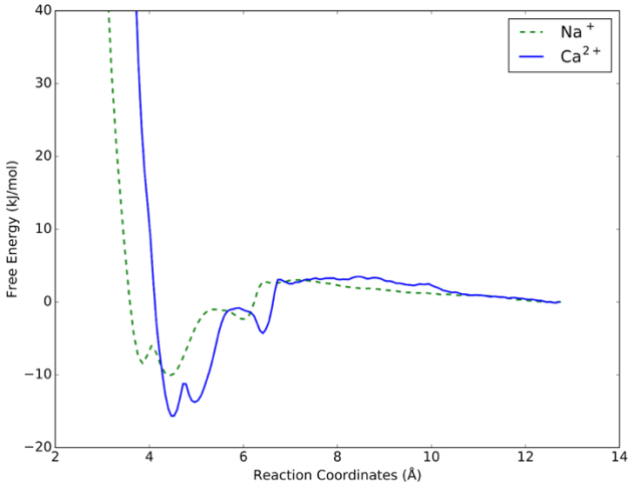

Figure 4-11 The free energy profile of the binding of Na^+ (green dashed line) and Ca^{2+} (blue solid line) with $UO_2(CO_3)_3^{4-}$ in pure water.

4.4 Conclusions

The sequential processes of UO_2^{2+} binding with the three CO_3^{2-} groups and the two Ca^{2+} ions in pure water and in 0.1 M NaCl have been simulated by classical molecular dynamics with both the non-constrained brute-force approach and umbrella sampling. We found that the three CO_3^{2-} groups and two Ca^{2+} ions spontaneously bind to UO_2^{2+} to form the $Ca_2(UO_2)(CO_3)_3$ complex; the process is faster in pure water than in 0.1 M NaCl. The simulated free energies for the five steps in pure water and 0.1 M NaCl show excellent agreement with the experiment. The coordination structures of $UO_2(CO_3)_3^{4-}$ and $CaUO_2(CO_3)_3^{2-}$ were found to be significantly affected by the presence of Na^+ ions, leading to a monodentate binding of a carbonate group to U and a water molecule entering the first coordination shell of U. The structure of the $Ca_2(UO_2)(CO_3)_3$ complex was less affected by the Na^+ ion. Our free-energy simulations based on classical molecular dynamics simulations revealed the important roles of Na^+ ions in the association of UO_2^{2+}, CO_3^{2-}, and Ca^{2+} ions in an aqueous solution.

5 Uranyl-Glutardiamidoxime Binding from First Principles Molecular Dynamics, Classical Molecular Dynamics, and Free-Energy Simulations

5.1 Introduction

Following the discussions in Chapter 4, the low concentration and relatively strong uranyl-carbonate interaction present a great challenge for uranium seawater extraction. State-of-the-art technology employs a polymeric sorbent grafted with amidoxime ligands.[72,73] However, some transition-metal ions present in seawater compete against uranium for binding with the amidoxime ligands, especially vanadium.[74]

Two methods have been developed to graft amidoxime ligands on a polymer-fiber sorbent: radiation induced graft polymerization (RIGP) and atom transfer radical polymerization (ATRP).[75,76] In RIGP, copolymerization of acrylonitrile (AN) and monomers such as substituted acrylic acids happens on the surface of electron-radiated polyethylene fiber, followed by reaction with hydroxylamine that converts the –CN group to the amidoxime groups.[77] It has been suggested that, based on the reaction between acrylonitrile and hydroxylamine and the subsequent base conditioning, both open and cyclic forms of amidoxime exist on the fiber surface. Considering these two amidoxime configurations, multiple possible coordination motifs with uranyl have been proposed, including monodentate or η^1 through the oxime oxygen, bidentate through the oxime oxygen and the amine nitrogen, η^2 or side-on coordination through the N–O oximate bond. Recent extended X-ray absorption fine structure (EXAFS) studies suggest that fiber samples after contact with seawater show chelating binding interactions or a possible of mixed binding modes, instead of the η^2 mode.[78]

Although limited insight has been obtained for the real fiber sample regarding the binding mode, great progress has been made with small-molecule model ligands. For mono amidoxime ligands, both single-crystal structures and quantum-mechanical calculations have found η^2 binding mode to uranyl.[12,79] Since the amidoxime ligands are formed from reaction of hydroxylamine with polyacrylonitrile, dioxime or diamidoxime ligands are a better model for the real sorbent. Rao et al. used two model ligands, glutarimidedioxime (H_2A) and glutardiamidoxime (H_2B), to represent the cyclic imide dioxime and the open-chain diamidoxime, respectively. They obtained binding free energies between the small-molecule ligands and the uranyl by potentiometry. For the cyclic H_2A, they were able to crystalize the complex and found that two HA^- ligands coordinate to UO_2^{2+} equatorially in a tridentate mode.[3,5,80] For the open H_2B, they could not obtain a single crystal structure.[5] So the binding mode of glutardiamidoxime (H_2B) and its deprotonated forms with uranyl remains unknown.

Since the cyclic form binds to vanadium very strongly,[81] the open-chain or acyclic form has been suggested to give higher uranium/vanadium selectivity[75] and it is important to find out the binding mode between H_2B and uranyl that might shed light on the U/V selectivity. Toward this end, our work focuses on providing a thorough computational analysis to assist in determining H_2B binding mode to uranyl complex from both first principles and classical molecular dynamics simulations. More importantly, we will explicitly consider the solvation environment including both the water molecules and the Na^+/Cl^- ions. To validate our computational models, we will also compare the simulated binding free energies with the experiment to further check the viability of our models.

5.2 Computational Methods

5.2.1 First principles molecular dynamics

First-principles density functional theory (DFT) molecular dynamics (MD) via the Born-Oppenheimer approximation was performed using Vienna *ab initio* simulation package (VASP).[26,27] The Kohn–Sham equations are solved with the all-electron projected augmented wave (PAW) method.[28,29] We have chosen the Perdew–Burke–Ernzerhof (PBE) functional of the generalized-gradient approximation (GGA) for electron exchange and correlation.[30] This DFT-MD method has been employed previously to address uranyl in water.[57,82] Two ligands and one uranyl group in a 100-water periodic box at a density of 1.14 g/cm^3 was simulated by NVT at 300 K for 10 ps. It is well known that the PBE functional tends to overstructure water, leading a frozen solution eventually, so we checked the diffusivity of the water molecules not coordinating to the uranyl-ligand complex and found it to be close to 1×10^{-9} m^2/s. This is in the same order of magnitude as the measured self-diffusion coefficient of liquid water at 300 K (2.6×10^{-9} m^2/s),[83] so the water solvent remains liquid in our DFT-PBE-MD simulation at 300 K.

5.2.2 Gas-phase quantum mechanical calculations

DFT calculations of isolated molecular complexes were performed with the TURBOMOLE package V6.5 with GGA-PBE functional along with the def-TZVP basis set, including def-ECP for uranium (listed in Supporting Information) and the resolution of the identity (RI) formalism with the corresponding auxiliary basis set.

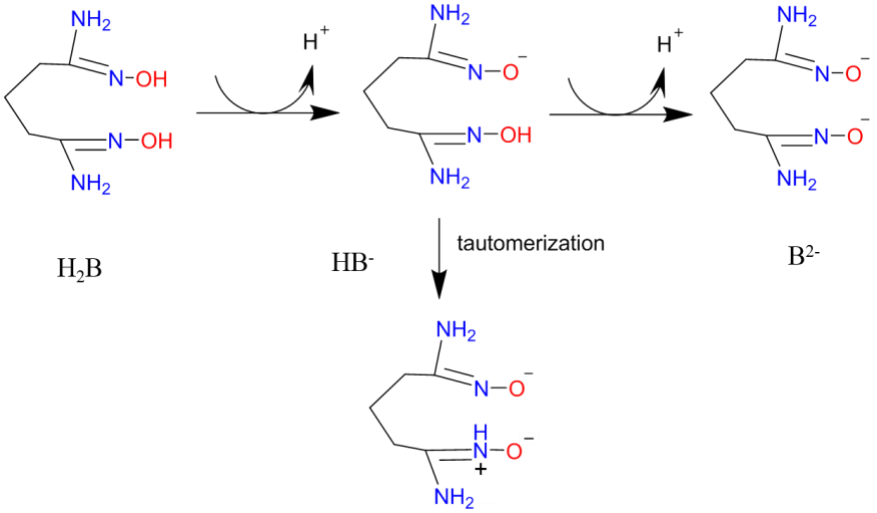

Scheme 5-1 Structures of glutardiamidoxime (H_2B) and its two deprotonated forms, HB^- and B^{2-}.

5.2.3 Classical simulation systems and force field parameters

To simulate the effect of ionic strength during MD simulations, we considered a water box where Na^+ and Cl^- ions were added to reach the experimental molar strength of 0.5 M NaCl. The TIP3P model was employed for water molecules, while the parameters for Na^+ and Cl^- ions were from a previous study.[45] The force field parameters of the solute molecules (UO_2^{2+}) and ligands (HB^- and B^{2-}; see **Scheme 5-1**) were generated from AMBER 14 GAFF force field (Generalized Amber Force Field).[42] The partial atomic charges of these solutes (UO_2^{2+}, B^{2-}, BH^-) were obtained from the restrained electrostatic potential (RESP) charge at a B3LYP level of theory[84] with 6-31G(d) basis and antechamber suite.[85] UO_2^{2+}, HB^-, and B^{2-} were placed apart from each other into a periodic water box containing 6,000 TIP3P water molecules. A cut off of 12 Å was used for non-

bonded interactions. Here we note that our uranyl force field parameters differ only slightly from and give similar performance to those from Guilbaud and Wipff.[40,86]

5.2.4 Classical molecular dynamics

First, 4000 cycles of minimization (2000 cycles of steepest descent and 2000 cycles of conjugate gradient) were carried out to relax the solvent, while solute atoms were constrained by a potential of 3000 kcal/mol-Å. Continually, a second minimization was conducted with solute atoms constrained by 500 kcal/mol-Å. A final, third minimization stage was implemented with 4000 cycles of energy minimization without constraints (2000 cycles of steepest descent and 2000 cycles of conjugated gradient). After the sequence of thorough minimizations of the solute molecule, the system was gradually heated from 0 to 300 K over a 50 ps. Then, the cell was relaxed to 1.0 g/cc with a *NPT* MD at 1 fs for 100 to 500 ps at a constant pressure of 1.0 bar and 300 K. Next, a *NVT* simulation was run for 500 ns at 300 K. All simulations were accomplished by applying the GPU-accelerated *pmemd* program in Amber 14.[51] During the production run, the temperature was kept constant using Nose-Hoover thermostat at 300 K, and the geometry of the water molecules was held fix with the SHAKE algorithm.

5.2.5 Umbrella sampling with the weighted histogram analysis method (WHAM)

To calculate free energy of binding between uranyl and the ligands, we obtained the free-energy profile via potential of mean force (PMF) with our classical MD simulations by using umbrella sampling with the WHAM method.[87] The PMF simulations were carried out in a 2,000-molecule water box in an ionic strength of I = 0.50 M NaCl solution. The reaction coordinate was taken as the distance from U to the oxime oxygen -C=N-O$^-$. The final equilibration structures were used for production simulations with no applied constraints. Umbrella sampling between 2.00 and 15.00 Å containing 75 ~ 96 windows (depending on the system) with a force constant ranging 40 – 150 kcal/mol-Å^2. At the transition states, larger force constants (100 – 150 kcal/mol-Å^2) and more windows of 0.1 Å bin size were added around the region to obtain sufficient sampling; for other regions, smaller force constants (40 – 100 kcal/mol-Å^2) were used with window sizes of 0.2 Å. Each window was equilibrated between 6 to 10 ns, where the last 5 ns was used for production. Furthermore, the binding free energy was obtained from the PMF profile by following the previous method.[36,69]

5.3 Results and discussion

5.3.1 Binding of glutardiamidoxime to uranyl in gas-phase

Previous experiments suggest that it is mainly the deprotonated forms (HB$^-$ and B^{2-} in Scheme 5-1) of glutardiamidoxime binding to uranyl.[19] To provide a baseline understanding, we first examined the gas-phase model of the binding at the DFT-PBE/def-TZVP level of theory with def-ecp for urniaum, without the solvent. We found that UO_2^{2+} and B^{2-} binds via the two –NO$^-$ groups, both in the η^2 mode (Figure **5-1**). This mode is in agreement with previous QM calculations of binding of UO_2^{2+} with amidoximate ligands.[11] To examine if the binding mode in Figure **5-1** is stable in solvation from water molecules, we used DFT-based first principles MD to examine the UO_2B complex in a 100-water supercell.

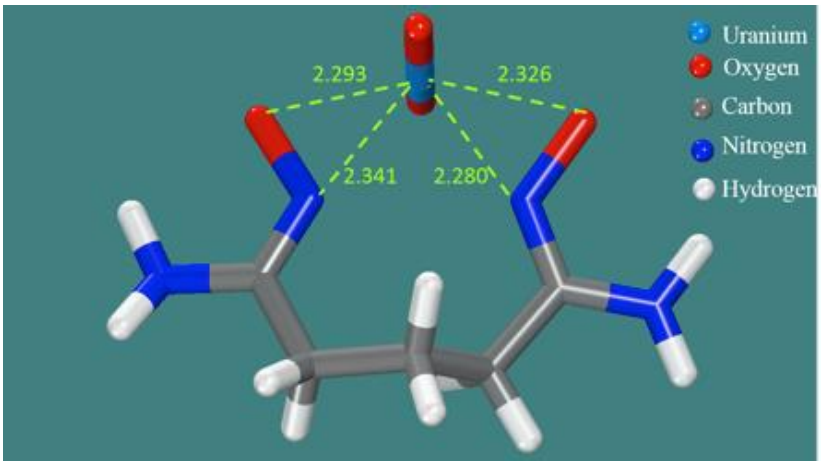

Figure 5-1 DFT-optimized gas phase structure of UO_2B where B^{2-} is double-deprotonated glutardiamidoxime (see Scheme 5-1).

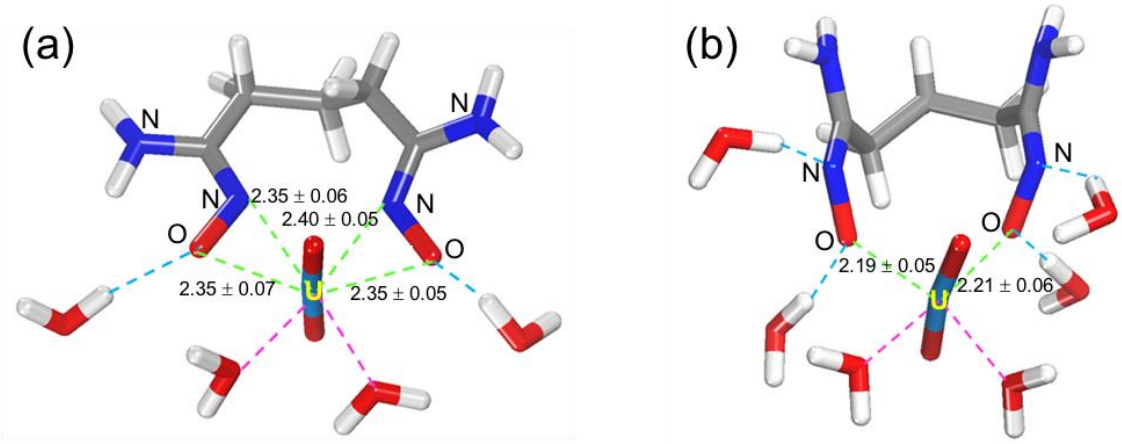

Figure 5-2 Typical structures from DFT-MD simulation of one UO_2B complex in 100 H_2O molecules: (a) the η^2-binding mode; (b) the η^1-binding mode. Average U-N and U-O distances are shown in Å.

5.3.2 First principles MD of UO_2B complex in water

Our DFT MD simulations show that the structure from Figure 5-1 (that is, the η^2 mode) can be maintained in the explicit water solvation (Figure 5-2a; black) with a slight change of the bond lengths (Figure 5-2b). However, we found that the complex with two η^1 binding modes (Figure 5-2c), which is less stable in the gas phase, now becomes more stable with the explicit solvation (Figure 5-2a; red). This means that the hydrogen-bond network now changes the energy landscape of the complex in terms of the binding mode. This can be clearly seen in Figure 5-2b and Figure 5-2c: while the oxime nitrogen (N1 and N2) is not hydrogen-bonded to water in the η^2 mode (Figure 5-2b), it is in the η^1 mode (Figure 5-2c). The preference of the oxime nitrogen to be solvated by water leads to the higher stability of the η^1 mode. In the η^2 binding mode, the O-N π bond as well as the O and N lone pairs of the oximate group dominate the interaction with U, as analyzed previously,[16] while in the η^1 binding mode the interaction is mainly via the lone pair on the O atom. To further understand the detailed binding mechanism with one additional ligand, to

include the Na^+/Cl^- ions in the simulation, and also to address the relative stabilities of the different binding modes with water solvation, DFT-MD is unable to afford the system size and timescale needed to perform the free-energy simulations. So we turned to classical MD simulations.

5.3.3 Binding of glutardiamidoxime to uranyl from classical MD

We placed UO_2^{2+} and B^{2-} ions far apart from each other in a large simulation cell to run a brute-force MD simulation for over 500 nanoseconds (ns). The binding is monitored by the U-O and U-N distances. The time evolution of the key distances is shown in Figure 5-3a, while the atom labels are shown in Figure 5-4a. The first complexation event happens at about 15 ns when one $–N-O^-$ end of the B^{2-} ligand attaches to UO_2^{2+}. Then around 35 ns, the second $–N-O^-$ end also binds to UO_2^{2+}, leading to a bidentate binding mode. Closer inspection of the U-O and U-N distances (Figure 5-3a inset) shows that the two U-O distances average at about 2.30 Å, while the two U-N distances averages at about 2.60 Å. A snapshot of the binding is shown in Figure 5-4a; one can see that the N atoms of the two oxime moieties interact with U weakly. This is further supported by the radial distribution analysis of the trajectory after the complex is formed (Figure 5-5). One can see that the N atoms of the $–N-O^-$ groups are rather loosely interacting with U, yielding an average U-N distance of 2.625 Å with a wide dispersion. This binding between the two $–N-O^-$ moieties and UO_2^{2+} (Figure 5-4 is different from the η^1 binding mode from our DFT MD results (Figure 5-2) and better described as a distorted η^2 binding mode. In addition, one can see that one $–NH_2$ group also coordinates to the uranyl in the snapshot (N3 in Figure 5-4a) with an average distance of about 2.50 Å (Figure 5-5). For comparison, the $–NH_2$ groups are not directly interacting with uranyl in our DFT-MD models (Figure 5-2). Further study such as through improving the force field is warranted to resolve this inconsistency between classical MD and DFT-MD simulations.

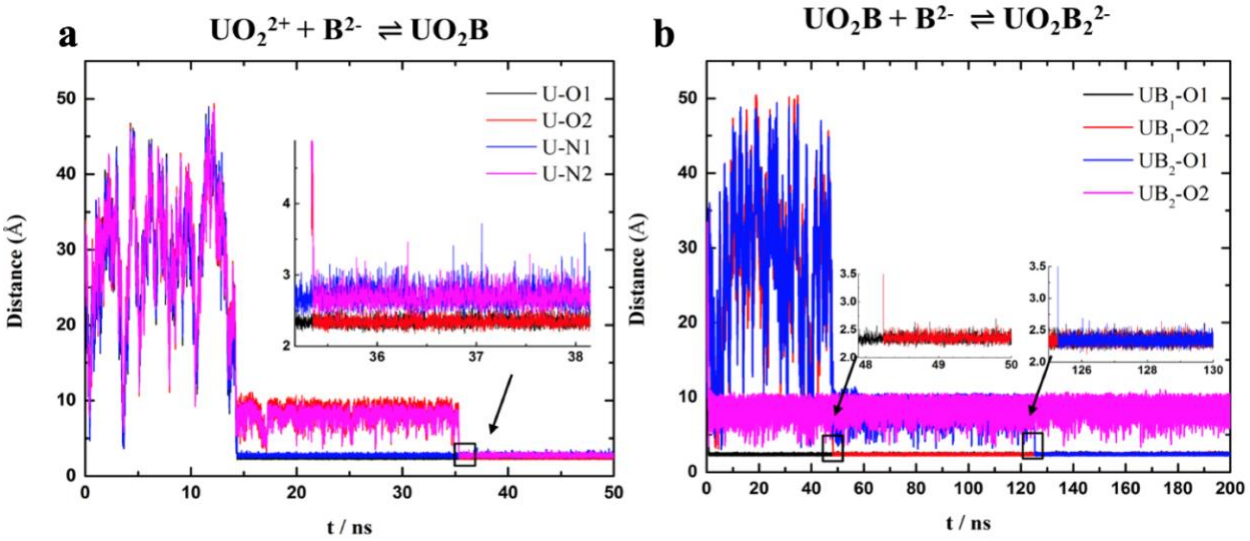

Figure 5-3 Classical molecular dynamics simulations of the binding as monitored by key U-O and U-N distances with time: (a) between UO_2^{2+} and B^{2-} ions, initially around 20 Å apart; (b) between UO_2^{2+} and two B^{2-} ions, initially about 20 Å apart, in pure water. The atoms labels for (a) and (b) are shown in Figure **5-4**a and Figure **5-4**b, respectively**.**

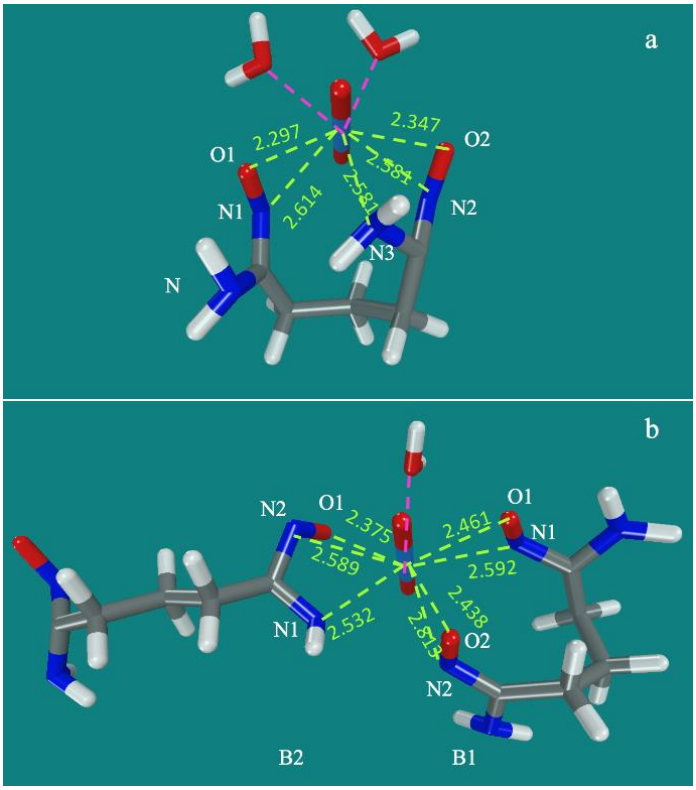

Figure 5-4 Snapshots of the binding modes after 500 ns classical MD simulations: (a) UO_2B; (b) $[UO_2B_2]^{2-}$ in pure water. Instantaneous U-N and U-O distances are labelled in Å.

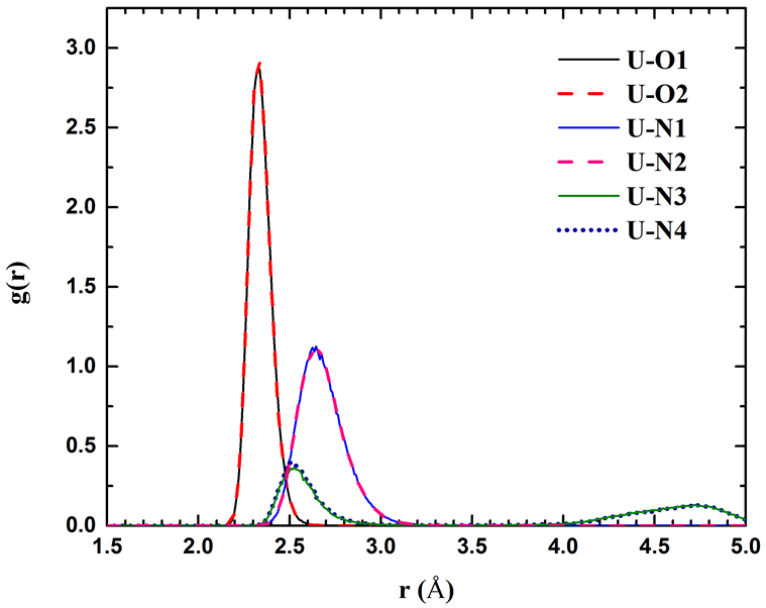

Figure 5-5 Radial distribution function of O and N atoms on the ligand around U for the structure of UO_2B in pure water after 500 ns classical MD simulation. A snapshot of the binding structure and the atom labels are shown Figure **5-4**a

Next we simulated the binding of two B^{2-} ligands with uranyl. Here we monitored the four U-O distances: two from each of the two B^{2-} ligands, B1 and B2. From Figure 5-3b, one can see that the bidentate binding with the B1 ligand is finished at 45 ns, while the B2 ligand has only one of its two O groups interacting with uranyl after 200 ns. In fact, the second ligand binds with uranyl via only one oxime oxygen after 500 ns MD simulation. Figure 5-4b shows a snapshot of the binding in the $[UO_2B_2]^{2-}$ complex. One can see that the B1 ligand (the one on the right in Figure 5-4b) binds with UO_2^{2-} in a bidentate mode (same as in the UO_2B complex) but the B2 ligand binds with one of its two amidoximate groups. The B2 ligand is rather linear with the non-binding amidoximate group extended well away for the uranyl group. One thing to note is that the $–NH_2$ group of the binding amidoximate end of the B2 ligand also weakly coordinates to U with a distance of about 2.51 Å, a mode proposed previously as the adsorption mechanism of U(VI) to amidoxime-based polymers.[88,89] In our simulation, it seems that steric effects prevent the second ligand from forming a chelating binding with both oximate ends. This could be a kinetic issue that our classical MD, despite its 500 ns run, could not overcome.

5.3.4 Gas phase and aqueous-phase structures for uranyl binding with two glutardiamidoxime ligands

The structure of the $[UO_2B_2]^{2-}$ complex as found in our classical MD simulations and shown in Figure 5-4b may not be the most stable structure of the complex in water. To explore other conformations of binding, we first compared their gas phase energetics at the DFT-PBE/def-TZVP level of theory, without the solvent. Figure 5-6a shows an isomer where the $[UO_2B_2]^{2-}$ complex binds to both B^{2-} ligands in a bidentate, η^1 mode. This isomer is metastable, and after perturbation and relaxation, the structure changes to Figure 5-6b where one B^{2-} ligand binds in a double η^2 mode and the other binds in a single η^2 mode; the energy is lowered by 2.3 eV. To see whether the structures in Figure 5-6 are stable in an aqueous solution, we put them in water and performed classical MD simulations. We found that the structure in Figure 5-6b converged to the structure in Figure 5-4b, indicating again that the normal η^2 mode is less stable in an explicit water-solvation environment and becomes distorted. More interestingly, the structure in Figure 5-6a changes to that in Figure 5-7a, indicating the preference of a distorted η^2 structure in explicit water solvation. In this distorted η^2 structure, the average U-N distance is about 2.60 Å, while the average U-O distance is about 2.33 Å (Figure 5-7b). From integrating both U-N and U-O coordination in Figure 5-7b up to 2.70 Å, we found the coordination number of U to be seven; the extra coordination beyond the normal number of six could be due to our force field. Now that we have two stable structures of the $[UO_2B_2]^{2-}$ complex in water (Figure 5-4b and Figure 5-7a), it would be interesting to compare their free energy, as discussed next.

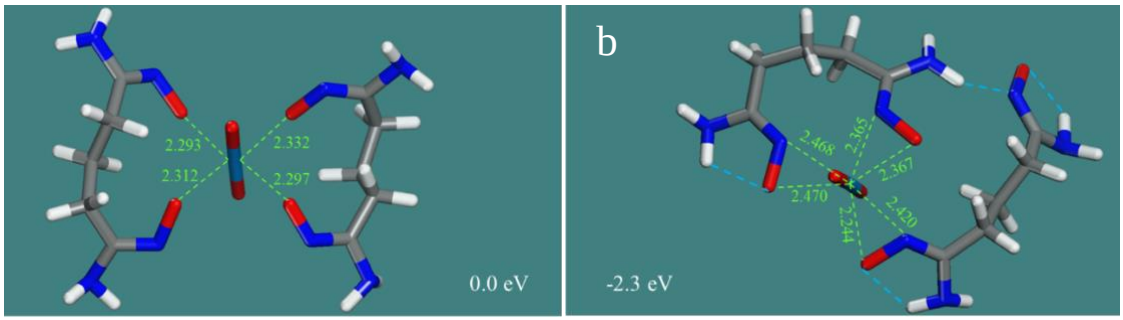

Figure 5-6 DFT-optimized gas phase structures for $[UO_2B_2]^{2-}$ (a) η^1 binding mode; (b) η^2 binding mode. The blue lines represent intramolecular hydrogen bonding.

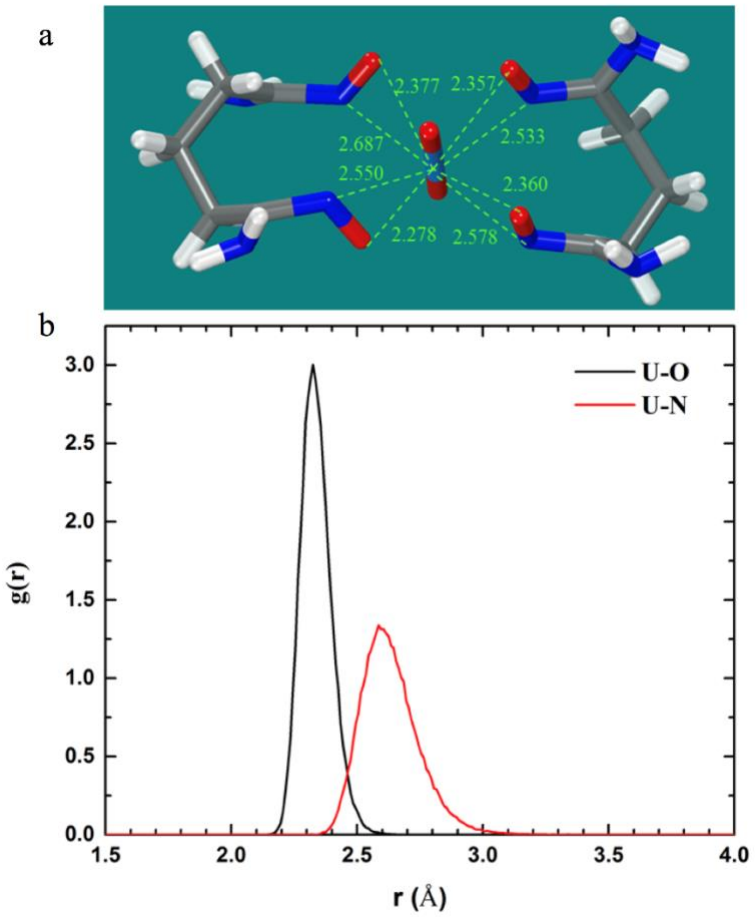

Figure 5-7 (a) A snapshot of the fourfold distorted η^2 binding structure of $[UO_2B_2]^{2-}$ after 100 ns classical MD simulation in 0.50 M NaCl; (b) the corresponding radial distribution function. Bond distances are from an instantaneous snapshot.

5.3.5 Free energy simulations of glutardiamidoxime-uranyl binding

Although there is no experimental structural information regarding the glutardiamidoxime-uranyl binding, the free energies of the sequential binding events have been measured. This provides a useful way to validate our atomistic insights from MD simulations above. Using umbrella sampling we obtained the free energy profile via the potential of mean force (PMF) for the glutardiamidoxime-uranyl binding. Figure 8 shows the free-energy profiles for the association of a single ligand (UO_2^{2+} + B^{2-}), the association of the second ligand (UO_2B + B^{2-}), and the association of UO_2B and HB^- (UO_2B + HB^-). In these simulations, we start with a bound complex and then begin to slowly pull one end of the ligand away from the uranyl using the U-O distance as a reaction coordinate. One can see that the three reactions have very similar PMF profiles. In the case of $UO_2B \rightarrow UO_2^{2+} + B^{2-}$ (red line in Figure 5-8), we started with the structure in Figure 4a and then broke the first U-O binding at about 3.0 Å with a free-energy barrier of about 45 kJ/mol; then the system reached a broad metastable or intermediate state between 4 and 10 Å, due to the flexibility of the $(CH_2)_3$ linker between the two amidoximate end groups; then the second U-O binding broke between 10 and 12 Å.

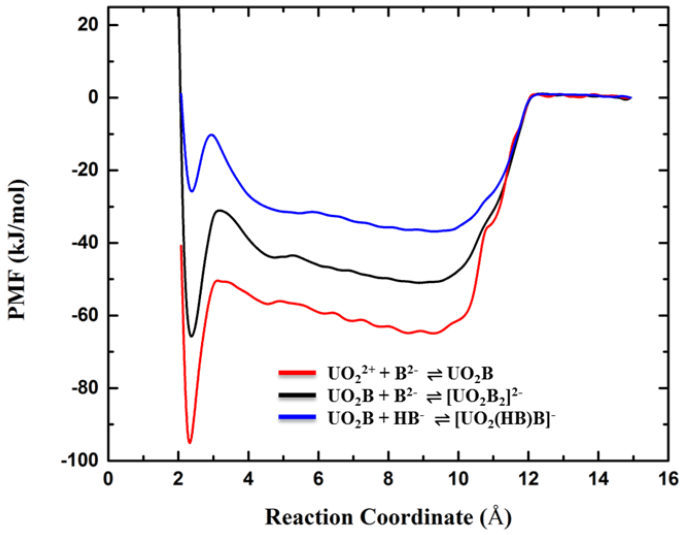

Figure 5-8 Free energy profiles from the potential of the mean force (PMF) for the binding events: $UO_2^{2+} + B^{2-}$; $UO_2B + B^{2-}$; $UO_2B + HB^-$ in 0.50 M NaCl. Reaction coordinate is defined as a U-O bond distance.

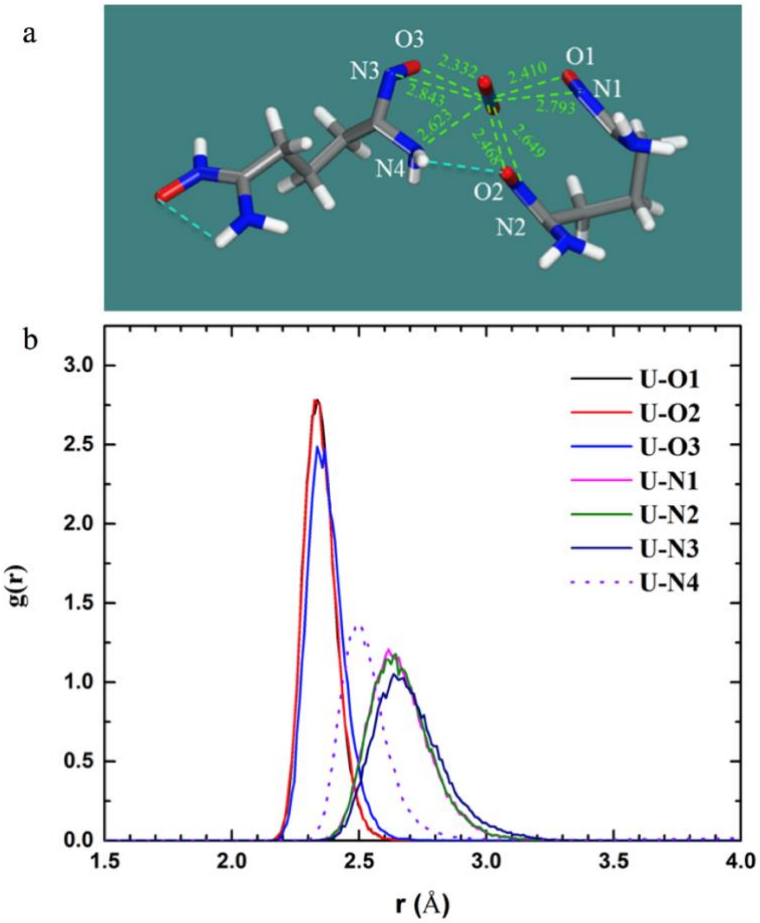

Figure 5-9 (a) Snapshot of the $[UO_2(HB)B]^-$ structure from a 50 ns classical MD simulation in 0.50 M NaCl; (b) the corresponding radial distribution function.

For the process of $[UO_2B_2]^{2-} \rightarrow UO_2B + B^{2-}$, we started with the structure for $[UO_2B_2]^{2-}$ in Figure 5-7a where both B^{2-} ligands bind in a distorted η^2 mode, corresponding to the minimum at 2.35 Å in Figure 5-8 (black line). After breaking the first U-O binding with a free-energy barrier of about 35 kJ/mol (at 3.0 Å in Figure 5-8; black line), we found that the structure changes to the configuration in Figure 5-4b, corresponding to the broad local minimum between 4 and 10 Å in Figure 5-8 whose energy is about 10 kJ/mol higher than that of the initial complex. Conversely, there is a free energy barrier of about 15 kJ/mol for the conversion of the local minimum at ~9 Å to the bound complex at 2.35 Å in Figure 5-8, which explains why such tightly bound mode of binding was not formed during the brute-force MD simulation of the binding of UO_2^{2+} with two B^{2-} ligands (Figure 5-3b).

Since Tian et al. showed that the most abundant species at seawater pH (8.3) is $[UO_2(HB)B]^-$,[5] we performed brute-force MD simulation of UO_2^{2+} with two faraway B^{2-} and HB^- ligands and found that the B^{2-} ligand binds first followed by the HB^- ligand, in agreement with the stronger electrostatic attraction between UO_2^{2+} and B^{2-}. The brute-force MD yielded a binding mode as shown in Figure 5-9a, which corresponds to a reaction coordinate of 9 Å in Figure 5-8 (blue line). One can see that the oximate end of the HB^- ligand binds to UO_2^{2+} in a chelating mode with an average U-NH_2 distance of 2.50 Å and U-O distance of 2.30 Å (Figure 5-9b), while B^{2-} binds with two distorted η^2 modes. We also explored the configuration with the fourfold complexation mode for $[UO_2(HB)B]^-$, which corresponds to a reaction coordinate of 2.35 Å in Figure 5-8 (blue line). Interestingly, unlike the case in $[UO_2B_2]^{2-}$, this configuration of fourfold complexation is less stable than the threefold binding mode (Figure 5-9a) for $[UO_2(HB)B]^-$.

We note that the H atom is placed on the N atom of the oxime group of HB^- in Figure 5-9a (left end). This tautomerized form of oxime (see Scheme **5-1**) has been proposed for $[UO_2(HB)B]^-$ by Tian et al. for the bound state.[19] We compared it with the untautomerized form (H on the O atom of oxime) for the step of the oxime end of HB^- binding with UO_2B. We found that the tautomerized form binds stronger by 15 kJ/mol than the untautomerized form, leading to a more stable $[UO_2(HB)B]^-$. This is why we used the tautomerized form of the oxime group in HB^- for our free energy simulations of $[UO_2(HB)B]^-$ formation. In the configuration of fourfold complexation (at 2.35 Å in Figure 5-8, blue line) of the bound state, the tautomerized form of the oxime group in HB^- binds to U via the η^1 mode through the O atom, while the oximate end of HB^- and B^{2-} bind to U via the distorted η^2 mode. In the free or unbound state of the oxime group in HB^- (Figure 5-9a), the untautomerized form (H on the O atom of oxime) is more stable; here we use the tautomerized form (H on the N atom of oxime) instead so that we can compare the free-energy difference between the free (Figure 5-9a) and bound states with classical MD simulations that cannot describe the proton transfer or the tautomerization process. We hope to use DFT MD simulations to determine the free energy of the tautomerization process of the amidoxime group in the future.

5.3.6 Comparison of simulated free energies with experiment

From the PMF profiles in Figure 5-8, we then followed an integration protocol from Chialvo et al.[34] to obtain the binding free energies. Table 5-1 compares the free energies for the three binding events from our simulations against the experimental values. One can see that very good agreement has been obtained for all three binding events. We consider this a strong indication that our classical MD simulations could well capture the binding thermodynamics. This also in turn lends support to the binding modes as found above between UO_2^{2+} and B^{2-}. One can see that

the first B^{2-} ligand binding is very strong, while the binding strength reduces by half for the second B^{2-} ligand. Binding of UO_2B with HB^- slightly weaker than with B^{2-}.

Table 5-1 Comparison of experimental and simulated free energies of binding between uranyl and the glutardiamidoxime (H_2B) ligand at 298 K in 0.5 NaCl aqueous solution.

Reaction	$\Delta G_{Exp.}$ (kJ/mol) [19]	$\Delta G_{Calc.}$ (kJ/mol)
$UO_2^{2+} + B^{2-} \rightleftharpoons UO_2B$	-98.7	-91.9 ± 6.8
$UO_2B + B^{2-} \rightleftharpoons [U\,O_2B_2]^{2-}$	-50.2	-55.3 ±5.1
$UO_2B + HB^- \rightleftharpoons [UO_2(HB)B]^-$	-39.8	-37.8± 2.0

5.3.7 Implications for the experiment.

The η^2 mode has been suggested by previous gas phase and implicit-solvation models and also found in several single crystal structures.[11,90] Our work shows that the aqueous solvation environment could be very different from those cases. On the other hand, the glutardiamidoxime ligand is a very simplified model compared to the real ligand binding environment in the polymeric sorbent, and more complex ligand models need to be developed to consider the carboxylate group and a mixture of cyclic and open-chain configurations. The combined approach here shows a promising way to simulate the binding of such complex ligands with uranyl, although more work is needed to further improve the force field for a consistent picture between classical MD and DFT MD simulations.

5.4 Conclusions

In summary, we have used a suite of computational methods to shed light on the binding between uranyl and glutardiamidoxime (H_2B), an important model ligand with an open-chain conformation. From our molecular dynamics (MD) simulations solvent as well as the Na^+ and Cl^- ions, we found that the binding configurations of B^{2-} with uranyl favor the twofold distorted η^2 binding between the oximate ends (C=N-O^-) and U, while HB^- prefers the chelating mode for the oximate end with the neutral end being solvated by water. We simulated the free energies of sequential ligand binding to form UO_2B, $[UO_2B_2]^{2-}$, and $[UO_2(HB)B]^-$ with umbrella sampling. Very good agreement with the experimental values was achieved, which corroborates our structural insights into the binding mode. The free-energy profiles as a function of the U-O distance from the potential-of-mean-force simulations showed similar features of a loose intermediate state separated from the tight-binding state by a sizable barrier (15 to 25 kJ/mol). Hence the present work revealed key structural and thermodynamic insights into the binding between uranyl and an open-chain amidoxime ligand in a simulated seawater that will be useful for further understanding of uranium extraction from the sea in a more realistic ligand and solvation environment.

6 Understanding the Binding of a Bifunctional Amidoximate-Carboxylate Ligand with Uranyl in Seawater

6.1 Introduction

Besides the favorable binding configurations discussed in Chapter 5, the incorporation of an carboxylic acid co-monomer into the poly(amidoxime) adsorbents has also been shown to increase uranium uptake.[77,91] Experimentalists have optimized the molar ratio of amidoxime to carboxylate.[75,76] Research suggests that the enhancement of uranium recovery from the bifunctional ligand containing both AO^- and Ac^- could be due to a synergetic effect. Density functional theory calculations with implicit solvation models have been performed to unveil this synergetic effect; some have shown that a protonated carboxylate is conducive to the dissociation of the uranium-carbonate complex.[51,79,92] But the explicit solvation environment, important in uranyl speciation and ligand displacement, has not been considered.

This work aims to shed light on the synergetic effect between amidoxime and carboxylate groups in binding with uranyl, by using a model ligand and an explicit solvation environment. Especially, classical molecular dynamic (CMD) simulations coupled with free-energy methods (umbrella sampling with the weighted histogram analysis method)[93] will be utilized to investigate the modes and thermodynamics of the binding in a simulated seawater condition. Moreover, gas-phase quantum mechanical calculations and ab initio MD simulations have also been performed to provide a baseline understanding.

6.2 Computational methods

6.2.1 Ab initio molecular dynamics

Ab initio molecular dynamics (MD) via the Born-Oppenheimer approximation and DFT was performed using Vienna ab initio simulation package (VASP).[26,27] The Kohn−Sham equations were solved with the all-electron projected augmented wave (PAW) method.[28,29] We chose the Perdew−Burke−Ernzerhof (PBE) functional of the generalized-gradient approximation (GGA) for electron exchange and correlation.[30] Two ligands and one uranyl group in a 100-water periodic box at a density of 1.11 g/cm^3 was simulated by NVT at 300 K for a total of 20 ps with the last 10ps data for analysis.

6.2.2 Gas phase analysis

Density functional theory (DFT) calculations of isolated molecular complexes were performed with the TURBOMOLE package V6.5 with the GGA-PBE functional along with the def-TZVP basis set, including def-ECP for uranium and the resolution of the identity (RI) formalism with the corresponding auxiliary basis set.

6.2.3 Classical molecular dynamics

To simulate the effect of ionic strength during MD simulations, we considered a water box where Na^+ and Cl^- ions were added to reach the molar strength of 0.5 M NaCl for a simulated seawater condition. The TIP3P model was employed for water molecules, while the parameters for Na^+ and Cl^- ions were from a previous study.[45] The force field parameters of UO_2^{2+} and the bifunctional ligand were generated from the AMBER 16 GAFF force field (generalized AMBER force field).[42] The partial atomic charges were obtained from the restrained electrostatic potential (RESP) charge at the B3LYP[84] level of theory with 6-31G(d) basis and antechamber suite.[85] UO_2^{2+} and the bifunctional ligand were placed apart from each other into a periodic water box containing

2000 TIP3P water molecules. A cutoff of 12 Å was used for nonbonded interactions. Typical input files for our classical MD simulations including all force field parameters are provided in the SI.

To prepare the system for MD simulations, 4000 cycles of minimization (2000 cycles of steepest descent and 2000 cycles of conjugate gradient) were first carried out to relax the solvent, while solute atoms (uranyl and the ligand) were constrained by a potential of 3000 kcal/(mol Å). Then, a second minimization was conducted with solute atoms constrained by 500 kcal/(mol Å). A final, third minimization stage was implemented with 4000 cycles of energy minimization without constraints (2000 cycles of steepest descent and 2000 cycles of conjugated gradient). After the sequence of thorough minimizations of the solute molecule, the system was gradually heated from 0 to 300 K over 50 ps. Then, the cell was relaxed to 1.0 g/cm^3 with an NPT MD at 1 fs for 100−500 ps at a constant pressure of 1.0 bar and 300 K. Next, an NPT simulation was run for 500 ns at 300 K. All simulations were accomplished by applying the GPU-accelerated pmemd program in Amber 16.[51] During the production run, the temperature was kept constant using a Nose−Hoover thermostat at 300 K, and the geometry of the water molecules was held fix with the SHAKE algorithm.

6.2.4 Umbrella sampling and weighted histogram analysis method (WHAM)

To calculate the free energy of binding between uranyl and the ligand, we obtained the free-energy profile via the potential of mean force (PMF) with our classical MD simulations by using umbrella sampling with the WHAM method.[87] The reaction coordinate was taken as the distance from U to the oxime oxygen −C=N−O$^-$. Umbrella sampling between 2.00 and 15.00 Å containing about 80 windows (depending on the system) was carried out with a force constant ranging from 80 to 300 kcal/(mol Å^2). At the transition states, larger force constants (200−300 kcal mol^{-1} Å^{-2}) and more windows of 0.1 Å bin size were added around the region to obtain sufficient sampling; for other regions, smaller force constants (80−200 kcal mol^{-1} Å^{-2}) were used with window sizes of 0.2 Å. Each window was equilibrated for 2 ns, where the last 1 ns was used for statistics. Furthermore, binding free-energy was calculated from the constructed PMFs following previous methods.[36,69]

6.3 Results and discussion

6.3.1 Structure of the bifunctional model ligand.

Since it is the deprotonated form of an amidoxime or carboxylic group that binds with uranyl, our model ligand simply comprises an amidoximate group and an acetate group connected by the –$(CH_2)_3$– linker (Figure 6-1). So the bifunctional ligand has an overall charge of -2 and is denoted as AcAO.

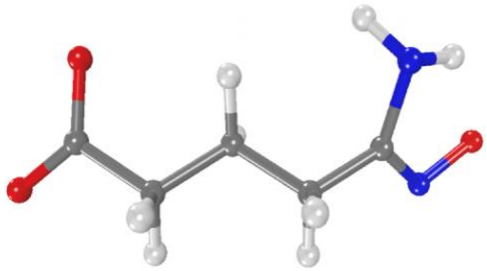

Figure 6-1 DFT-optimized gas-phase structure of the dianionic bifunctional ligand, denoted as AcAO. The ligand consists of carboxylate or substituted acetate (Ac^-, left) and amidoximate (AO^-, right) functional groups. C, gray; O, red; N, blue; H, white. Same color scheme is used in subsequent figures.

6.3.2 *Binding of uranyl with one bifunctional AcAO ligand in the gas phase.*

Various binding modes of a single bifunctional ligand to uranyl (including the coordination by water molecules) are compared in Figure 6-2. The most stable configuration (Figure 6-2a) consists of a bifunctional, chelate binding: AO^- in η^2 mode and Ac^- in monodentate mode. In the second most stable configuration, the binding mode of AO^- in η^2 changes to η^1 and the energy is 0.21 eV higher (Figure 6-2b). The mono-functional binding configurations (with either AO^- or Ac^- end) have much higher energies. We also tested an initial structure of the chelate binding with the Ac^- group in the bidentate mode but found it relaxed to the monodentate mode. For comparison, we further examined the dianionic CO_2-$(CH_2)_3$-CO_2 ligand with two carboxylate group and found that the chelate monodentate mode (Figure 6-2c) is also more stable than the bidentate mode (Figure 6-2d) in this case.

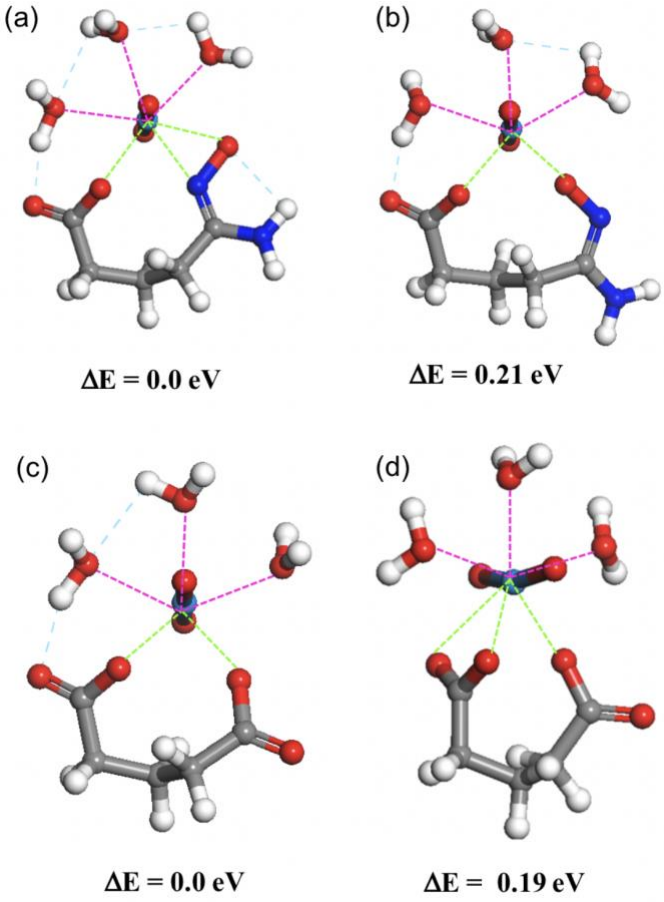

Figure 6-2 (a) and (b) two optimized structures and their relative energies (DFT-PBE/def-TZVP) of the $UO_2AcAO(H_2O)_3$ complex in gas phase, where AcAO is the dianionic bifunctional ligand in Figure **6-1**. (c) and (d) two optimized structures and their relative energies of the $UO_2AcAc(H_2O)_3$ complex in gas phase, where AcAc is the dianionic CO_2-$(CH_2)_3$-CO_2 ligand. Coordination bonds to the U atom (sky blue) in the uranyl group are indicated by the dashed lines.

6.3.3 *Ab initio molecular dynamics simulation of the UO_2AcAO complex in water.*

To gauge the stability of the UO_2AcAO complex in an explicit solvent model, we have performed AIMD simulations at the DFT-PBE level. This approach has been used recently in the binding of uranyl with ligands in water.[57,94] Figure 6-3a shows a snapshot of the most stable gas-phase configuration of the UO_2C complex after a 10 ps production simulation in a pure water box.

One can see that the gas-phase geometry of the most stable configuration is well maintained in water. The first solvation shell shows how the water molecules hydrogen bond with oximate-oxygen, uranyl oxygens, and carboxylate oxygen. In addition, two water molecules are coordinated to U. Figure 6-3b shows radial distribution functions for the η^2 mode of the AO^- group and the monodentate mode of the Ac^- group in coordination to U: the uranyl-carbonate-oxygen (U-Oc) is predominately at 2.25 Å, the uranyl-oximate-oxygen (U-Oox) at 2.30 Å, and the uranyl-oximate-nitrogen (U-Nox) at 2.38 Å.

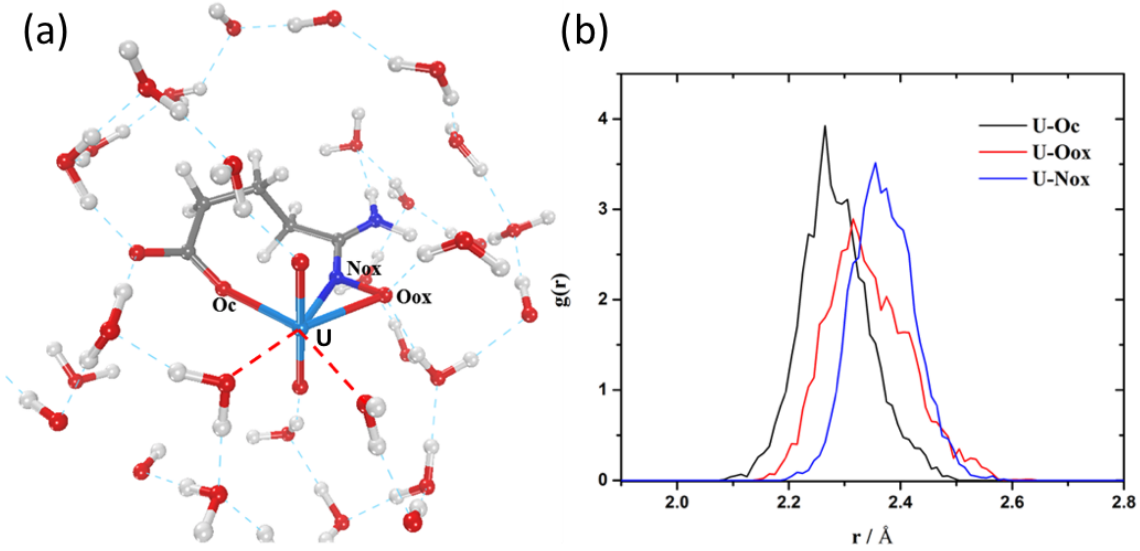

Figure 6-3 (a) A snapshot of the UO_2AcAO complex in water from ab initio MD (DFT-PBE). (b) Radial distribution functions of the ligand binding sites around U.

6.3.4 Binding of uranyl with two bifunctional AcAO ligands in the gas phase.

The equatorial coordinate sites occupied by water molecules in the UO_2AcAO complex (Figure 6-3a) can further bind with one more AcAO ligand. Figure 4 shows the different types of binding configurations for the two AcAO ligands with one uranyl and their relative energies in the gas phase. Both cis-/trans- and and η^2/η^1 AO configurations were considered. Interestingly, one can see that the four most stable configurations of $[UO_2(AcAO)_2]^{2-}$ all have very similar energies (within 0.10 eV). To test stability of these configurations in a simulated seawater, we performed CMD simulations of the complex in a 0.5 M NaCl solution.

6.3.5 Classical MD simulations of binding of uranyl with two bifunctional AcAO ligands in 0.5 M NaCl.

We found that the cis-configuration (Figure 6-4a) is stable in the 0.5 M NaCl solution, therefore a local minimum on the free-energy surface. More interestingly, we found that all the three trans-configurations (Figure 6-4b-d) converged into the trans-bis(η^2-AO) configuration (Figure 6-4c). Hence in 0.5 M NaCl, the $[UO_2(AcAO)_2]^{2-}$ complex can exist in two states. To evaluate the relative stability, we used umbrella sampling to obtain the potential-of-mean-force (PMF) and binding free energies for the two configurations.

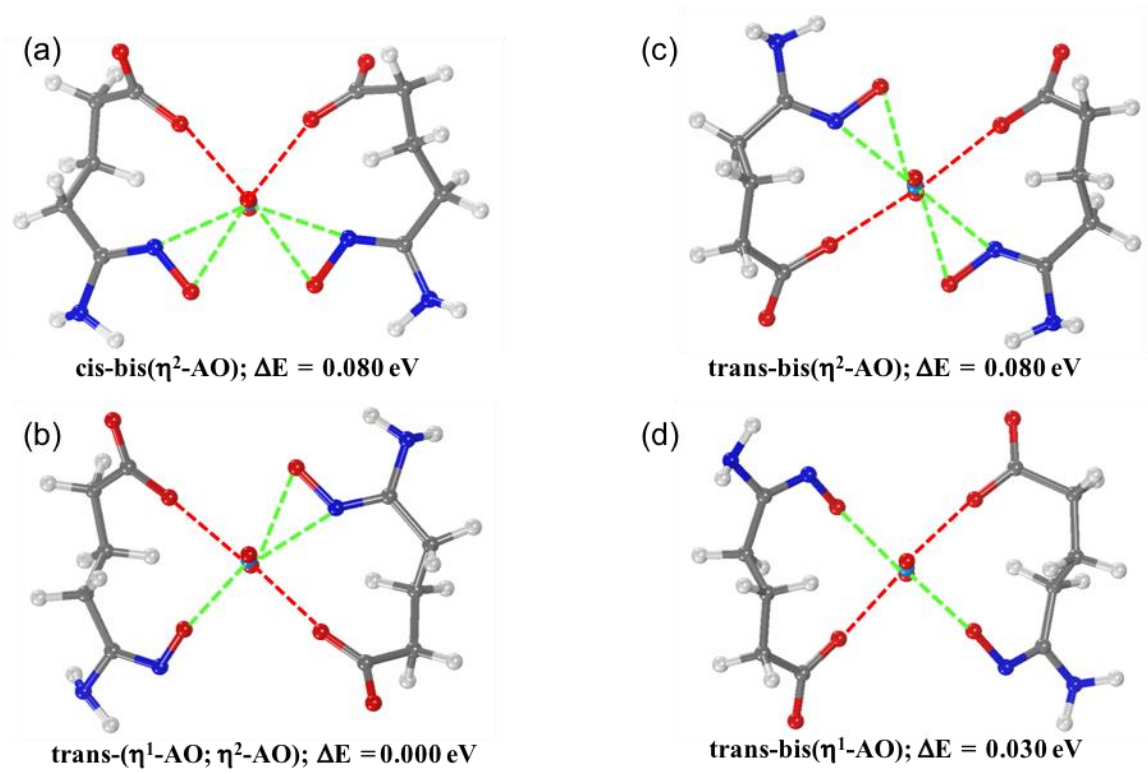

Figure 6-4 DFT-optimized gas-phase structures and relative energies (DFT-PBE/def-TZVP) of the $[UO_2(AcAO)_2]^{2-}$ complex with different cis-/trans- and η^2/η^1 AO configurations. Coordination bonds to the U atom (sky blue) in the uranyl group are indicated by the dashed lines.

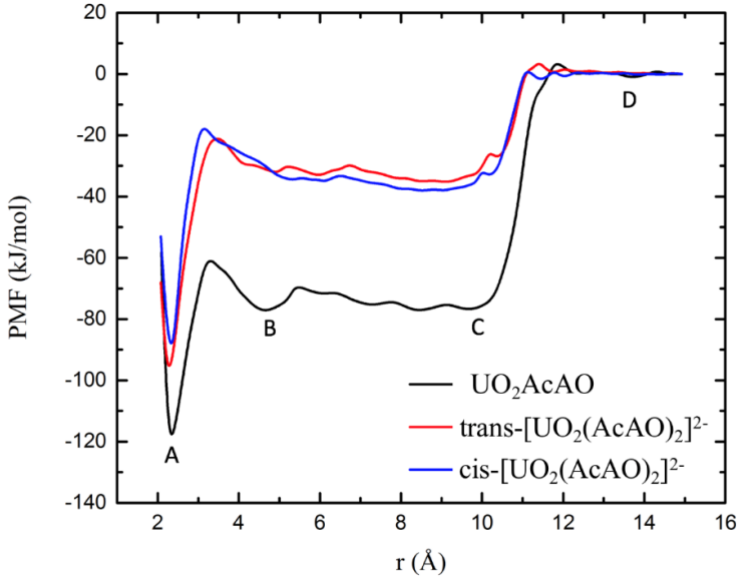

Figure 6-5 The potential-of-mean-force for sequential formations of the UO_2AcAO complex (black line) and the $[UO_2(AcAO)_2]^{2-}$ complex (from UO_2AcAO and $AcAO^{2-}$) for both the cis- (blue line) and trans- (red line) configurations in 0.5 M NaCl. The distance (*r*) between U and the oximate O on the ligand is defined as the reaction coordinate.

6.3.6 *Potential-of-mean-force (PMF) and free energies of binding for uranyl with the bifunctional ligands in 0.5 M NaCl*

Figure 6-5 shows the PMFs for sequential formations of the UO_2AcAO complex as well as both the cis- and trans-configurations of the $[UO_2(AcAO)_2]^{2-}$ complex (from UO_2AcAO and $AcAO^{2-}$). The distance between U and the oximate O on the ligand is the reaction coordinate. We first examine the formation of the UO_2AcAO complex, following the positions D → C → B → A in Figure 6-5. Initially, UO_2^{2+} and the AcAO ligand are far away from each other (Figure 6-6D); as they come closer, one carboxylate O first binds with U (Figure 6-6C); the broad minimum from C → B in Figure 6-5 represents the approaching of the AO end of the AcAO ligand toward U, finally reaching a solvent-shared state (Figure 6B); from B → A, the AO group displaces a water molecule to bind with U and the process has to overcome a barrier of 16 kJ/mol but has a favorable free-energy change of -40 kJ/mol.

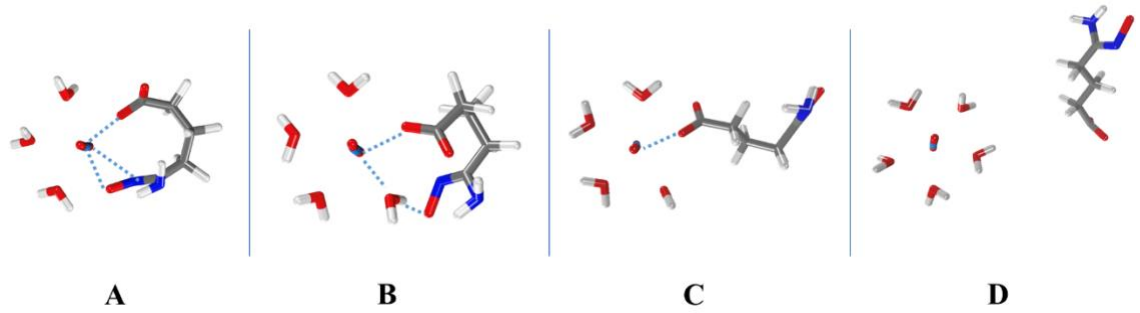

Figure 6-6 Snapshots during formation of the UO_2AcAO complex along the free-energy profile (positions are indicated in Figure **6-5**, black line). Coordination bonds to the U atom (sky blue) in the uranyl group are indicated by the dashed lines.

The binding of the second AcAO ligand to uranyl (namely, formation of the $[UO_2(AcAO)_2]^{2-}$ complex from UO_2AcAO and $AcAO^{2-}$) follows a similar process as the binding of the first AcAO ligand. In other words, the carboxylate group binds first, leading to a loose-binding intermediate state with a broad local minimum; then it overcomes a free-energy barrier, to reach a more stable, tight-binding chelate state. The difference here between the first and second binding events is that the second binding is weaker, which is expected, because the first binding is between a dication and a dianion while the second binding is between a neutral complex and a dianion. Figure 6-5 further shows that the trans-configuration of the $[UO_2(AcAO)_2]^{2-}$ complex is slightly more stable than the cis-configuration by 7 kJ/mol, so our free energy analysis below is based on the more stable trans-configuration.

From the PMF curves in Figure 6-5, we obtained the free energies for the sequential binding of uranyl with the AcAO ligands. The results are shown in Table 6-1. One can see that binding of the first AcAO ligand has a free energy of -117 kJ/mol, while binding of the second AcAO ligand has a free energy of -87 kJ/mol, leading to a sum of -202 kJ/mol for complexation of uranyl with two AcAO ligands. Previously, we obtained the free energies for the sequential binding of uranyl with the $[AO(CH_2)_3AO]^{2-}$ ligands which are shown for comparison in Table 6-1.[93] One can see for both steps, the bifunctional AcAO ligand has a strong binding with uranyl than the $[AO(CH_2)_3AO]^{2-}$ ligand, leading to a more favorable interaction of -55 kJ/mol for the total free energy change.

Since uranyl exists mainly as the neutral $Ca_2[UO_2(CO_3)_3]$ species in seawater,[3-5] we also determined the binding free energies starting with $Ca_2[UO_2(CO_3)_3]$. Here we considered the scenario that two incoming ligands completely displace Ca^{2+} and CO_3^{2-} ions around UO_2^{2+}.

Combining the free-energy values in Table 6-1 and the binding free energies of Ca^{2+}, UO_2^{2+}, and CO_3^{2-} to form $Ca_2[UO_2(CO_3)_3]$ from our earlier work, [74,95] we obtained the free energies for the displacement reactions for both the $[CO_2(CH_2)_3AO]^{2-}$ and $[AO(CH_2)_3AO]^{2-}$ ligands (Table 6-2). One can again see that the bifunctional ligand has more favorable thermodynamics than the $[AO(CH_2)_3AO]^{2-}$ ligand in displacing Ca^{2+} and CO_3^{2-} ions to bind with UO_2^{2+}.

Table 6-1 Gibbs free energies for sequential binding of the $[CO_2(CH_2)_3AO]^{2-}$ ligand (AcAO) with uranyl (UO_2^{2+}), in comparison with the $[AO(CH_2)_3AO]^{2-}$ ligand.

Binding free-energy	$[CO_2(CH_2)_3AO]^{2-}$ ligand[a]	$[AO(CH_2)_3AO]^{2-}$ ligand[b]
First ligand: ΔG_1 (kJ/mol)	-117	-92
Second ligand: ΔG_2 (kJ/mol)	-87	-55
Total: ΔG (kJ/mol)	-202	-147

[a]This work, namely, the AcAO ligand; [b]Ref. 94. AO is the amidoximate group, that is, $-C(NH_2)=N-O^-$.

Table 6-2 Gibbs free energies for displacement of Ca^{2+} and CO_3^{2-} ions in $Ca_2[UO_2(CO_3)_3]$ by the $[CO_2(CH_2)_3AO]^{2-}$ ligand and the $[AO(CH_2)_3AO]^{2-}$ ligand.

Reaction	ΔG (kJ/mol)
$Ca_2[UO_2(CO_3)_3] + 2[CO_2(CH_2)_3AO]^{2-} = [UO_2(CO_2(CH_2)_3AO)_2]^{2-} + 3CO_3^{2-} + 2Ca^{2+}$	-47
$Ca_2[UO_2(CO_3)_3] + 2[AO(CH_2)_3AO]^{2-} = [UO_2(AO(CH_2)_3AO)_2]^{2-} + 3CO_3^{2-} + 2Ca^{2+}$	8

6.3.7 Implications

The comparison between the $[CO_2(CH_2)_3AO]^{2-}$ ligand (AcAO) and the $[AO(CH_2)_3AO]^{2-}$ ligand in Table 1 suggests a synergy between the carboxylate group and the amidoximate group in binding with uranyl. This is consistent with the experimental findings that the highest uptake of uranium is achieved via copolymerization of acrylonitrile (which further reacts with NH_2OH to yield amidoxime groups) and an unsaturated carboxylic acid (such as itaconic acid), followed by conditioning with a base (such as KOH).[77,95] Of course, our model is a simple one, but it serves as an important initial step toward understanding the binding modes of uranyl in the real polymeric sorbents for seawater uranium recovery.

Another point is that we have used the deprotonated forms of amidoxime and carboxylic groups to bind with uranyl. In the seawater pH (~8.0), uranyl exists mainly as the neutral $Ca_2[UO_2(CO_3)_3]$ species in seawater,[9,15,16] while the ligands themselves could exist in either neutral un-deprotonated or ionic deprotonated state, depending on their pK_a. Speciation studies have shown that after binding with uranyl at pH~8, the amidoxime ligands usually exist in the deprotonated form in the complex.[3,5] This is the reason why we started with the deprotonated form in our classical molecular dynamics (CMD) simulation of the binding process, since CMD cannot simulate the bond-breaking deprotonation process. For ligands with pK_a much greater than 8 (e.g., 11 or above), they usually exist as the neutral, un-deprotonated state at pH~8 and then lose the proton when binding with uranyl; the proton usually reacts with the displaced carbonate to form bicarbonate.[13,23] Such reaction processes can be studied with either quantum mechanical calculations with an implicit solvation model[13] or hybrid quantum mechanical/molecular mechanical (QM/MM) MD simulations with an explicit solvation.[23]

6.4 Conclusions

We have simulated the binding of an amidoxime-carboxylate bifunctional ligand ($[CO_2(CH_2)_3AO]^{2-}$ or AcAO) with uranyl. DFT-PBE calculations of the gas-phase structures yielded a chelate binding mode to uranyl: amidoximate binding with η^2 via the oximate group and a monodentate carboxylate binding via an oxygen atom. DFT-PBE-based ab initio molecular dynamics (MD) simulation of the UO_2AcAO complex in an explicit water environment confirmed the stability of the chelate mode. Classical MD and free-energy simulations in a simulated seawater environment (namely, 0.5 M NaCl) showed that one of the carboxylate oxygens binds first to uranyl, leading to a loose intermediate state with a broad minimum, and then the amidoximate group overcomes a free-energy barrier and displaces a water molecule coordinated to U, resulting in a much more stable and tightly bound chelate state. Binding of the second AcAO ligand follows a similar process and the two AcAO ligands prefer a trans-configuration at the equatorial coordination plane of uranyl. We further obtained the binding free energies from the potential-of-mean-force curves and found that the binding of the two AcAO ligands bind with uranyl is 55 kJ/mol stronger than the two $[AO(CH_2)_3AO]^{2-}$ ligands, indicating a synergy between amidoximate and carboxylate groups in binding uranyl.

7 Displacement of Carbonates in $Ca_2UO_2(CO_3)_3$ by Amidoxime-based Ligands from Free-energy Simulations

7.1 Introduction

To understand how polymeric sorbents grafted with AO ligands extract uranyl from seawater, it is necessary to investigate the competition between carbonates and amidoxime ligands with the explicit consideration of common ions and water molecules.[36,96]

Free-energy simulations including many ions and solvent molecules are beyond the capability of ab initio or first principles MD. Instead, in this work we employ classical MD methods with umbrella sampling to obtain the free-energy profile for the ligand displacement between carbonates of $Ca_2UO_2(CO_3)_3$ with amidoxime-based ligands. This approach has been successfully employed recently[93,97] to obtain free-energy profiles and thermodynamics of uranyl binding with carbonate and Ca^{2+} as well as with glutardiamidoxime in NaCl solutions, offering accurate binding free energies in comparison with the experiment. Herein we apply this approach to the ligand-displacement processes, that is, the reaction between amidoxime-based ligands and $Ca_2UO_2(CO_3)_3$, in an effort to reveal key mechanistic detail and to quantify the thermodynamic driving force that will be useful to understand seawater uranium extraction by amidoxime-grafted polymeric sorbents.

7.2 Computational Methods

7.2.1 Simulation systems and force field parameters

The simulation system contains one $Ca_2UO_2(CO_3)_3$ complex, a number of amidoxime-based ligands, and 2,000 water molecules in a cubic box with periodic boundary conditions applied. To simulate the seawater condition, we added Na^+ and Cl^- ions to reach a NaCl concentration of 0.5 M. The whole periodic simulation box was kept neutral by adding ions (Na^+ or Cl^-) to balance the charge. No explicit H^+ or OH^- ions were in the simulation box, so the system pH could be considered at 7, which is a reasonable approximation to the seawater pH (~8.2), since pH control is still very challenging for classical MD simulations. The original TIP3P model[41] was employed for the water molecules. The force-field parameters of UO_2^{2+} were chosen from Guilbaud and Wipff's model[40] and those for CO_3^{2-} were parameterized following the recent work of Doudou et al.[36] The Na^+ and Cl^- ions were modeled with the parameterization of Joung and Cheatham[45] and the parameters for Ca^{2+} were chosen from the work of Rahaman et al.[62] and successfully applied in a recent study.[36] The force-field parameters for amidoxime ligands were generated from the AMBER GAFF force field[42] except for the atomic charges, which were derived from fitting the restrained electrostatic potential (RESP) at the B3LYP/6-31+G* level with the Gaussian09 package[84] and using the antechamber program suite.[85] The Lorentz-Berthelot rules were used to obtain the cross pairs of atoms.

7.2.2 Classical molecular dynamics simulations

Classical MD simulations were carried out for each prepared system by employing the Amber 14 molecular simulation package.[51] First, 4,000 cycles of minimization (2,000 cycles of steepest descent and 2,000 cycles of conjugate gradient) were carried out to relax the solvent, while all the solute atoms were constrained by a potential of 3,000 kcal/(mol/Å). Second, another minimization stage was conducted with the solute atoms constrained by 500 kcal/(mol/Å). Third, 4000 cycles of energy minimization (2,000 cycles of steepest descent and 2,000 cycles of conjugate gradient) were carried out without any constraint. Next, the system was gradually heated

from 0 to 300 K over a period of 50 ps, followed by another 100 ps of *NPT* MD simulations to relax the system to its equilibrium density, which is close to 1.0 g/cm^3, with the target temperature of 300 K and the target pressure of 1.0 atm. Afterward, additional 10 ns of *NPT* MD simulation with a target temperature of 300 K was performed as pre-equilibration before umbrella sampling. All the simulations were accomplished by applying the GPU-accelerated *pmemd* program[51] in Amber 14. A time step of 1.0 fs was used for all the simulations. The SHAKE algorithm[50] was applied to constrain all hydrogen-containing bonds with a tolerance of 10^{-5}. The Berendsen thermostat method[63] was used to control the system temperature and a cutoff of 12 Å was set for both van der Waals (vdW) and the real-space part of electrostatic interactions. A continuum model correction implemented in Amber 14 for energy and pressure was used for the long range vdW correction. Long range electrostatics were calculated using Particle mesh Ewald (PME)[64] with the Ewald coefficient of 0.22664 Å^{-1} for the reciprocal part and a cubic spline switch function for the direct sum.

7.2.3 Umbrella sampling

The umbrella sampling technique[65,66] was employed to map out the free-energy profiles of the displacement of CO_3^{2-} and Ca^{2+} with amidoxime ligands. The distance difference, $d_{U\text{-}C} - d_{U\text{-}O}$, was chosen as the reaction coordinate (RC) for the exchange of the anionic amidoxime ligand with CO_3^{2-}. Here $d_{U\text{-}C}$ is the distance between U and C of carbonate while $d_{U\text{-}O}$ is the distance between U and O of amidoxime. For the introduction of an additional Ca^{2+} ion, U-Ca distance $d_{U\text{-}Ca}$ was chosen as the RC. For each displacement process, CMD simulations were performed with a series of biasing harmonic potential (50 kcal mol^{-1} Å^{-2}) along the RC with 0.1~0.2 Å step separating the neighboring simulation windows. 2 ns MD simulation was carried out for each window with the second half being sampled for production. Then the simulation data for all windows of each system were collected to determine the probability distributions along the RC and further pieced together by the weighted histogram analysis method (WHAM)[67,68] to generate the free-energy profile.

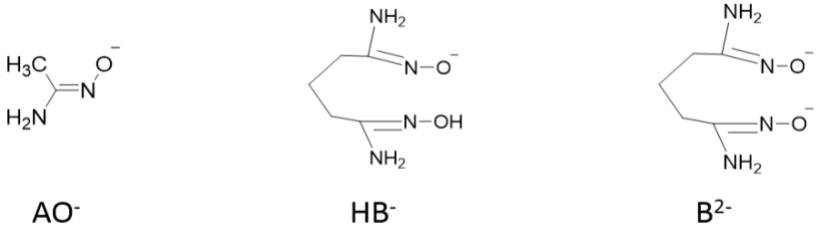

Scheme 7-1 The three amidoximate ligands simulated in this study to displace CO_3^{2-} in $Ca_2UO_2(CO_3)_3$: acetamidoximate (AO^-); monodeprotonated glutardiamidoxime (HB^-); double deprotonated glutardiamidoxime (B^{2-}).

7.3 Results and discussion

The three commonly used small-molecule amidoxime ligands are acetamidoxime (HAO), the open-chain glutardiamidoxime (H_2B), and the cyclic glutarimidedioxime (H_2A). Experimental studies[5,98] of their binding with uranyl show that at the seawater pH the anionic forms are the main binding form (Scheme 7-1) and the dominant species are $UO_2(AO)_3^-$ in the case of HAO and $UO_2B(HB)^-/UO_2B_2^{2-}$ in the case of H_2B. Here we chose HAO and the open-chain H_2B instead of the cyclic H_2A to study here for two reasons. First, the cyclic form binds vanadium (V) too strong, leading to poorer U/V selectivity than the open-chain form.[81] Second, the complex structure

between the uranyl and the cyclic form has been solved and the binding mode is relatively simple;[19] in contrast, both the binding mode and the complex structure between uranyl and the open-chain form are still unclear.

The total displacement reactions of the three carbonate groups in $Ca_2UO_2(CO_3)_3$ by the anionic forms of the ligands (Scheme 7-1) are proposed as in Scheme 7-2: (a) by three AO^- to produce $UO_2(AO)_3^-$; (b) by one B^{2-} and one HB^- to produce $UO_2B(HB)^-$; (c) by two B^{2-} to produce $UO_2B_2^{2-}$. Below we examine the three reactions one by one.

(a) $Ca_2UO_2(CO_3)_3 + 3AO^- \rightarrow UO_2(AO)_3^- + 2Ca^{2+} + 3CO_3^{2-}$

(b) $Ca_2UO_2(CO_3)_3 + HB^- + B^{2-} \rightarrow UO_2B(HB)^- + 2Ca^{2+} + 3CO_3^{2-}$

(c) $Ca_2UO_2(CO_3)_3 + 2B^{2-} \rightarrow UO_2B_2^{2-} + 2Ca^{2+} + 3CO_3^{2-}$

Scheme 7-2 The proposed displacement reactions of the three carbonates in $Ca_2UO_2(CO_3)_3$ by (a) three AO^-; (b) one HB^- and one B^{2-}; (c) two B^{2-}.

7.3.1 Displacement of three carbonates by acetamidoximate

Figure 7-1 shows the compete free-energy profile for the displacement of three carbonates by acetamidoximate. We found that the first two carbonates are different from the third one in terms of the displacement mechanism and the free-energy profiles. This is closely related to the two Ca^{2+} ions already in $Ca_2UO_2(CO_3)_3$. So we examine the first two carbonates and the third one separately.

7.3.1.1 Displacement of the first two carbonate groups by acetamidoximate

In the first stage of the displacement reaction as shown in Figure 7-1, we found that one incoming AO^- replaces one $CaCO_3$ unit or ion pair. This process can be divided into two steps:

$$Ca_2UO_2(CO_3)_3 + AO^- \rightarrow Ca_2UO_2(CO_3)_2(AO)^+ + CO_3^{2-} \quad (7.1)$$

$$Ca_2UO_2(CO_3)_2(AO)^+ \rightarrow CaUO_2(CO_3)_2(AO)^- + Ca^{2+} \quad (7.2)$$

Eq. (7.1) and Eq. (7.2) correspond to the steps of **A1→A2→A3** and **A3→A4→A5** in Figure 7-1, respectively. The relevant structures are depicted in Figure 7-2. One can see that in the initial state **A1**, the AO^- ligand approaches the $Ca_2UO_2(CO_3)_3$ complex from the back position between two carbonates facing away from the two Ca^{2+} ions. Then the oximate O of AO^- binds to U, while the carbonate on the opposite side (the leaving group) between the two Ca^{2+} ions changes to a monodentate mode (**A2**). Then the carbonate group leaves (**A2→A3**), which requires a free-energy barrier of about 6 kcal/mol. Overall, Eq. (7.1) is endergonic by 5.3 kcal/mol with a barrier about 10.2 kcal/mol, easily surmountable at room temperature. Then, the dissociated CO_3^{2-} grabs one Ca^{2+} away from the uranyl complex but still interacts with the remaining Ca^{2+} (**A4**). The AO^- in $CaUO_2(CO_3)_2(AO)^-$ (**A4**) is in a distorted η^2 binding mode where the distance from the oximate N to U is slightly longer than in a usual η^2 binding mode. This distorted η^2 binding mode has been found to be common in our classical MD simulations of the uranyl-amidoximate complexes,[35] likely due to the explicit solvation by the water hydrogen-bond network about the complex. Next, the $Ca^{2+}\ldots CO_3^{2-}$ ion pair completely dissociates away (**A4→A5**). Combining Eq. (7.1) and Eq. (7.2), the displacement of the first CO_3^{2-} by AO^- is only slightly endergonic by about 2.8 kcal/mol due to the stabilization of the leaving CO_3^{2-} by Ca^{2+}.

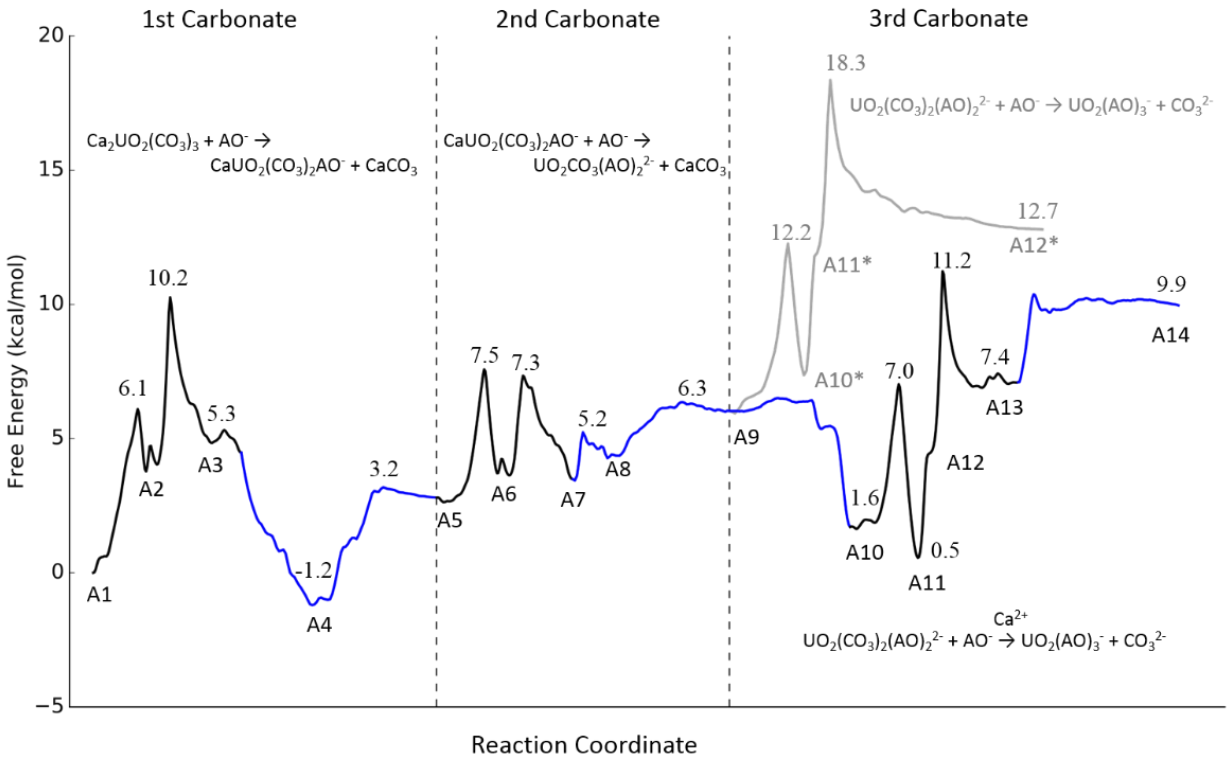

Figure 7-1 Free-energy profile for displacing the first, second and third carbonates in the $Ca_2UO_2(CO_3)_3$ complex by acetamidoximate (AO^-). For black and grey lines, reaction coordinate is $d_{U\text{-}C} - d_{U\text{-}O}$; for blue lines, reaction coordinate is $d_{U\text{-}Ca}$.

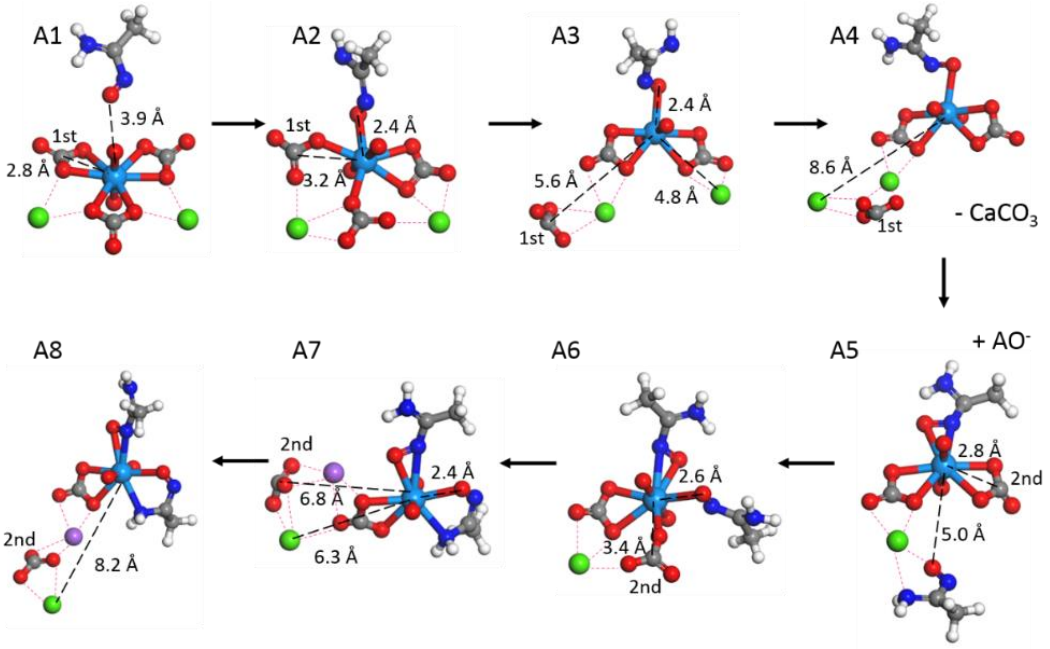

Figure 7-2 Structure snapshots for displacing the first two carbonates in the $Ca_2UO_2(CO_3)_3$ complex by acetamidoximate (AO^-). The structure labels correspond to the intermediate states in Figure **7-1**. Color code: U, light blue; O, red; C, gray; N, dark blue; Ca, green; Na, purple; H, white.

The displacement of the second CO_3^{2-} by AO^- can be similarly divided into two reactions:

$$CaUO_2(CO_3)_2(AO)^- + AO^- \rightarrow CaUO_2(CO_3)(AO)_2 + CO_3^{2-} \quad (7.3)$$

$$CaUO_2(CO_3)(AO)_2 \rightarrow UO_2(CO_3)(AO)_2^{2-} + Ca^{2+} \quad (7.4)$$

Eq. (7.3) and Eq. (7.4) correspond to the steps of **A5→A6→A7** and **A7→A8→A9**, respectively, in Figure 7-1. The relevant structures are also shown in Figure 7-2. The second attacking AO^- forms the U-O binding while the second leaving CO_3^{2-} switches from bidentate to monodentate binding with uranyl (**A6**). Then the attacking AO^- forms a bidentate binding mode with U and the CO_3^{2-} group breaks away from U, whereas a Na^+ ion bridges the leaving CO_3^{2-} and the remaining one (**A7**). Note that in the displacement of the first CO_3^{2-} it is the remaining Ca^{2+} ion that bridges the leaving and binding carbonates (**A4**, Figure 7-2). Next, the leaving CO_3^{2-} drags the remaining Ca^{2+} ion along and dissociates as an ion pair (**A7→A8**). In $UO_2(CO_3)(AO)_2^{2-}$ (**A8),** the chelate binding mode between the second attacking AO^- with U was found. Although previous DFT calculations with an implicit solvation model suggested that the η^2 mode is preferred,[24,25] recent EXAFS investigation of uranyl binding in amidoxime-functionalized polymer fibers together with high-level quantum chemistry calculations showed that the chelate mode is also energetically competitive.[17] In our case, we think that the nearby carbonate group and the Na^+ ion have perturbed the hydrogen bond network, leading to the chelate bond.

Overall we find that the free energy barrier of the second CO_3^{2-} displacement (~ 4 kcal/mol) is lower than that of the first one (~ 10 kcal/mol). In other words, the second CO_3^{2-} displacement is kinetically easier than the first one. This can be attributed to the destabilization of the complex after dissociating away the first CO_3^{2-} and Ca^{2+} ions. Thermodynamically, the free energy increases further by about 3.2 kcal/mol after the second displacement, similar to the amount after the first one. So the reaction is endergonic by about 6.0 kcal/mol for the first two carbonate displacements.

7.3.1.2 Displacement of the third carbonate group by acetamidoximate

We first investigated the direct exchange of the third carbonate by the third AO^-

$$UO_2(CO_3)(AO)_2^{2-} + AO^- \rightarrow UO_2(AO)_3^- + CO_3^{2-} \quad (7.5)$$

Eq. (7.5) corresponds to the steps of **A9→A10*→A11*→A12*** in Figure 7-1. The corresponding intermediate structures are shown in Figure 7-3. Overall, the process is both kinetically and thermodynamically more difficult than the first two displacements: uphill by 6 kcal/mol with a free-energy barrier of 12 kcal/mol. With the insertion of the third AO^- ligand, the binding state of the second AO^- changes from a bidentate model to the η^2 mode (**A10*** in Figure 7-3). Then the binding state of the leaving CO_3^{2-} changes from bidentate to monodentate binding (**A10*→A11*** in Figure 7-3) and next it dissociates away; this step of CO_3^{2-} dissociation is most responsible for the higher barrier and free-energy increase, as shown in Figure 7-1.

Since Ca^{2+} ions facilitate the displacement of the first two carbonate groups, we hypothesize that an additional Ca^{2+} ion can help the third carbonate displacement. As shown in Figure 7-1, both the free-energy barrier and the free-energy increase are relatively small in the case of the displacement of the second CO_3^{2-} by AO^-. In other words, the displacement of the second CO_3^{2-} by AO^- is a relatively facile process and the help from a Na^+ ion is enough; an additional Ca^{2+} ion may further lower the free-energy barrier, but probably not much. In contrast, the displacement of the third CO_3^{2-} by AO^- is significantly more uphill in free energy; therefore, an additional Ca^{2+} ion is needed. To test this idea, we considered the following reaction steps:

$$UO_2(CO_3)(AO)_2^{2-} + Ca^{2+} \rightarrow CaUO_2(AO)_2 \quad (7.6)$$

$$CaUO_2(CO_3)(AO)_2 + AO^- \rightarrow CaUO_2(AO)_3^+ + CO_3^{2-} \quad (7.7)$$

$$CaUO_2(AO)_3^+ \rightarrow UO_2(AO)_3^- + Ca^{2+} \quad (7.8)$$

Eq. (7.6) involves the binding of a free Ca^{2+} ion with $UO_2(CO_3)(AO)_2^{2-}$ to form the $CaUO_2(CO_3)(AO)_2$ complex and is marked as **A9→A10** in Figure 7-1 and Figure 7-3. This reaction is exergonic by about 4.5 kcal/mol. Then the third AO^- displaces the carbonate in $CaUO_2(CO_3)(AO)_2$ (Eq. (7.7)) and drags the Ca^{2+} ion along (Eq. (7.8)). The binding between the third AO^- with uranyl is formed by overcoming a barrier of 5.4 kcal/mol (**A10→A11**) and slightly exergonic. Then, the CO_3^{2-} group changes from bidentate to monodentate binding (**A11→A12**) and dissociates from uranyl yet maintains close contact with Ca^{2+} (**A12→A13**). The energy barrier of the **A11→A12→A13** step is about 10.7 kcal/mol and the free energy increases by about 6.9 kcal/mol. Next, the $Ca^{2+}\ldots CO_3^{2-}$ ion pair breaks away from the $UO_2(AO)_3^-$ complex (**A13→A14**) with a free energy rise of 2.9 kcal/mol. In $UO_2(AO)_3^-$ (**A14** in Figure 7-3), all three AO^- are in the η^2 binding mode, in agreement with the previous DFT studies with implicit solvation.[10,13]

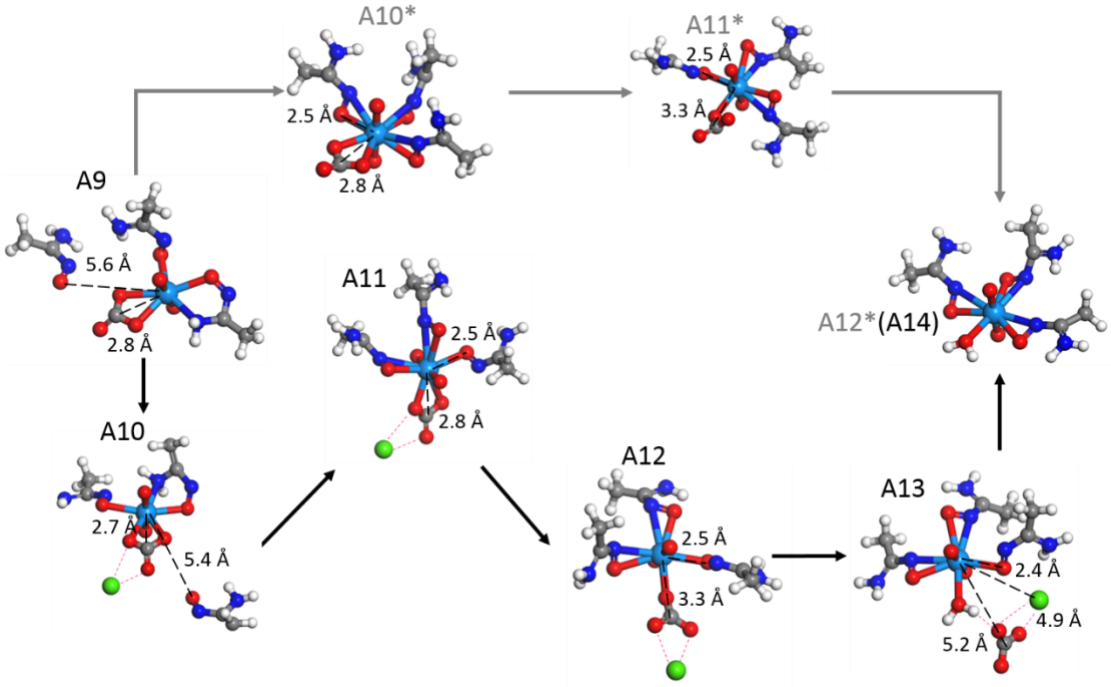

Figure 7-3 Structure snapshots for displacing the third carbonate in the $Ca_2UO_2(CO_3)_3$ complex by the third acetamidoximate (AO^-): without the help of a Ca^{2+} ion, **A9→A10*→A11*→A12***; with the help of a Ca^{2+} ion, **A9→A10→A11→A12→A13→A14**. The structure labels correspond to the intermediate states in Figure **7-1**. Color code: U, light blue; O, red; C, gray; N, dark blue; Ca, green; Na, purple; H, white.

By comparing the difference without and with the presence of the additional Ca^{2+} ion to displace the third CO_3^{2-}, one can see from Fig. 1 that the overall energy barrier for the complete displacement process of the three carbonate groups reduces from 18.3 kcal/mol without the additional Ca^{2+} ion to 11.2 kcal/mol with its presence, while the overall free energy rise drops from 12.7 kcal/mol to 9.9 kcal/mol. Given the overwhelming presence of Ca^{2+} ions in seawater, we think that the pathway with the presence of the additional Ca^{2+} ion should better represent the reality.

7.3.2 *Displacement of the three carbonates by deprotonated glutardiamidoxime*

Experiment suggests[5] that the complexation of uranyl with glutardiamidoxime (H_2B) at the seawater pH exists mainly as $UO_2B(HB)^-$, followed by $UO_2B_2^{2-}$. Our MD simulations[97] found that both species contain at least one chelate binding B^{2-} with UO_2^{2+}. This implies that the first two CO_3^{2-} groups will be displaced by a single B^{2-} which has two end amidoximate groups (Scheme 7-1). The third carbonate can be displaced by either the second B^{2-} or the HB^- ligand.

7.3.2.1 *Displacement of the first two CO_3^{2-} groups by B^{2-}*

Figure 7-4 shows that the free-energy profile of the displacement of the first two CO_3^{2-} groups in the $Ca_2UO_2(CO_3)_3$ complex by a single B^{2-} ligand. The first carbonate displacement has a free-energy barrier of 10.7 kcal/mol and is uphill by 7.2 kcal/mole, while the second carbonate displacement has a free-energy barrier of 6.1 kcal/mol and is downhill by 6 kcal/mol. Again the two CO_3^{2-} groups leave as the $Ca^{2+}\ldots CO_3^{2-}$ ion pairs as facilitated by the two Ca^{2+} ions.

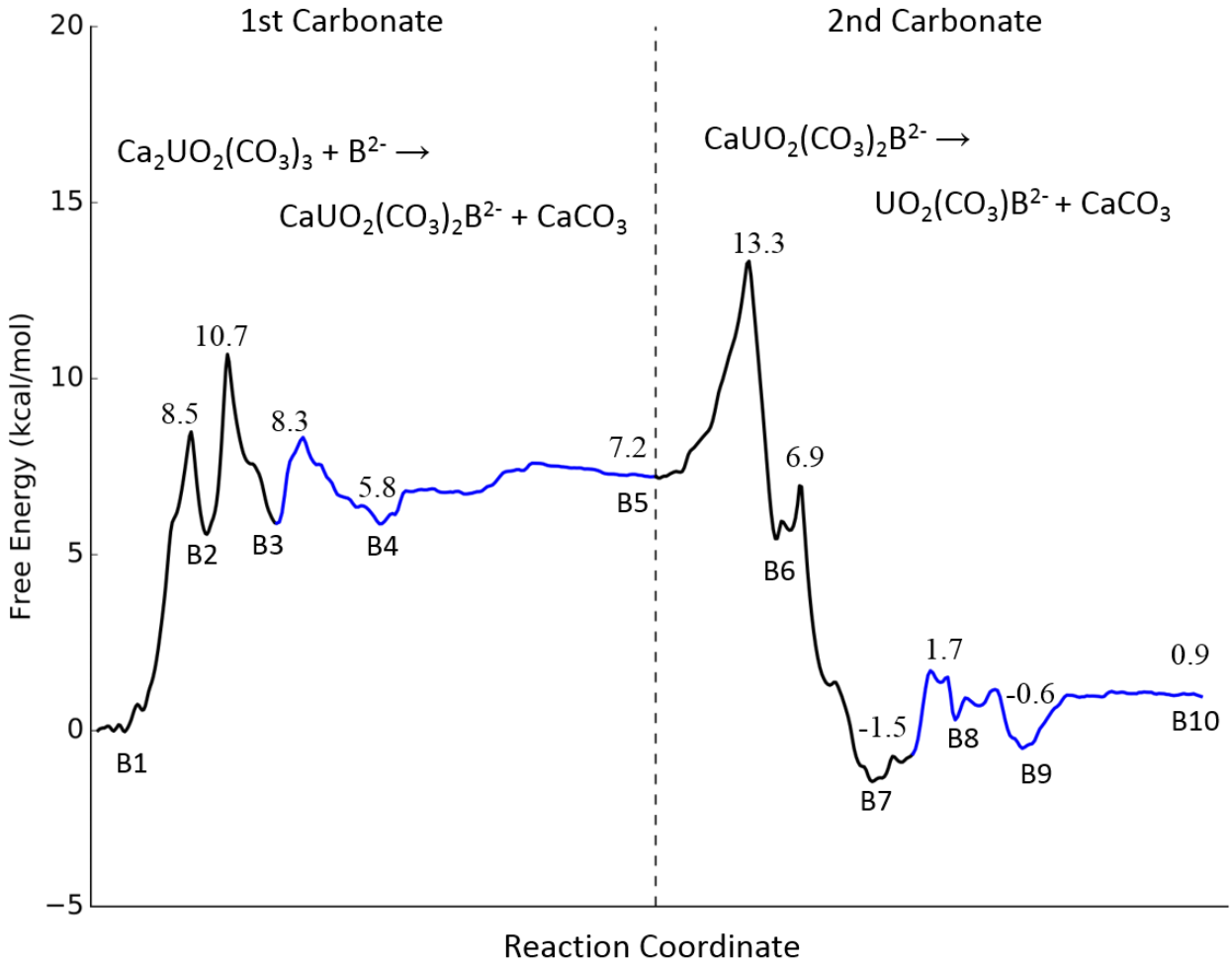

Figure 7-4 Free-energy profile for displacing the first two carbonates in the $Ca_2UO_2(CO_3)_3$ complex by the double deprotonated glutardiamidoxime ligand (B^{2-}). For black lines, reaction coordinate is $d_{U\text{-}C} - d_{U\text{-}O}$; for blue lines, reaction coordinate is $d_{U\text{-}Ca}$.

The intermediate structures in Figure 7-4 are shown in Figure 7-5. One can see how first one end of the B^{2-} ligand binds to U (**B1→B2**), next the first carbonate breaks away (**B2→B3**) and drags a Ca^{2+} ion along (**B4**), and then the Ca^{2+}…CO_3^{2-} pair leaves the complex (**B4→B5**). Subsequently, the loose amidoximate end of the B^{2-} ligand attacks the U center and the second carbonate group leaves with the second Ca^{2+} ion, while the intermediates are also stabilized by a Na^{+} ion (**B8** and **B9**). Due to the chelate effect, the overall process of one B^{2-} ligand displacing the first two carbonate groups is thermodynamically neutral.

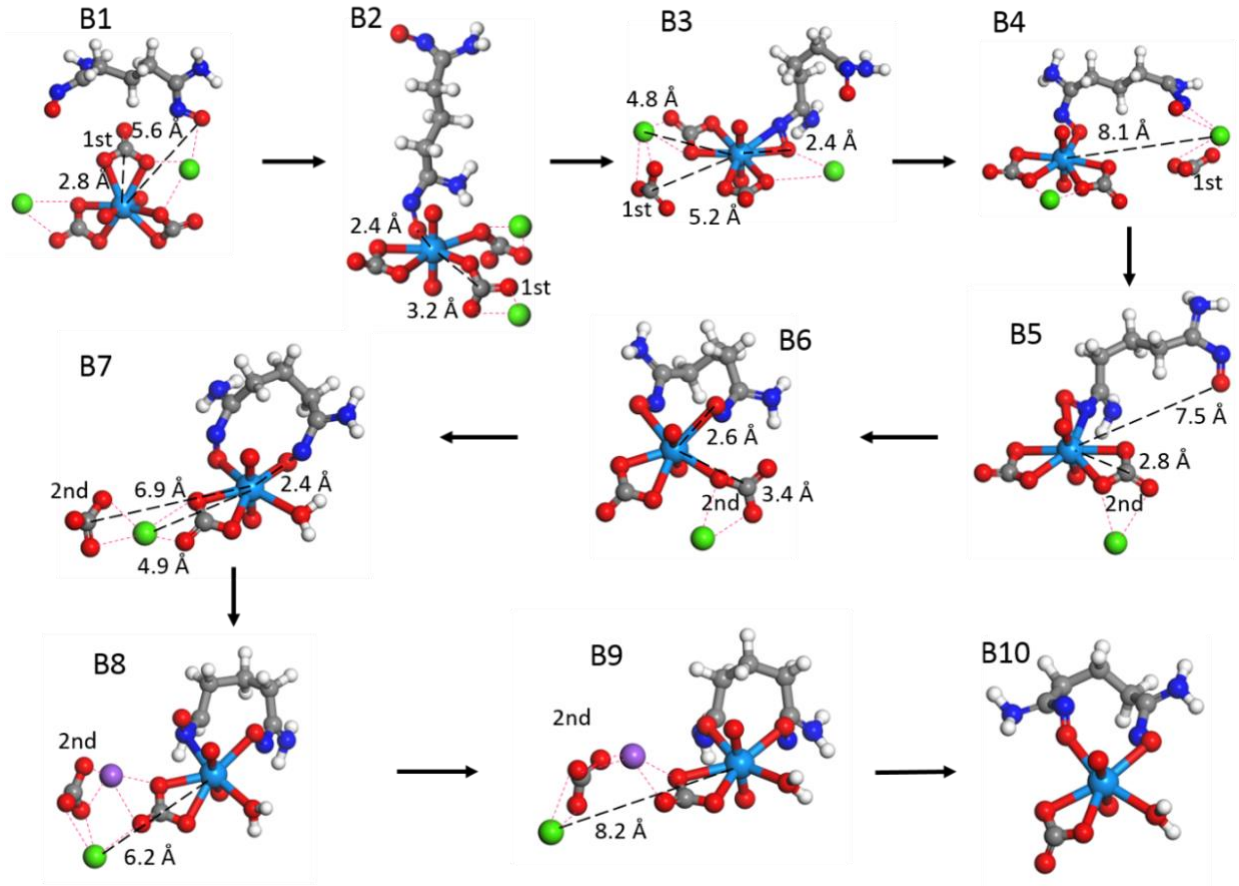

Figure 7-5 Structure snapshots for displacing the first two carbonates in the $Ca_2UO_2(CO_3)_3$ complex by the double deprotonated glutardiamidoxime ligand (B^{2-}). The structure labels correspond to the intermediate states in Figure **7-4**. Color code: U, light blue; O, red; C, gray; N, dark blue; Ca, green; Na, purple; H, white.

7.3.2.2 Displacement of the third CO_3^{2-} group by HB^{-}

With the first and second CO_3^{2-} groups being displaced by the single B^{2-} ligand, we then consider the displacement of the third CO_3^{2-} by HB^{-} which yields $UO_2B(HB)^{-}$, the most dominant species at seawater pH from binding of uranyl with H_2B.[5] Figure 7-6 shows the free energy profile of the displacement process with and without the help of an additional Ca^{2+} ion. Without the Ca^{2+} ion, the reaction has a free-energy barrier of 14.6 kcal/mol and is uphill by 10.4 kcal/mol. With the help of an additional Ca^{2+} ion, the barrier is lowered by 3 kcal/mol and the free energy of the final state is lowered by 4 kcal/mol.

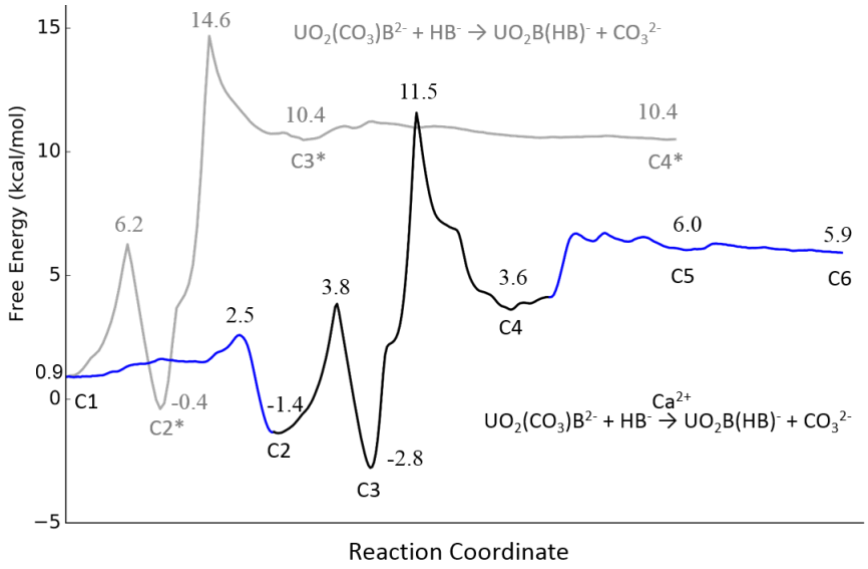

Figure 7-6 Free-energy profile for displacing the carbonate group in the $UO_2(CO_3)B^{2-}$ complex by mono-deprotonated glutardiamidoxime ligand (HB^-). For black lines, reaction coordinate is $d_{U\text{-}C} - d_{U\text{-}O}$; for blue lines, reaction coordinate is $d_{U\text{-}Ca}$.

The intermediates in Figure 7-6 are illustrated in Figure 7-7. The reaction starts with the amidoximate (that is, deprotonated) end of the HB^- ligand attacking U (**C1**). Without the Ca^{2+} ion, the departure of the third carbonate (**C1→C2*→C3*→C4***) is mediated by a Na^+ ion (**C3*** in Figure 7-7). With the Ca^{2+} ion, the initial dissociation of the third carbonate is facilitated by the Ca^{2+} ion (**C1→C2→C3→C4**), while the leaving of the $Ca^{2+}\ldots CO_3^{2-}$ ion pair is also helped by a Na^+ ion (**C5**). In both scenarios, breaking the uranyl-carbonate bonding is the most difficult step.

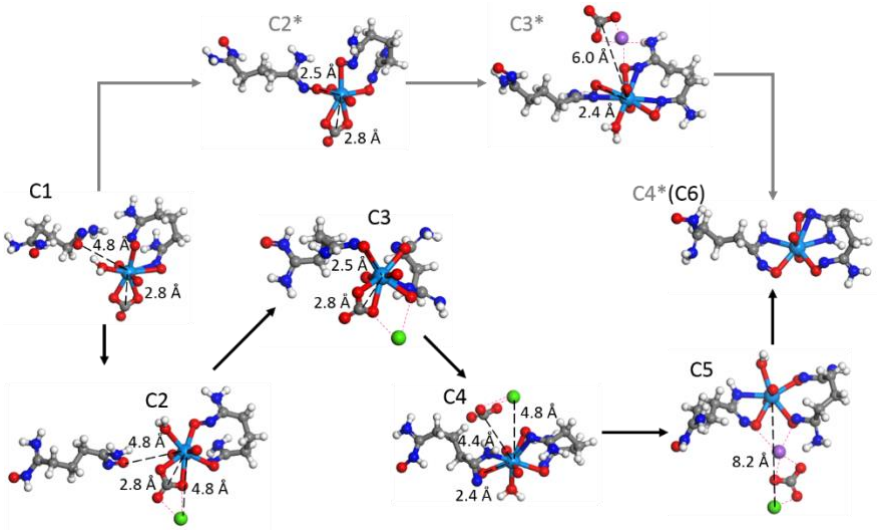

Figure 7-7 Structure snapshots for displacing the carbonate group in the $UO_2(CO_3)B^{2-}$ complex by mono-deprotonated glutardiamidoxime ligand (HB^-): without the help of a Ca^{2+} ion, **C1→C2*→C3*→C4***; with the help of a Ca^{2+} ion, **C1→C2→C3→C4→C5→C6**. The structure labels correspond to the intermediate states in Figure **7-6**. Color code: U, light blue; O, red; C, gray; N, dark blue; Ca, green; Na, purple; H, white.

7.3.2.3 Displacement of the third CO_3^{2-} group by B^{2-}

The third CO_3^{2-} can also be displaced by a second B^{2-} to produce $UO_2B_2^{2-}$, another dominant species after $UO_2B(HB)^-$. The free-energy profile in Figure 7-8shows that with the help of an additional Ca^{2+} ion, the barrier for displacing the third carbonate is lowered by about 4 kcal/mol and the free-energy change of the reaction is also less uphill by 5 kcal/mol. The intermediate structures in Figure 7-9 again show how the presence of the additional Ca^{2+} ion mediates the departure of the carbonate group, while in the absence of the additional Ca^{2+} ion, a Na^+ ion is involved in the exchange process. Unlike the attack by the HB^- ligand where only the amidoximate end of the ligand is involved, both ends of the second B^{2-} ligand are involved in the displacement process. One can see that one oximate O first binds to U at 2.5 Å (D3 in Figure 7-9), while the other loose end interacts with the Ca^{2+} ion. Then the loose end approaches U and the carbonate group switches to monodentate binding (**D4** in Figure 7-9). In the final state, each of the two second B^{2-} ligands binds to U with two distorted η^2 modes, consistent with our previous simulations of the structure of $UO_2B_2^{2-}$ in seawater.[93]

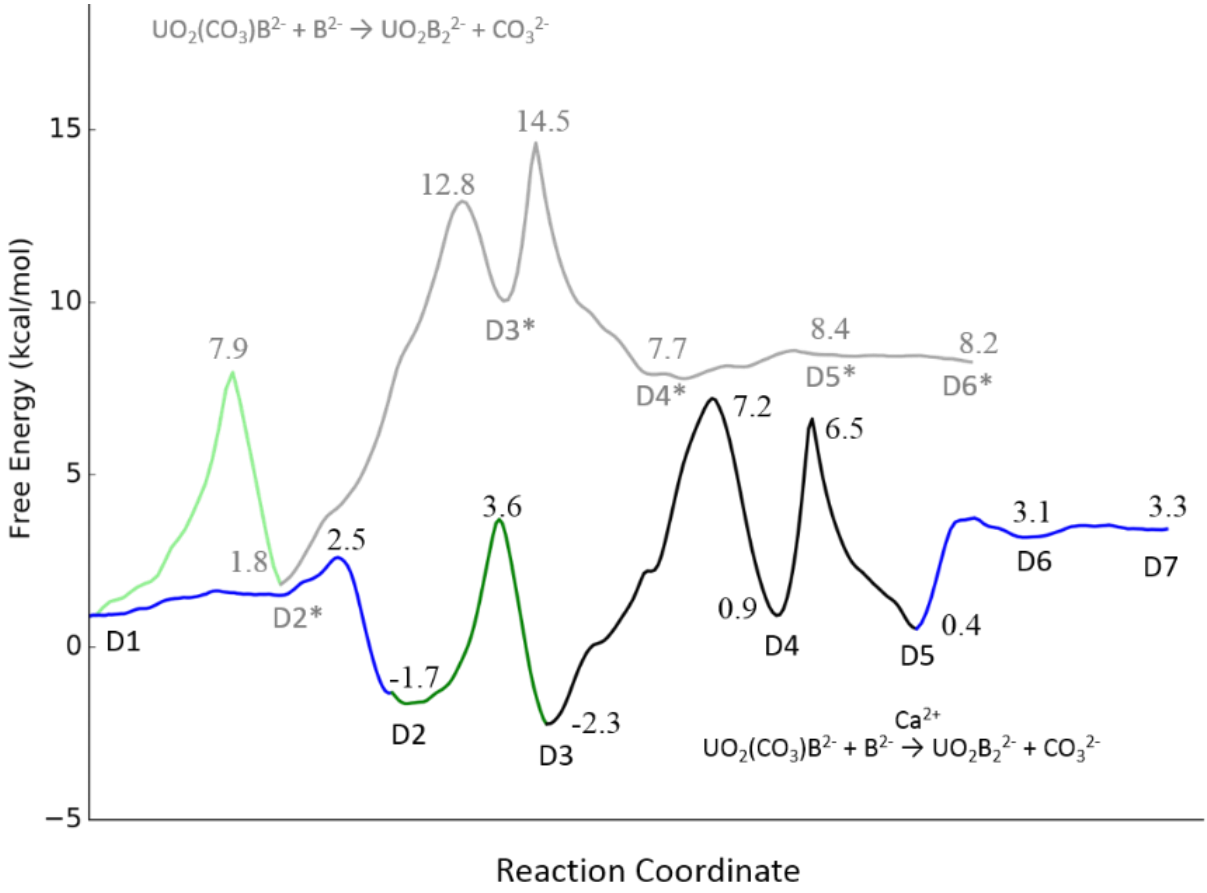

Figure 7-8 Free-energy profile for displacing the carbonate group in the $UO_2(CO_3)B^{2-}$ complex by double deprotonated glutardiamidoxime ligand (B^{2-}). For black and grey lines, reaction coordinate is $d_{U\text{-}C} - d_{U\text{-}O}$; for green and light green lines, reaction coordinate is $d_{U\text{-}C}$; for blue lines, reaction coordinate is $d_{U\text{-}Ca}$.

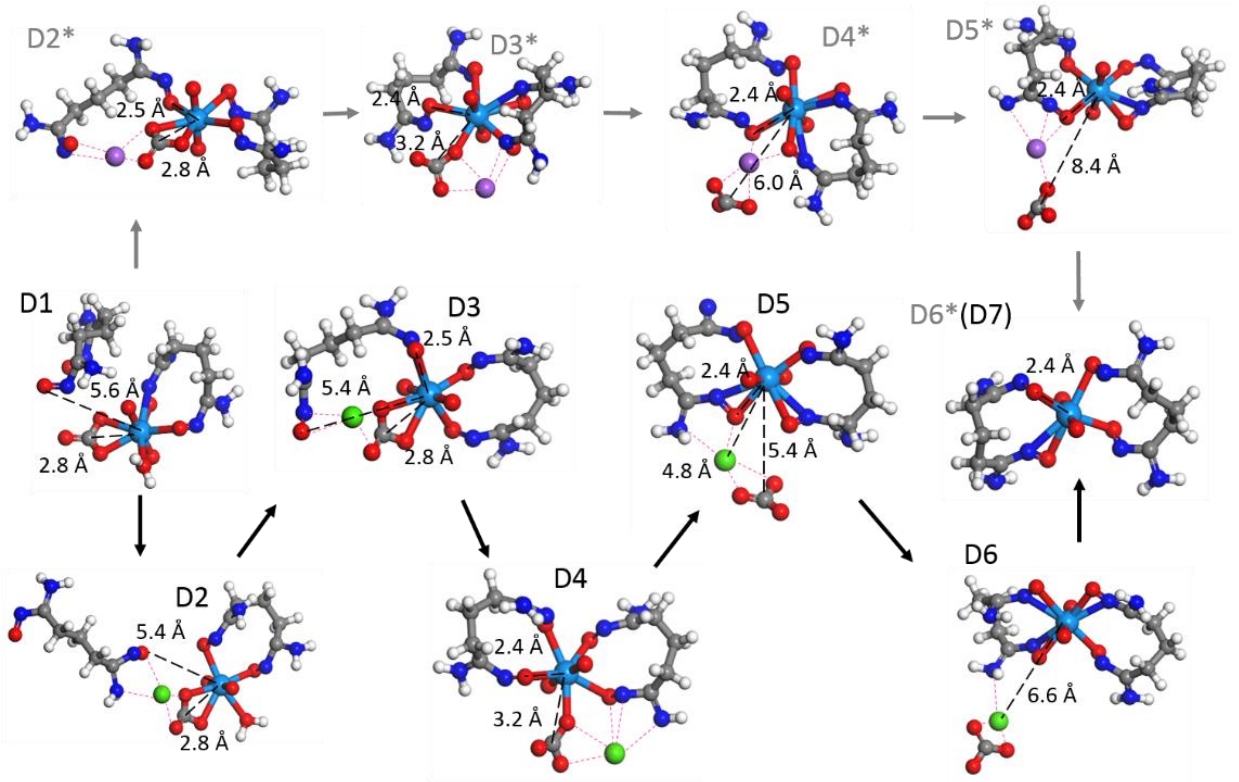

Figure 7-9 Structure snapshots for displacing the carbonate group in the $UO_2(CO_3)B^{2-}$ complex by double deprotonated glutardiamidoxime ligand (B^{2-}): without the help of a Ca^{2+} ion, **D1 → D2* → D3* → D4* → D5* → D6***; with the help of a Ca^{2+} ion, **D1→D2→D3→D4→D5→D6→D7**. The structure labels correspond to the intermediate states in Figure **7-8**. Color code: U, light blue; O, red; C, gray; N, dark blue; Ca, green; Na, purple; H, white.

7.3.3 Overall trends and implications

Now that we have complete pictures of the displacement reactions, we can summarize and compare the overall free-energy changes from several perspectives: displacing two vs. three CO_3^{2-}; AO^- vs. B^{2-}/HB^- ligands; with vs. without the additional Ca^{2+} ion. As shown in Table 7-1, the most favorable thermodynamics is for displacing two CO_3^{2-} in the $Ca_2UO_2(CO_3)_3$ complex by a double deprotonated glutardiamidoxime ligand (B^{2-}), which has ΔG close to zero (0.9 kcal/mol). All the other reactions are uphill in the free energy, ranging from 3 to 13 kcal/mol. Due to the chelate effect, the B^{2-}/HB^- ligands have more favorable ΔG than the simple AO^- by about 2 to 5 kcal/mol. The additional Ca^{2+} ion also lows ΔG by 3 to 5 kcal/mol. We need to emphasize that what we predicted in this study are standard-state free energy change, ΔG°, which relates to the equilibrium constant, K, via $\Delta G° = -RT \ln K$. A positive ΔG° means that *K* is relatively small; e.g., a predicted value of 3.3 kcal/mol for ΔG° corresponds to a *K* value of ~0.004 at room temperature. Even though this *K* value is small, the reaction can still be driven to the right-hand side by using much more excess ligands as practiced experimentally.

Table 7-1 Free-energy changes (ΔG) for displacing CO_3^{2-} in the $Ca_2UO_2(CO_3)_3$ complex by acetamidoximate (AO^-) and deprotonated glutardiamidoxime ligands (B^{2-}/HB^-).

Type	Reaction	ΔG (kcal/mol)
Displacing two CO_3^{2-}	$Ca_2UO_2(CO_3)_3 + 2AO^- \rightarrow UO_2CO_3(AO)_2^{2-} + 2CaCO_3$	6.0
	$Ca_2UO_2(CO_3)_3 + B^{2-} \rightarrow UO_2CO_3B^{2-} + 2CaCO_3$	0.9
Displacing three CO_3^{2-}	$Ca_2UO_2(CO_3)_3 + 3AO^- \rightarrow UO_2(AO)_3^- + 2CaCO_3 + CO_3^{2-}$	12.7
	$Ca_2UO_2(CO_3)_3 + B^{2-} + HB^- \rightarrow UO_2B(HB)^- + 2CaCO_3 + CO_3^{2-}$	10.4
	$Ca_2UO_2(CO_3)_3 + 2B^{2-} \rightarrow UO_2B_2^{2-} + 2CaCO_3 + CO_3^{2-}$	8.2
With additional Ca^{2+}	$Ca_2UO_2(CO_3)_3 + 3AO^- + Ca^{2+} \rightarrow UO_2(AO)_3^- + 3CaCO_3$	9.9
	$Ca_2UO_2(CO_3)_3 + B^{2-} + HB^- + Ca^{2+} \rightarrow UO_2B(HB)^- + 3CaCO_3$	5.9
	$Ca_2UO_2(CO_3)_3 + 2B^{2-} + Ca^{2+} \rightarrow UO_2B_2^{2-} + 3CaCO_3$	3.3

There are several important implications from the present study. First, we see very important roles played by both Ca^{2+} and Na^+ ions during the ligand displacement process and the whole free-energy profile, confirming the necessity to take them into account in the simulations. Second, since the B^{2-}/HB^- ligands better represent the ligands grafted on the polymeric sorbents than the simple AO^-, we expect that the chelate effect is important and a positive entropy change for the displacement reaction. Hence the enthalpy change will be likely to be positive, so higher temperature will shift the equilibrium toward the right favoring uranium extraction. Last, since displacing the third carbonate by the amidoxime-based ligands is difficult, it may be sufficient for U extraction to just displace the first two carbonate groups.

7.3.4 Further discussions

In this work, we used the anionic forms of the amidoxime ligands for replacing the carbonate groups. However, the amidoxime ligands should exist mainly as the neutral form in the seawater pH (8.2) due to their rather weak acidity or large pK_a's (~13). The protons from the amidoxime ligands are supposed to react with the leaving carbonates from the $Ca_2UO_2(CO_3)_3$ complex to form bicarbonate, the dominant species of the total carbonates at the seawater pH. Of course, our classical MD simulations cannot describe this proton-transfer process. We hope that future hybrid quantum mechanical/molecular mechanical (QM/MM) simulations can address this issue.

We found that the carbonate group leaves as the $CaCO_3$ ion pair. To determine how difficult to separate the ion pair, we obtained the free-energy profile for dissociating the pair into two separate ions (Figure 7-10). In water, the ion pair is found to be 9 kcal/mol more stable in free energy than the separate ions; in 0.5 M NaCl, the ion pair is found to be 5 kcal/mol more stable. In addition, a free-energy barrier of about 8 kcal/mol is required for the dissociation of the ion pair into separate ions in both cases. So in our simulation time scale, the ions stay as a pair. In the real seawater, the Ca^{2+} concentration is about 100 times the CO_3^{2-} concentration, so we expect that some CO_3^{2-} ions may exist as the $CaCO_3$ ion pair.

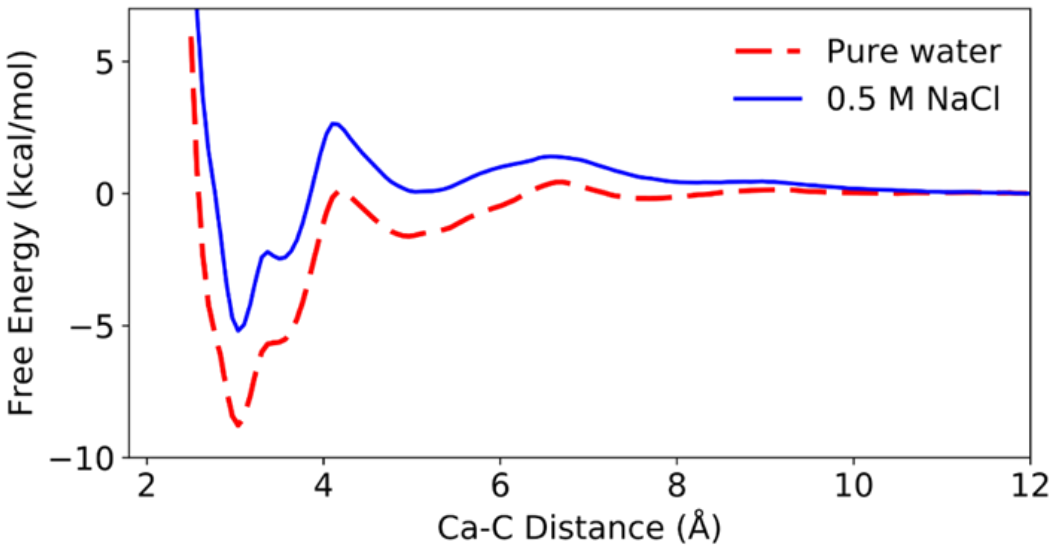

Figure 7-10 Free energy profile for the association of CO_3^{2-} with Ca^{2+}.

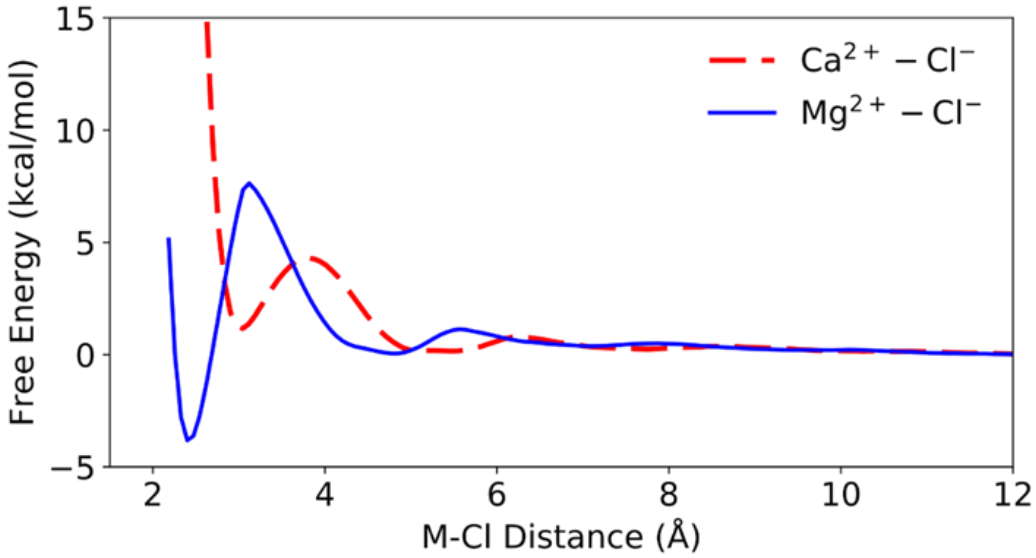

Figure 7-11 Free energy profile for the association of Ca^{2+}(red dashed line) and Mg^{2+}(blue solid line) with Cl^{-}.

A main finding of the present work is that an additional Ca^{2+} ion can facilitate the displacement of the third carbonate group. Since the concentration of Mg^{2+} is about five times that of Ca^{2+}, one wonders if Mg^{2+} can also facilitate displacement of the third carbonate group. To test this idea, we placed a Mg^{2+} ion in our simulated 0.5 M NaCl solution. Interestingly, we found that the Mg^{2+} ion quickly forms an $MgCl^{+}$ ion pair with Cl^{-}. So we compared the free energy profiles for associations of the $CaCl^{+}$ and $MgCl^{+}$ ion pairs (see Figure 7-11). One can see that formation of a contact ion pair is more favorable for $MgCl^{+}$ than $CaCl^{+}$. In other words, Ca^{2+} is more easily found as free ion that Mg^{2+}, and is therefore more suitable for facilitating the displacement reaction.

7.4 Conclusions

We have used classical molecular dynamics combined with umbrella sampling to map the free-energy profiles for the displacement of the three carbonates in $Ca_2UO_2(CO_3)_3$ by the simple acetamidoximate (AO^-) and the more complex glutardiamidoximate (B^{2-}/HB^-) ligands in the 0.5 M NaCl aqueous solution. We found that the two Ca^{2+} ions in $Ca_2UO_2(CO_3)_3$ can greatly facilitate the displacement of the first two carbonate groups which leave as the neutral $Ca^{2+}\ldots CO_3^{2-}$ ion pairs. Displacing the last carbonate needs the help of an additional Ca^{2+} ion. The presence of the Na^+ ions also helps mediate the carbonate departure. The overall displacement reaction is endergonic up to 13 kcal/mol, depending on the number of carbonates to be displaced, the amidoxime ligand type, and the presence of the additional Ca^{2+} ion. These insights will be useful to understand seawater uranium extraction by amidoxime-grafted polymeric sorbents.

8 Solvation of the Vanadate Ion in Seawater Conditions from Molecular Dynamics Simulations

8.1 Introduction

Although promising, the state-of-the-art poly(amidoxime) sorbents attract more vanadium (V) than uranium from sweater [74,99]. Hence, one prevalent challenge of developing advanced sorbents for uranium from seawater is to enhance U/V selectivity while increasing the U uptake at the same time.

Vanadium exists in seawater at 1.7-2.3 ppb [100] with a predominate oxidation state of 5+ as a vanadate anion, [101] while uranium is found at 3.3 ppb as a uranyl ion [102]. The speciation of vanadate (V) in solution can involve complex equilibria between various mono- and oligonuclear clusters, critically depending on concentration and pH [103]. In seawater pH of 8.2, V(V) is present in equilibrium with two oxyanion forms of the orthovanadate, $H_2VO_4^-$ and HVO_4^{2-}. Although a number of recent studies have shed important light on speciation of uranyl in different aqueous environments,[15,16,57,104 9] little is known about speciation of vanadium species in seawater [103,105-108]. Equilibrium complexation of HVO_4^{2-} has been previously determined from speciation calculations using free ion concentrations modeled for seawater and calculated stability contestants at the appropriate ionic strength [107].

From the perspective of molecular simulations, Buhl et al. have investigated water effects on the ^{51}V NMR chemical shifts of $H_2VO_4^-$ with Car-Parrinello molecular dynamics (CPMD) [109]. They found that the aqueous environment induced a conformational change on the two VOH moieties from C_2 symmetry to C_s symmetry and an exchange of water molecules between the first solvation sphere of $H_2VO_4^-$ and the solution. Recent work with coupled cluster theory examined coordination number and prominent binding modes of water and other ligands to vanadyl (VO_2^+) [106]. From a single-crystal structure, Rao and coworkers have found a unique binding mode of vanadium to amidoxime-type ligand, where the V-O bonds are sequentially displaced by two amidoximate oxygens [81]. In addition, the oxovanadium (IV) and dioxovanadium (V) complexation with an amidoximate ligand has been studied computationally [105,106].

To our knowledge, the solvation of the HVO_4^{2-} ion, a major species of V(V) in seawater, has not been studied from a computational perspective, especially under the realistic solvation conditions. In this paper, our goal is to understand solvation of the HVO_4^{2-} ion in seawater from molecular dynamics simulations. We use both density functional theory molecular dynamics (DFT-MD) and classical molecular dynamics (CMD) simulations. Starting with Na_2HVO_4, we first pry into dissociation of sodium ions. Next, we investigate how Na^+ ions interact with the vanadate ion. Furthermore, we calculate the potential of mean force of dissociating Na^+ from vanadate.

8.2 Computational methods

8.2.1 DFT-MD

First-principles molecular dynamic simulations based on density functional theory (DFT-MD) and Born–Oppenheimer approximation were carried out using Vienna Ab-initio simulation package (VASP) with plane wave basis and periodic boundary conditions [26,27]. The Kohn-Sham equations are solved with the all-electron projected augmented wave (PAW) method [28,29]. We have chosen the Perdew-Burke-Ernzerhof (PBE) functional of the generalized-gradient approximation (GGA) for electron exchange and correlation [30]. PBE is one of the most versatile GGA functionals, which provides a balance description for diverse molecules and materials,

instead of being designed for a special class of molecules or interactions. The MD calculations were carried out at 298 K in a canonical NVT ensemble for a periodic cubic box that contains one Na_2HVO_4 complex in a fixed number of water molecules: we examined two concentrations with 50 and 100 water molecules. The temperature was kept constant via Nose-Hoover thermostat. A Verlet algorithm was used to integrate Newton's equation of motion with a time step of 1 femtosecond. After equilibration at 298 K for 15 ps, another 15 ps of production run was followed. Graphical visualization and analysis of the liquid structure packing of the vanadate complex was examined with VMD [33].

8.2.2 Force field parameters

Generalized Amber force field (GAFF) format was used for the HVO_4^{2-} anion based on Gaussian09 calculations at the B3LYP level of theory with the 6-31G(d) basis sets for O and H and the LANL2DZ effective-core potential for V. Restrained electrostatic potential (RESP) charges were obtained from fitting into the electrostatic potential from Gaussian09 calculations. The van der Waals parameter for V was taken from the UFF while those for O and H from AMBER [51]. Bond stretching, bond bending, and dihedral angle parameters were from fitting the potential energy curves from Gaussian09 scanning.

8.2.3 Classical MD

To investigate Na_2HVO_4 in water, both fresh and seawater were used: the fresh water model contains 1500 water molecules, while the seawater model contains additional 15 Na^+ and Cl^- ions, to mimic the salinity of seawater at 0.54 M NaCl. The TIP3P model was used for water, while the vdW parameters for Na^+ and Cl^- ions are the same as used previously [45]. Before an unconstrained production run, a sequence of constrained steps was employed to keep the sodium's localized around the vanadate complex: first, a simple minimization step with 2000 optimization steps; second, a NVT heating run from 0 K to 300 K for 100 ps with a 1fs time; next, a 10 ns NPT equilibration step for optimal volume and density. After an equilibration run, a 100 ns unconstrained production run was performed. For the production run, the temperature was kept constant using the Nose-Hover thermostat at 300 K, and the geometry of the water molecules was held fix with the SHAKE algorithm.

8.2.4 Umbrella Sampling

The potential of mean force (PMF) simulation via umbrella sampling was performed to obtain the free-energy profile of $NaHVO_4^-$ dissociation into HVO_4^{2-} and Na^+. A bias potential of 40 kcal/mol along the reaction coordinate (the Na-V distance, r_{Na-V}) drove the system from an initial $NaHVO_4^-$ thermodynamic state to a final HVO_4^{2-} (product). Starting at r_{Na-V}=3.0 Å the system took intermediate steps of 0.1 Å that was covered by a series of windows performed at 10 ns time frame to a final 6.0 Å. All windows were then stitched together with the Weighted Histogram Analysis Method (WHAM) to generate the PMF.

8.3 Results and discussion

8.3.1 DFT-MD analysis of Na_2HVO_4 in water

To investigate the most stable vanadate structure, we simulated the interaction of vanadate in water with DFT-MD using the Na_2HVO_4 salt as the initial state. Figure 8-1 shows a molecular model of Na_2HVO_4: a tetrahedral structure that is charge balanced with two sodium ions within close proximity of vanadate's oxygens. Two types of vanadate oxygens exist: a protonated V-OH group and three unprotonated V-O groups. To study the solvation of sodium ions, we monitored

the interaction of sodium ions to vanadium. In the 50-ps DFT-MD simulation, the dissolution of one sodium ion was observed. In the case of a simulation cell of 50 water molecules, the dissociating sodium departure is at about 6 ps (Figure 8-2a), while in the case of 100 water molecules, the dissociation of the sodium is around 8 ps (Figure 8-2b). One can also see that during the 50-ps time frame, one sodium ion remains associated with the vanadate anion as $NaHVO_4^-$. Limited by the accessible timescale of our DFT-MD simulation, we could not examine the dissolution of the remaining sodium ion from the brute-force DFT-MD simulation. So we turn to classical MD which allows us to simulate Na_2HVO_4 in both pure water and seawater for a much longer time scale.

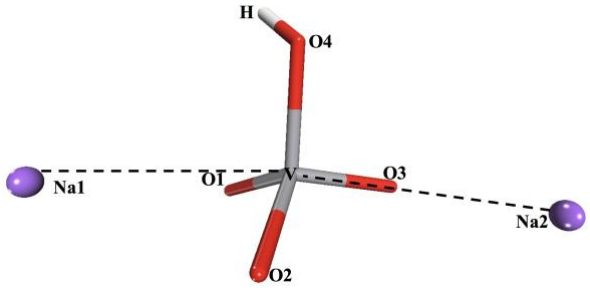

Figure 8-1 A snapshot of Na_2HVO_4 used as the initial state in the simulation.

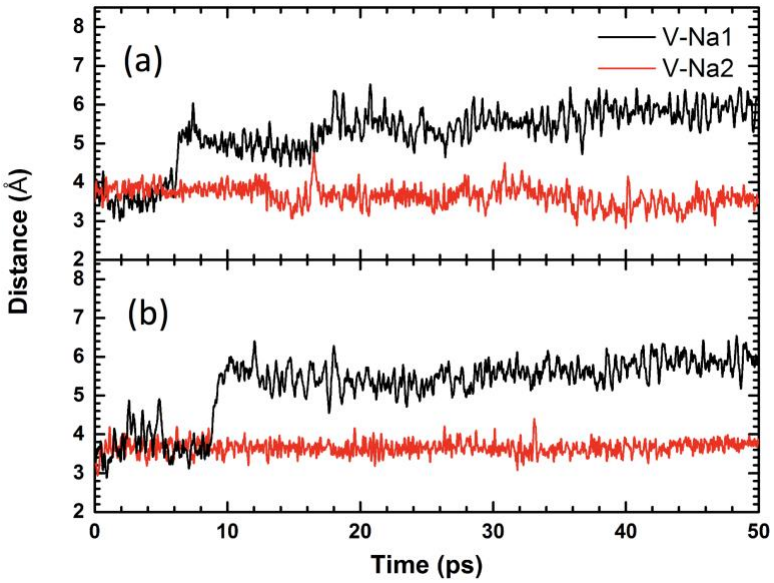

Figure 8-2 V-Na1 and V-Na2 distances as a function of time, starting with Na_2HVO_4 (Figure **8-1**) in water, from DFT-MD: (a) in a simulation cell of 50 water molecules; (b) in a simulation cell of 100 water molecules.

8.3.2 Classical molecular dynamics of Na_2HVO_4 in pure water and seawater

To further follow the dissolution of the two sodium ions, we first explore the coordination number (CN) of sodium ions around the vanadate in a 100-ns time frame. In pure water (Figure 8-3a), we found that both sodium ions can dissociate away and spend most of their time away from the HVO_4^{2-} anion (CN=0), while one sodium ion often associates with the HVO_4^{2-} anion (CN=1) and occasionally two sodium ions associate with the HVO_4^{2-} anion at the same time (CN=2). In seawater conditions (Figure 8-3b), we found that both sodium ions can dissociate away from the

HVO_4^{2-} anion (CN=0), but the most probable CN is between 1 and 2; sometimes there are three and even four sodium ions around the HVO_4^{2-} anion.

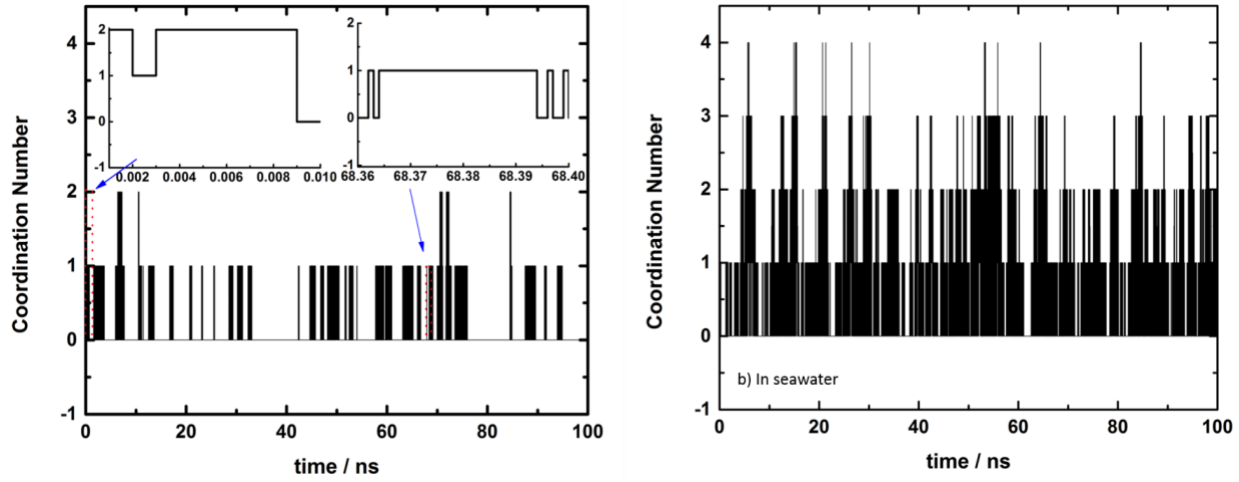

Figure 8-3 Change of coordination number of Na^+ ions around V with time from 100-ns classical molecular dynamics simulations: (a) in pure water; (b) in NaCl solution.

Averaging over the 100-ns trajectories in Figure 8-3, we obtained the radial distribution function (RDF) of sodium ions around V (Figure 8-4). In both pure water and seawater, two peaks can be seen at 2.95 Å and 3.55 Å. These peaks represent two interacting sites around the vanadate complex. The snapshots in Figure 8-5 show that the 2.95-Å site corresponds to a state where Na^+ interacting with two oxo groups (Na-O_V distances at about 2.42 and 2.54 Å), while the 3.55-Å site corresponds to a state where Na^+ interacting with one oxo group (Na-O_V distance at about 2.30 Å). Furthermore, CN from the integrated RDF shows that there is 0.3 Na^+ within a 4.0-Å radius around V in pure water, while there are 1.5 Na^+ around V in seawater.

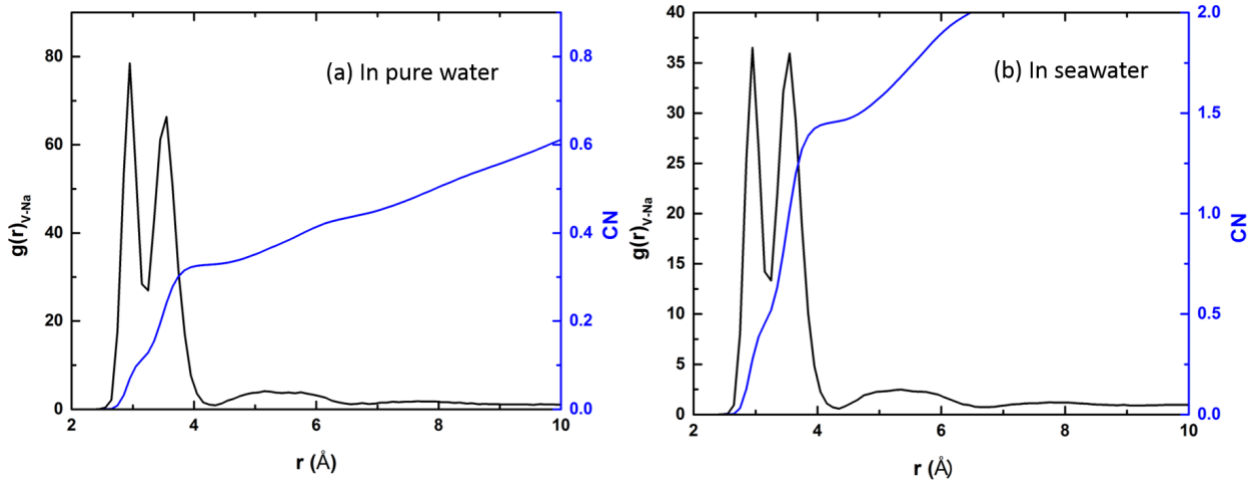

Figure 8-4 Radial distribution function (black) and coordination number (blue) of Na^+ ions around V averaged over 50-ns trajectories of classical molecular dynamics simulations: (a) in pure water; (b) in seawater.

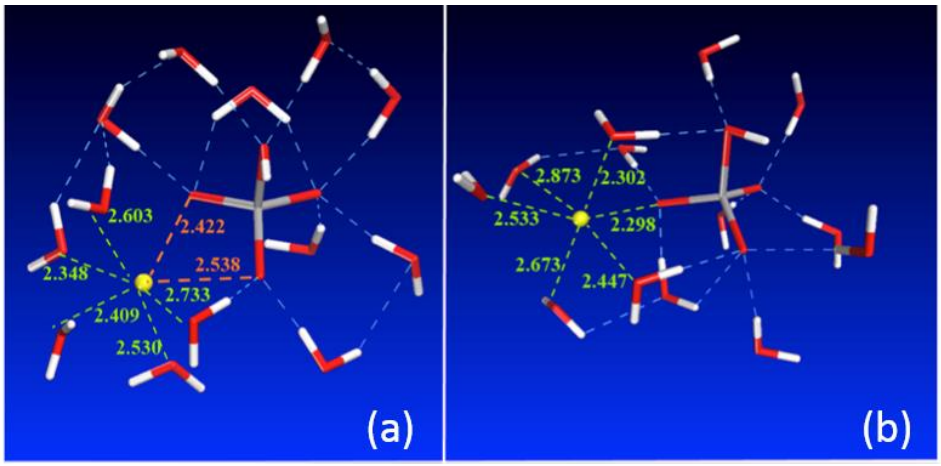

Figure 8-5 Snapshots of two states of $NaHVO_4^-$ in pure water, corresponding to the two peaks in radial distribution function of Na around V in Figure **8-4**: (a) $r_{V\text{-}Na}$ = 2.95 Å; (b) $r_{V\text{-}Na}$ = 3.55 Å. Na, yellow; V, gray; O, red; H, white.

8.3.3 Salt effect on hydrogen bonding

The CN of sodium ions around the vanadate anion is closely related to the hydrogen-bond network. So we explored the hydrogen bond lifetime of the vanadate anion in pure water and in seawater. To define the hydrogen bonds between water and the vanadate, we used geometrical criteria of the O-H---O distance within 3.0 Å and angles greater than 135°. From Figure 8-6, one can see that a longer lifetime of hydrogen bonds around the vanadate anion is observed in pure water than in seawater. So the existence of a high concentration of NaCl disrupts the hydrogen-bond network around the vanadate anion, thereby accelerating the hydrogen-bond dynamics. This is consistent with our finding that 1.5 sodium ions are closely associated with the vanadate anion as shown in the RDF plot (Figure 8-4b).

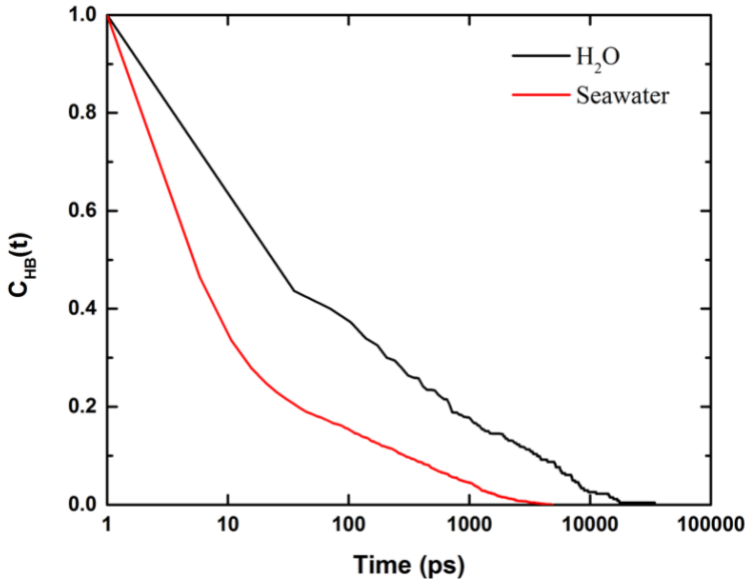

Figure 8-6 Hydrogen bond autocorrelation function, $C_{HB}(t)$, for water molecules hydrogen-bonded to HVO_4^{2-} in pure water (black) and in seawater (red).

The effects of adding NaCl on the solvation of the vanadate can be further inspected from the number of hydrogen bonds around each V-O group. Table 8-1 shows the average number of hydrogen bonds over the 100-ns trajectory. In pure water, the oxo groups (O1, O2, and O3) of vanadate (Figure 8-1) are calculated to accept about three hydrogens from surrounding waters, whereas the –OH group (O4) of vanadate accepts two. In seawater, the average number of hydrogen bonds decreases by about 0.3 to 0.4, as the sodium ions now compete with water molecules for the interaction with the vanadate anion.

Table 8-1 Average number of hydrogen bonds with the V-O groups of vanadate over 100-ns trajectory

V-O	In pure water	In seawater
V-O1	3.03 ± 0.68	2.74 ± 0.89
V-O2	3.06 ± 0.65	2.77 ± 0.86
V-O3	3.08 ± 0.63	2.83 ± 0.83
V-O4	2.24 ± 0.69	1.86 ± 0.89

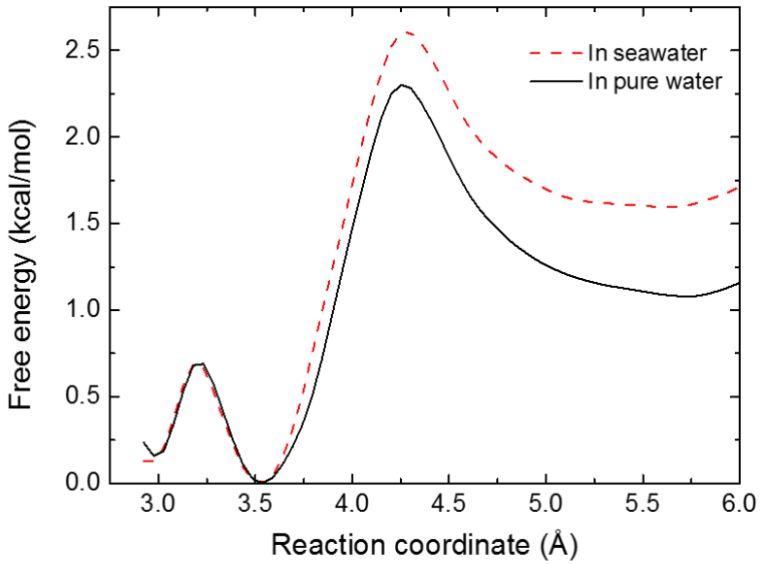

Figure 8-7 Free-energy profile from the potential of mean force of $NaHVO_4^-$ dissociation to HVO_4^{2-} and Na^+ in pure water and in seawater. Reaction coordinate is defined as the V-Na distance.

8.3.4 Free-energy dissociation of $NaHVO_4^-$

The DFT-MD and CMD simulations above show the high probability of the vanadate anion with a sodium ion associated with it to form $NaHVO_4^-$. To examine the free-energy profile for this sodium ion to dissociate away from the vanadate, we used umbrella sampling with our CMD simulations to obtain the potential of mean force (PMF). Figure 8-7 shows the free-energy profile of $NaHVO_4^-$ dissociation to HVO_4^{2-} and Na^+ in pure water and in seawater. One can see that the sodium ion in $NaHVO_4^-$ exists in two states, one with V-Na distance of 2.95 ± 0.15 Å and the other

with V-Na distance of 3.5 ± 0.25 Å, as already shown in the RDF plot in Figure 8-4 and in the snapshots in Figure 8-5. The two states are separated by a small barrier of ~0.7 kcal/mol. From the 3.5-Å state, the sodium ion can then break away with a barrier of 2.2 kcal/mol in pure water and 2.5 kcal/mol in seawater; both barriers are small enough that we observed many crossings in our brute-force MD simulations at 300 K (Figure 8-2). At the transition state (Figure 8-8a), the snapshot shows that the Na-O_V distance is at about 2.63 Å and the Na^+ ion is surrounded by five water molecules. Figure 8-7 also shows that the associated state ($NaHVO_4^-$) is more stable than the dissociated state (HVO_4^{2-} and Na^+). In addition, this stability is enhanced in seawater than in pure water. In the dissociated state, the snapshot sows that the Na^+ ion is now surrounded by six water molecules (Figure 8-8b).

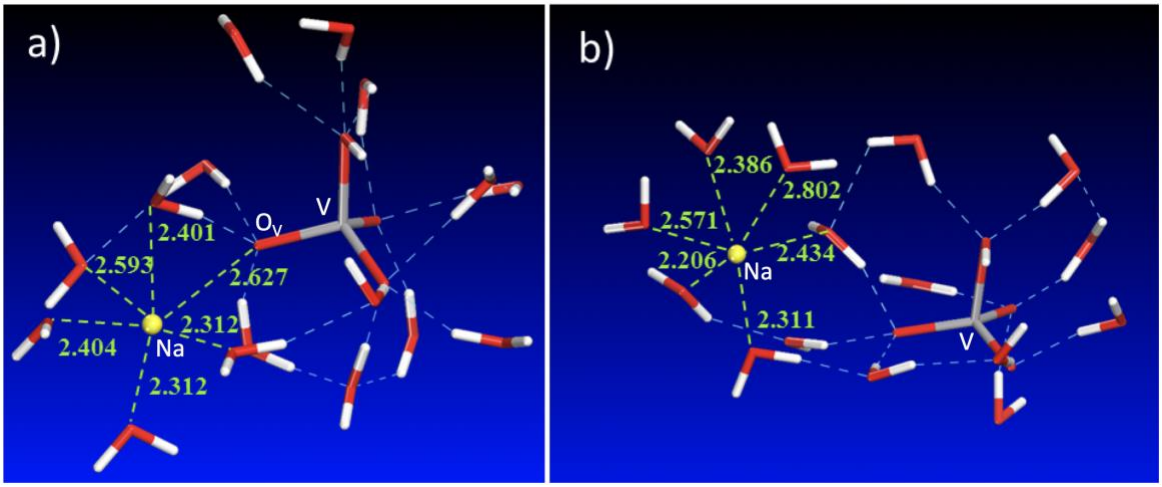

Figure 8-8 Snapshots along the potential of mean force (PMF) of $NaHVO_4^-$ dissociating into HVO_4^{2-} and Na^+: (a) transition state (at a Na-V distance of ~4.25 Å in Figure **8-7**); (b) after dissociation (at a Na-V distance of ~5.75 Å in Figure **8-7**). Na, yellow; V, gray; O, red; H, white.

8.4 Conclusions

In summary, we have examined the solvation of the vanadate anion (HVO_4^{2-}) with molecular dynamics simulations. Starting with Na_2HVO_4, DFT-MD showed that one Na^+ ion quickly dissociates away within a few ps, while the second Na^+ ion remains associated within the timescale of 50 ps. Classical MD simulations on the time scale of 100 ns showed that the fully dissociated state (HVO_4^{2-}) is most probable in pure water, while in seawater $NaHVO_4^-$ is the most probable state. Relaxation of hydrogen bonds around the vanadate anion was found to be faster in seawater than in pure water due to the disruption of the hydrogen-bond network by the Na^+ ions. Potential of mean force for $NaHVO_4^-$ dissociation into HVO_4^{2-} and Na^+ ion revealed a smaller barrier of ~2.5 kcal/mol. Our simulations show the importance of Na^+ ions in the solvation and speciation of vanadate in seawater; this knowledge will be useful for further understanding of the uranium/vanadium selectivity in ligand binding and design for seawater uranium recovery.

9 Computational Analysis of Enthalpy and Entropy Contributions to Uranium and Vanadium Complexation and its Implications in Uranium/Vanadium Selectivity

9.1 Introduction

Following the discussions in Chapter 8, it is known that vanadium is the main competitor for uranium extraction from seawater. Some of the state-of-the-art amidoxime ligands even prefer binding of vanadium over uranium.[74,99] Therefore, increasing the uranium/vanadium selectivity is essential to design effective strategy to extract uranium from seawater. Recently, temperature-dependent uptake data of uranium and vanadium based on two high-capacity adsorbents AF1 and AI8 developed by ORNL are published by the PNNL group.[110] Their results show that the sorption of U(VI) is highly endothermic while the sorption of V(V) is much less sensitive to temperature. This indicates that temperature can be used as a lever to control the uranium/vanadium selectivity. In this Chapter, we will address the different entropy and enthalpy contributions of uranium and vanadium uptake from the computational perspective. Understanding the origin of this difference will be helpful to design and choose candidates with high uranium/vanadium selectivity.

9.2 Computational Details

All the simulations are carried out with CMD methods implemented in the AMBER 16 package. The 0.5 M NaCl concentration is used to mimic the seawater condition. The open-chain amidoxime (glutardiamidoxime: $\mathbf{B}^{2-}$) discussed in Chapter 5 and Chapter 7 is used as the binding ligand. Since the dominated species of uranium in seawater is $Ca_2UO_2(CO_3)_3$, we use the complexation of uranyl involving $\mathbf{B}^{2-}$ displacing the second CO_3^{2-} group of $Ca_2UO_2(CO_3)_3$ to model the uranium uptake. For the vanadium uptake model, we directly employed the binding of $\mathbf{B}^{2-}$ with vanadyl (VO_2^+). Umbrella sampling technique is used to obtain the free energy of the displacing and binding processes. The calculations are performed with temperatures being set to 285-315 K with 15 K interval for U binding and extended to 345 K for V binding which is less sensitive to temperature changes. All the force field parameters and other calculation inputs are kept the same with those used in Chapter 5 and Chapter 7.

9.3 Results and discussion

9.3.1 Enthalpy and entropy contributions for U binding

We first compare the free energy profiles for the U binding process at different temperatures in Figure 9-1. The initial state **B5**, intermediate **B6** and final state **B7** are marked on the free energy profiles along with their structures showing in Figure 9-1(b). As the temperature increase from 285 K to 315 K, the free energy difference between **B5** and **B6** decreases from 11.5 kJ/mol to 2.5 kJ/mol. The increasing temperature makes the formation of the intermediate **B6** much easier. As a result, the free energy change from **B5** to final state **B7** is reduced from –9.8 kJ/mol to –18.3 kJ/mol. By looking at the structure of **B6** in Figure 9-1(b), we can see that the intermediate involves the bidentate binding CO_3^{2-} transformed from its monodentate binding form with the uranium complex in the initial state, which is endothermic at 285 K and benefited from higher temperature.

We further applied van't Hoff Equation to fit the logarithm of the equilibrium constant K which can be calculated from free energy ΔG with the inverse of temperature T to determine the enthalpy ΔH and entropy ΔS

$$\ln K = -\left(\frac{\Delta H}{R}\right)\frac{1}{T} + \frac{\Delta S}{R} \tag{9.1}$$

in which *R* is the gas constant. The fitted results are shown in Figure 9-2 and based on the fitted parameters the values of Δ*H* and Δ*S* are calculated in Table 9-1. Our estimated Δ*H* of 65 kJ/mol and Δ*S* of 0.264 kJ/K/mol are in good agreement with the experimental data for both AF1 and AI8 sorbents.[110] Two insights are gained upon this agreement: (1) since it is confirmed both from simulation and experiments that the uranium complexation by amidoxime is endothermic, we can expect the improved uranium uptake from higher operating temperatures; (2) the large positive entropy change suggests that the chelate effect which we studied in Chapter 7 is important when considering the ligand exchange with carbonate.

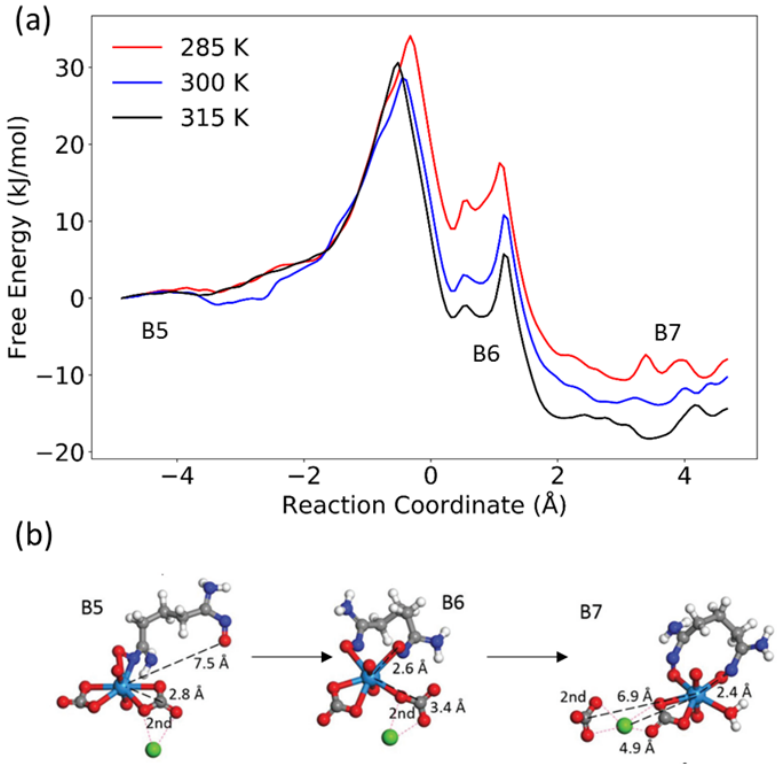

Figure 9-1 (a) Free energy profiles for the uranium complexation from 285-315 K and (b) the structures of the initial state **B5**, intermediate state B6 and final state **B7**.

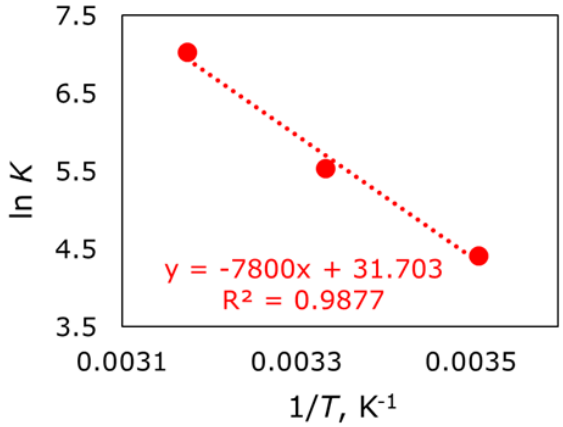

Figure 9-2 van't Hoff plots (ln K vs 1/T) for the complexation of U(VI) with open-chain B^{2-} ligand.

Table 9-1 Comparison between simulations and experiments[110] for enthalpy and entropy contributions to U(VI) and V(V) bindings with the amidoxime ligands

Reaction	Δ*H* and Δ*S*	Simulation	Expt. (AF1)	Expt. (AI8)
U + Amidoxime	Δ*H* (kJ/mol)	65 ± 7	57 ± 6	59 ± 11
	Δ*S* (kJ/K/mol)	0.26 ± 0.02	0.31 ± 0.02	0.32 ± 0.04
V + Amidoxime	Δ*H* (kJ/mol)	–11 ± 3	6.1 ± 5.9	–11 ± 6
	Δ*S* (kJ/K/mol)	0.05 ± 0.01	0.16 ± 0.02	0.10 ± 0.02

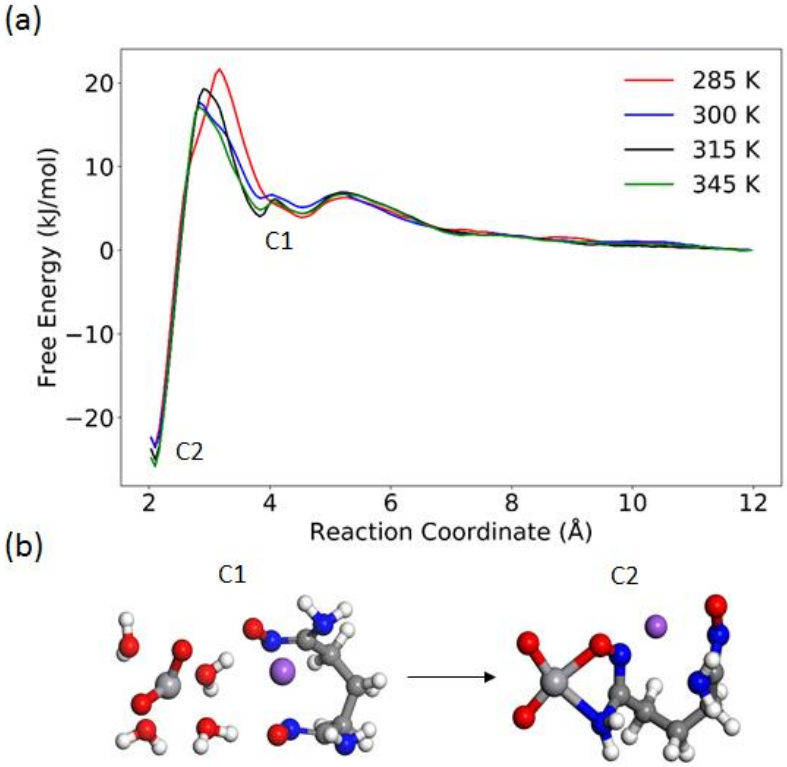

Figure 9-3 (a) Free energy profiles for the VO_2^+ binding process from 285-345 K and (b) the structures of the intermediate state **C1** and final state **C2**.

9.3.2 Enthalpy and entropy contributions for V binding

The free energy profiles of the binding of VO_2^+ with B^{2-} at different temperatures are shown in Figure 9-3(a). The structure of intermediate **C1** and final sate **C2** in Figure 9-3(b), the initial state involves the free ions separated from each other more than 12 Å. From the free energy profiles, we noticed that free energy change of either in the formation of **C1** or **C2** is less than 2.5 kJ/mol when the temperature increases from 285 K to 345 K. By inspecting the intermediate structure of **C1**, we see that it features the hydrogen bonding of two water molecules in the first solvation shell of VO_2^+ with the oxime oxygen of B^{2-} ligand. Increasing the temperature has small impact on the deep free energy drop of forming the binding state **C2**.

Like the U binding process, we applied van't Hoff equation to fit the free energy data in Figure 9-4 and calculated the enthalpy ΔH=11 kJ/mol and entropy ΔS=0.045 kJ/K/mol (Table 9-1). These values are close to the experimental data of the AI8 sorbent for V(V) binding which is slightly exothermic with a positive entropy change.[110] In contrast, the experimental data of AF1 sorbent shows that its binding with V(V) is slightly endothermic. This suggests that the majority of the amidoxime ligands in AF1 are not the open-chain form.

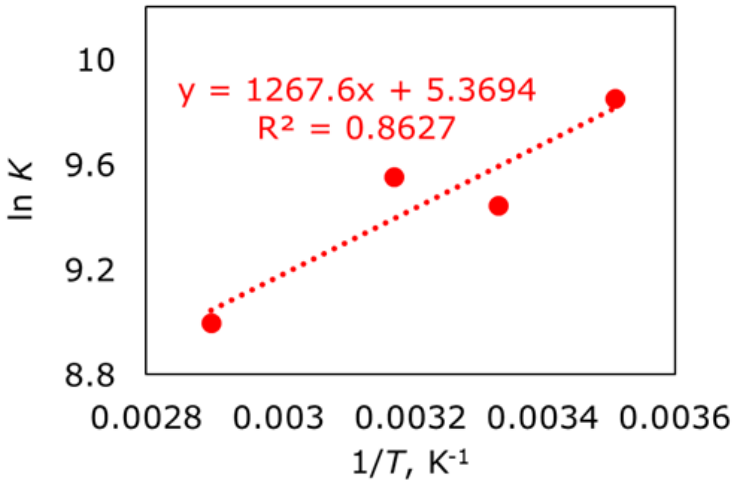

Figure 9-4 van't Hoff plots (ln K vs 1/T) for the binding of V(V) with open-chain $\mathbf{B}^{2-}$ ligand.

9.4 Conclusions

In this chapter we performed computational analyses of free energies of binding at different temperatures to obtain enthalpy and entropy contributions to uranium and vanadium bindings. We found that uranium complexation with the open-chain amidoxime is endothermic and has a large positive entropy change, in very good agreement with the experiment for both AF1 and AI8 sorbents. In contrast, vanadium complexation with the open-chain amidoxime is slightly exothermic and has a smaller positive entropy change, in good agreement with the experiment for the AI8 sorbent but different from that for the AF1 sorbent. Hence, use of the open-chain amidoxime at higher temperatures is a very good way to increase U/V selectivity.

10 References

(1) Seko, N.; Katakai, A.; Hasegawa, S.; Tamada, M.; Kasai, N.; Takeda, H.; Sugo, T.; Saito, K. Aquaculture of Uranium in Seawater by a Fabric-Adsorbent Submerged System. *Nucl. Technol.* **2003,** *144*, 274-278.

(2) Kim, J.; Tsouris, C.; Mayes, R. T.; Oyola, Y.; Saito, T.; Janke, C. J.; Dai, S.; Schneider, E.; Sachde, D. Recovery of Uranium from Seawater: A Review of Current Status and Future Research Needs. *Sep. Sci. Technol.* **2013,** *48*, 367-387.

(3) Tian, G. X.; Teat, S. J.; Zhang, Z. Y.; Rao, L. F. Sequestering Uranium from Seawater: Binding Strength and Modes of Uranyl Complexes with Glutarimidedioxime. *Dalton Trans.* **2012,** *41*, 11579-11586.

(4) Sun, X. Q.; Xu, C.; Tian, G. X.; Rao, L. F. Complexation of Glutarimidedioxime with Fe(III), Cu(II), Pb(II), and Ni(II), the Competing Ions for the Sequestration of U(VI) from Seawater. *Dalton Trans.* **2013,** *42*, 14621-14627.

(5) Tian, G. X.; Teat, S. J.; Rao, L. F. Thermodynamic Studies of U(VI) Complexation with Glutardiamidoxime for Sequestration of Uranium from Seawater. *Dalton Trans.* **2013,** *42*, 5690-5696.

(6) Pan, H. B.; Liao, W. S.; Wai, C. M.; Oyola, Y.; Janke, C. J.; Tian, G. X.; Rao, L. F. Carbonate-H_2O_2 Leaching for Sequestering Uranium from Seawater. *Dalton Trans.* **2014,** *43*, 10713-10718.

(7) Sun, X. Q.; Tian, G. X.; Xu, C.; Rao, L. F.; Vukovic, S.; Kang, S. O.; Hay, B. P. Quantifying the Binding Strength of U(VI) with Phthalimidedioxime in Comparison with Glutarimidedioxime. *Dalton Trans.* **2014,** *43*, 551-557.

(8) Lee, J. Y.; Yun, J. I. Formation of Ternary $CaUO_2(CO_3)_3^{2-}$ and $Ca_2UO_2(CO_3)_3(aq)$ Complexes under Neutral to Weakly Alkaline Conditions. *Dalton Trans.* **2013,** *42*, 9862-9869.

(9) Endrizzi, F.; Rao, L. Chemical Speciation of Uranium(VI) in Marine Environments: Complexation of Calcium and Magnesium Ions with $[(UO_2)(CO_3)_3]^{4-}$ and the Effect on the Extraction of Uranium from Seawater. *Chem. Eur. J.* **2014,** *20*, 14499-14506.

(10) Vukovic, S.; Watson, L. A.; Kang, S. O.; Custelcean, R.; Hay, B. P. How Amidoximate Binds the Uranyl Cation. *Inorg. Chem.* **2012,** *51*, 3855-3859.

(11) Vukovic, S.; Hay, B. P. De Novo Structure-Based Design of Bis-amidoxime Uranophiles. *Inorg. Chem.* **2013,** *52*, 7805-7810.

(12) Abney, C. W.; Liu, S. B.; Lin, W. B. Tuning Amidoximate to Enhance Uranyl Binding: A Density Functional Theory Study. *J. Phys. Chem. A* **2013,** *117*, 11558-11565.

(13) Wang, C. Z.; Lan, J. H.; Wu, Q. Y.; Luo, Q.; Zhao, Y. L.; Wang, X. K.; Chai, Z. F.; Shi, W. Q. Theoretical Insights on the Interaction of Uranium with Amidoxime and Carboxyl Groups. *Inorg. Chem.* **2014,** *53*, 9466-76.

(14) Morse, J. W.; Shanbhag, P. M.; Saito, A.; Choppin, G. R. Interaction of Uranyl Ions in Carbonate Media. *Chem. Geol.* **1984,** *42*, 85-99.

(15) Bernhard, G.; Geipel, G.; Brendler, V.; Nitsche, H. Speciation of Uranium in Seepage Waters of a Mine Tailing Pile Studied by Time-resolved Laser-induced Fluorescence Spectroscopy (TRLFS). *Radiochim. Acta* **1996,** *74*, 87-91.

(16) Bernhard, G.; Geipel, G.; Reich, T.; Brendler, V.; Amayri, S.; Nitsche, H. Uranyl(VI) Carbonate Complex Formation: Validation of the $Ca_2UO_2(CO_3)_3(aq.)$ Species. *Radiochim. Acta* **2001,** *89*, 511-518.

(17) Kelly, S. D.; Kemner, K. M.; Brooks, S. C. X-ray Absorption Spectroscopy Identifies Calcium-uranyl-carbonate Complexes at Environmental Concentrations. *Geochim. Cosmochim. Acta* **2007,** *71*, 821-834.
(18) Di Bernardo, P.; Zanonato, P. L.; Benetollo, F.; Melchior, A.; Tolazzi, M.; Rao, L. F. Energetics and Structure of Uranium(VI)-Acetate Complexes in Dimethyl Sulfoxide. *Inorg. Chem.* **2012,** *51*, 9045-9055.
(19) Xu, C.; Tian, G. X.; Teat, S. J.; Rao, L. F. Complexation of U(VI) with Dipicolinic Acid: Thermodynamics and Coordination Modes. *Inorg. Chem.* **2013,** *52*, 2750-2756.
(20) Leggett, C. J.; Rao, L. F. Complexation of Calcium and Magnesium with Glutarimidedioxime: Implications for the Extraction of Uranium from Seawater. *Polyhedron* **2015,** *95*, 54-59.
(21) Kubicki, J. D.; Halada, G. P.; Jha, P.; Phillips, B. L. Quantum Mechanical Calculation of Aqueuous Uranium Complexes: Carbonate, Phosphate, Prganic and Biomolecular species. *Chem. Cent. J.* **2009,** *3*, 11402-11411.
(22) Tirler, A. O.; Weiss, A. K. H.; Hofer, T. S. A Comparative Quantum Mechanical Charge Field Study of Uranyl Mono- and Dicarbonate Species in Aqueous Solution. *J. Phys. Chem. B* **2013,** *117*, 16174-16187.
(23) Tirler, A. O.; Hofer, T. S. Structure and Dynamics of the Uranyl Tricarbonate Complex in Aqueous Solution: Insights from Quantum Mechanical Charge Field Molecular Dynamics. *J. Phys. Chem. B* **2014,** *118*, 12938-12951.
(24) Kerisit, S.; Liu, C. Molecular Simulation of the Diffusion of Uranyl Carbonate Species in Aqueous Solution. *Geochim. Cosmochim. Acta* **2010,** *74*, 4937-4952.
(25) Kerisit, S.; Liu, C. Structure, Kinetics, and Thermodynamics of the Aqueous Uranyl(VI) Cation. *J. Phys. Chem. A* **2013,** *117*, 6421-6432.
(26) Kresse, G.; Hafner, J. Ab initio Molecular Dynamics for Liquid Metals. *Phys. Rev. B* **1993,** *47*, 558.
(27) Kresse, G.; Furthmuller, J. Efficiency of ab-initio Total Energy Calculations for Metals and Semiconductors Using a Plane-wave Basis Set. *Comput. Mater. Sci* **1996,** *6*, 15-50.
(28) Blöchl, P. E. Projector Augmented-wave Method. *Phys. Rev. B* **1994,** *50*, 17953-17979.
(29) Kresse, G.; Joubert, D. From Ultrasoft Pseudopotentials to the Projector Augmented-wave Method. *Phys. Rev. B* **1999,** *59*, 1758-1775.
(30) Perdew, J. P.; Burke, K.; Wang, Y. Generalized Gradient Approximation for the Exchange-correlation Hole of a Many-electron System. *Phys. Rev. B* **1996,** *54*, 16533.
(31) DiStasio, R. A.; Santra, B.; Li, Z. F.; Wu, X. F.; Car, R. The Individual and Collective Effects of Exact Exchange and Dispersion Interactions on the ab initio Structure of Liquid Water. *J. Chem. Phys.* **2014,** *141*.
(32) Forster-Tonigold, K.; Gross, A. Dispersion Corrected RPBE Studies of Liquid Water. *J. Chem. Phys.* **2014,** *141*.
(33) Humphrey, W.; Dalke, A.; Schulten, K. VMD: Visual Molecular Dynamics. *J. Mol. Graph.* **1996,** *14*, 33-38.
(34) Mereiter, K. The Crystal-Structure of Liebigite, $Ca_2UO_2(CO_3)_3$.Approximately $11H_2O$. *Tscher. Mineral. Petr. Mitt.* **1982,** *30*, 277-288.
(35) Denning, R. G. Electronic Structure and Bonding in Actinyl Ions and their Analogs. *J. Phys. Chem. A* **2007,** *111*, 4125-4143.

(36) Doudou, S.; Arumugam, K.; Vaughan, D. J.; Livens, F. R.; Burton, N. A. Investigation of Ligand Exchange Reactions in Aqueous Uranyl Carbonate Complexes Using Computational Approaches. *Phys. Chem. Chem. Phys.* **2011,** *13*, 11402-11411.
(37) Chen, J.; Zhang, H.; Rentzepis, P. M. Bond Evolution in Electron Transfer: A Time-Resolved EXAFS Study. *J. Phys. Chem. A* **2010,** *114*, 2751-2756.
(38) Zhang, B.; Guo, X.; Xie, S.; Liu, X.; Ling, C.; Ma, H.; Yu, M.; Li, J. Synergistic Nanofibrous Adsorbent for Uranium Extraction from Seawater. *RSC Adv.* **2016,** *6*, 81995-82005.
(39) Guilbaud, P.; Wipff, G. Hydration of Uranyl (UO_2^{2+}) Cation and Its Nitrate Ion and 18-crown-6 Adducts Studied by Molecular Dynamics Simulations. *J. Phys. Chem.* **1993,** *97*, 5685-5692.
(40) Guilbaud, P.; Wipff, G. Force Field Representation of the UO_2^{2+} Cation from Free Energy MD Simulations in Water. Tests on its 18-crown-6 and NO_3^- Adducts, and on its Calix[6]arene^{6-} and CMPO Complexes. *J. Mol. Struct. Theochem* **1996,** *366*, 55-63.
(41) Jorgensen, W. L.; Chandrasekhar, J.; Madura, J. D.; Impey, R. W.; Klein, M. L. Comparison of Simple Potential Functions for Simulating Liquid Water. *J. Chem. Phys.* **1983,** *79*, 926-935.
(42) Wang, J. M.; Wolf, R. M.; Caldwell, J. W.; Kollman, P. A.; Case, D. A. Development and Testing of a General Amber Force Field. *J. Comput. Chem.* **2004,** *25*, 1157-1174.
(43) Pavese, A.; Catti, M.; Price, G. D.; Jackson, R. A. Interatomic Potentials for $CaCO_3$ Polymorphs (Calcite and Aragonite), Fitted to Elastic and Vibrational Data. *Phys. Chem. Miner.* **1992,** *19*, 80-87.
(44) deLeeuw, N. H.; Parker, S. C. Atomistic Simulation of the Effect of Molecular Adsorption of Water on the Surface Structure and Energies of Calcite Surfaces. *J. Chem. Soc. Faraday Trans.* **1997,** *93*, 467-475.
(45) Joung, I. S.; Cheatham, T. E. Determination of Alkali and Halide Monovalent Ion Parameters for Use in Explicitly Solvated Biomolecular Simulations. *J. Phys. Chem. B* **2008,** *112*, 9020-9041.
(46) Plimpton, S. Fast Parallel Algorithms for Short-Range Molecular Dynamics. *J. Comput. Phys.* **1995,** *117*, 1-19.
(47) Love, D. L.; Sam, D. Radiochemical Determination of Sodium-24 and Sulfur-35 in Seawater. *Anal. Chem.* **1962,** *34*, 336-340.
(48) Ewald, P. P. Die Berechnung optischer und elektrostatischer Gitterpotentiale. *Ann. Phys.* **1921,** *369*, 253-287.
(49) Hoover, W. G. Canonical Dynamics: Equilibrium Phase-space Distributions. *Phys. Rev. A* **1985,** *31*, 1695-1697.
(50) Ryckaert, J. P.; Ciccotti, G.; Berendsen, H. J. C. Numerical Integration of the Cartesian Equations of Motion of a System with Constraints: Molecular Dynamics of n-Alkanes. *J. Comput. Phys.* **1977,** *23*, 327-341.
(51) Case, D. A.; Babin, V.; Berryman, J. T.; Betz, R. M.; Cai, Q.; Cerutti, D. S.; Cheatham, I., T. E. ; Darden, T. A.; Duke, R. E.; Gohlke, H., et al. *AMBER 14*, University of California, San Francisco: San Francisco, CA, 2014.
(52) Fermann, J. T.; Moniz, T.; Kiowski, O.; McIntire, T. J.; Auerbach, S. M.; Vreven, T.; Frisch, M. J. Modeling Proton Transfer in Zeolites: Convergence Behavior of Embedded and Constrained Cluster Calculations. *J. Chem. Theory Comput.* **2005,** *1*, 1232-9.
(53) Lee, C. T.; Yang, W. T.; Parr, R. G. Development of the Colle-Salvetti Correlation-Energy Formula into a Functional of the Electron-Density. *Phys. Rev. B* **1988,** *37*, 785-789.

(54) Becke, A. D. Density-Functional Thermochemistry .3. The Role of Exact Exchange. *J. Chem. Phys.* **1993,** *98*, 5648-5652.
(55) Danovich, D.; Hrusak, J.; Shaik, S. Ab initio Calculations for Small Iodo Clusters - Good Performance of Relativistic Effective Core Potentials. *Chem. Phys. Lett.* **1995,** *233*, 249-256.
(56) Harihara.Pc; Pople, J. A. Influence of Polarization Functions on Molecular-Orbital Hydrogenation Energies. *Theor. Chim. Acta* **1973,** *28*, 213-222.
(57) Priest, C.; Tian, Z.; Jiang, D.-e. First-principles Molecular Dynamics Simulation of the $Ca_2UO_2(CO_3)_3$ Complex in Water. *Dalton Trans.* **2016,** *45*, 9812-9819.
(58) Kelley, S. P.; Barber, P. S.; Mullins, P. H. K.; Rogers, R. D. Structural Clues to UO_2^{2+}/VO_2^+ Competition in Seawater Extraction Using Amidoxime-Based Extractants. *Chem. Commun.* **2014,** *50*, 12504-12507.
(59) Huang, K.; Wu, Y. T.; Dai, S. Sigmoid Correlations for Gas Solubility and Enthalpy Change of Chemical Absorption of CO_2. *Ind. Eng. Chem. Res.* **2015,** *54*, 10126-10133.
(60) Kerisit, S.; Liu, C. Molecular Dynamics Simulations of Uranyl and Uranyl Carbonate Adsorption at Aluminosilicate Surfaces. *Environ. Sci. Technol.* **2014,** *48*, 3899-3907.
(61) Guillaumont, R.; Fanghänel, T.; Neck, V.; Fuger, J.; Palmer, D. A.; Grenthe, I.; Rand, M. H., *Update on the Chemical Thermodynamics of Uranium, Neptunium, Plutonium, Americium and Technetium*; Elsevier: Amsterdam, The Netherlands, 2003.
(62) Rahaman, A.; Grassian, V. H.; Margulis, C. J. Dynamics of Water Adsorption onto a Calcite Surface as a Function of Relative Humidity. *J. Phys. Chem. C* **2008,** *112*, 2109-2115.
(63) Berendsen, H. J. C.; Postma, J. P. M.; van Gunsteren, W. F.; DiNola, A.; Haak, J. R. Molecular Dynamics with Coupling to an External Bath. *J. Chem. Phys.* **1984,** *81*, 3684.
(64) Darden, T.; York, D.; Pedersen, L. Particle Mesh Ewald: An Nlog(N) Method for Ewald Sums in Large Systems. *J. Chem. Phys.* **1993,** *98*, 10089-10092.
(65) Torrie, G. M.; Valleau, J. P. Nonphysical Sampling Distributions in Monte Carlo Free-Energy Estimation: Umbrella Sampling. *J. Comput. Phys.* **1977,** *23*, 187-199.
(66) Vijayaraj, R.; Van Damme, S.; Bultinck, P.; Subramanian, V. Molecular Dynamics and Umbrella Sampling Study of Stabilizing Factors in Cyclic Peptide-Based Nanotubes. *J. Phys. Chem. B* **2012,** *116*, 9922-9933.
(67) Kumar, S.; Bouzida, D.; Swendsen, R. H.; Kollman, P. A.; Rosenberg, J. M. Liquid-liquid Transition in ST2 Water. *J. Comput. Chem.* **1992,** *13*, 1011-1021.
(68) Souaille, M.; Roux, B. Extension to the Weighted Histogram Analysis Method: Combining Umbrella Sampling with Free Energy Calculations. *Comput. Phys. Commun.* **2001,** *135*, 40-57.
(69) Chialvo, A. A.; Cummings, P. T.; Cochran, H. D.; Simonson, J. M.; Mesmer, R. E. Na^+–Cl^- Ion Pair Association in Supercritical Water. *J. Chem. Phys.* **1995,** *103*, 9379-9387.
(70) Ciavatta, L. The Specific Interaction Theory in Evaluating Ionic Equilibria. *Ann. Chim. (Rome)* **1980,** *70*, 551-567.
(71) Lucks, C.; Rossberg, A.; Tsushima, S.; Foerstendorf, H.; Scheinost, A. C.; Bernhard, G. Aqueous Uranium(VI) Complexes with Acetic and Succinic Acid: Speciation and Structure Revisited. *Inorg. Chem.* **2012,** *51*, 12288-12300.
(72) Das, S.; Brown, S.; Mayes, R. T.; Janke, C. J.; Tsouris, C.; Kuo, L. J.; Gill, G.; Dai, S. Novel Poly(imide dioxime) Sorbents: Development and Testing for Enhanced Extraction of Uranium from Natural Seawater. *Chem. Eng. J.* **2016,** *298*, 125-135.
(73) Brown, S.; Yue, Y.; Kuo, L.-J.; Mehio, N.; Li, M.; Gill, G.; Tsouris, C.; Mayes, R. T.; Saito, T.; Dai, S. Uranium Adsorbent Fibers Prepared by Atom-Transfer Radical Polymerization

(ATRP) from Poly(vinyl chloride)-co-chlorinated Poly(vinyl chloride) (PVC-co-CPVC) Fiber. *Ind. Eng. Chem. Res.* **2016,** *55*, 4139-4148.
(74) Das, S.; Tsouris, C.; Zhang, C.; Kim, J.; Brown, S.; Oyola, Y.; Janke, C. J.; Mayes, R. T.; Kuo, L. J.; Wood, J. R., et al. Enhancing Uranium Uptake by Amidoxime Adsorbent in Seawater: An Investigation for Optimum Alkaline Conditioning Parameters. *Ind. Eng. Chem. Res.* **2016,** *55*, 4294-4302.
(75) Brown, S.; Chatterjee, S.; Li, M.; Yue, Y.; Tsouris, C.; Janke, C. J.; Saito, T.; Dai, S. Uranium Adsorbent Fibers Prepared by Atom-Transfer Radical Polymerization from Chlorinated Polypropylene and Polyethylene Trunk Fibers. *Ind. Eng. Chem. Res.* **2016,** *55*, 4130-4138.
(76) Oyola, Y.; Janke, C. J.; Dai, S. Synthesis, Development, and Testing of High-Surface-Area Polymer-Based Adsorbents for the Selective Recovery of Uranium from Seawater. *Ind. Eng. Chem. Res.* **2016,** *55*, 4149-4160.
(77) Das, S.; Liao, W. P.; Flicker Byers, M.; Tsouris, C.; Janke, C. J.; Mayes, R. T.; Schneider, E.; Kuo, L. J.; Wood, J. R.; Gill, G. A., et al. Alternative Alkaline Conditioning of Amidoxime Based Adsorbent for Uranium Extraction from Seawater. *Ind. Eng. Chem. Res.* **2016,** *55*, 4303-4312.
(78) Abney, C. W.; Mayes, R. T.; Piechowicz, M.; Lin, Z.; Bryantsev, V. S.; Veith, G. M.; Dai, S.; Lin, W. XAFS Investigation of Polyamidoxime-bound Uranyl Contests the Paradigm from Small Molecule Studies. *Energy Environ. Sci.* **2016,** *9*, 448-453.
(79) Guo, X.; Xiong, X.-G.; Li, C.; Gong, H.; Huai, P.; Hu, J.; Jin, C.; Huang, L.; Wu, G. DFT Investigations of Uranium Complexation with Amidoxime-, Carboxyl- and Mixed Amidoxime/Carboxyl-based Host Architectures for Sequestering Uranium from Seawater. *Inorg. Chim. Acta* **2016,** *441*, 117-125.
(80) Astheimer, L.; Schenk, H. J.; Witte, E. G.; Schwochau, K. Development of Sorbers for the Recovery of Uranium from Seawater .2. The Accumulation of Uranium from Seawater by Resins Containing Amidoxime and Imidoxime Functional-Groups. *Sep. Sci. Technol.* **1983,** *18*, 307-339.
(81) Leggett, C. J.; Parker, B. F.; Teat, S. J.; Zhang, Z.; Dau, P. D.; Lukens, W. W.; Peterson, S. M.; Cardenas, A. J. P.; Warner, M. G.; Gibson, J. K., et al. Structural and Spectroscopic Studies of a Rare Non-oxido V(V) Complex Crystallized from Aqueous Solution. *Chem. Sci.* **2016,** *7*, 2775-2786.
(82) Ferrier, M. G.; Batista, E. R.; Berg, J. M.; Birnbaum, E. R.; Cross, J. N.; Engle, J. W.; La Pierre, H. S.; Kozimor, S. A.; Lezama Pacheco, J. S.; Stein, B. W., et al. Spectroscopic and Computational Investigation of Actinium Coordination Chemistry. *Nat. Commun.* **2016,** *7*, 12312.
(83) Holz, M.; Heil, S. R.; Sacco, A. Temperature-dependent Self-diffusion Coefficients of Water and Six Selected Molecular Liquids for Calibration in Accurate 1H NMR PFG Measurements. *Phys. Chem. Chem. Phys.* **2000,** *2*, 4740-4742.
(84) Frisch, M. J. *Gaussian 09*, Gaussian, Inc: Wallingford, CT, 2009.
(85) Wang, J. M.; Wang, W.; Kollman, P. A.; Case, D. A. Automatic Atom Type and Bond Type Perception in Molecular Mechanical Calculations. *J. Mol. Graphics Modell.* **2006,** *25*, 247-260.
(86) Bühl, M.; Wipff, G. Insights into Uranyl Chemistry from Molecular Dynamics Simulations. *ChemPhysChem* **2011,** *12*, 3095-3105.

(87) Kumar, S.; Bouzida, D.; Swendsen, R. H.; Kollman, P. A.; Rosenberg, J. M. The Weighted Histogram Analysis Method for Free-Energy Calculations on Biomolecules .1. The Method. *J. Comput. Chem.* **1992,** *13*, 1011-1021.
(88) Zhang, A. Y.; Asakura, T.; Uchiyama, G. The Adsorption Mechanism of Uranium(VI) from Seawater on a Macroporous Fibrous Polymeric Adsorbent Containing Amidoxime Chelating Functional Group. *React. Funct. Polym.* **2003,** *57*, 67-76.
(89) Katragadda, S.; Gesser, H. D.; Chow, A. The Extraction of Uranium by Amidoximated Orlon. *Talanta* **1997,** *45*, 257-263.
(90) Qin, Z.; Shi, S. W.; Yang, C. T.; Wen, J.; Jia, J. P.; Zhang, X. F.; Yu, H. Z.; Wang, X. L. The Coordination of Amidoxime Ligands with Uranyl in the Gas Phase: a Mass Spectrometry and DFT Study. *Dalton Trans.* **2016,** *45*, 16413-16421.
(91) Liu, X.; Liu, H.; Ma, H.; Cao, C.; Yu, M.; Wang, Z.; Deng, B.; Wang, M.; Li, J. Adsorption of the Uranyl Ions on an Amidoxime-Based Polyethylene Nonwoven Fabric Prepared by Preirradiation-Induced Emulsion Graft Polymerization. *Ind. Eng. Chem. Res.* **2012,** *51*, 15089-15095.
(92) Zhang, L.; Su, J.; Yang, S.; Guo, X.; Jia, Y.; Chen, N.; Zhou, J.; Zhang, S.; Wang, S.; Li, J., et al. Extended X-ray Absorption Fine Structure and Density Functional Theory Studies on the Complexation Mechanism of Amidoximate Ligand to Uranyl Carbonate. *Ind. Eng. Chem. Res.* **2016,** *55*, 4224-4230.
(93) Priest, C.; Li, B.; Jiang, D.-e. Uranyl–Glutardiamidoxime Binding from First-principles Molecular Dynamics, Classical Molecular Dynamics, and Free-Energy Simulations. *Inorg. Chem.* **2017,** *56*, 9497-9504.
(94) He, M.; Liu, X.; Cheng, J.; Lu, X.; Zhang, C.; Wang, R. Uranyl Arsenate Complexes in Aqueous Solution: Insights from First-Principles Molecular Dynamics Simulations. *Inorg. Chem.* **2018,** *57*, 5801-5809.
(95) Kawai, T.; Saito, K.; Sugita, K.; Kawakami, T.; Kanno, J.; Kakakai, A.; Seko, N.; Sugo, T. Preparation of Hydrophilic Amidoxime Fibers by Cografting Acrylonitrile and Methacrylic Acid from an Optimized Monomer Composition. *Radiat. Phys. Chem.* **2000,** *59*, 405-411.
(96) Sieffert, N.; Wipff, G. Uranyl Extraction by N,N-dialkylamide Ligands Studied using Static and Dynamic DFT Simulations. *Dalton Trans.* **2015,** *44*, 2623-2638.
(97) Li, B.; Zhou, J.; Priest, C.; Jiang, D. E. Effect of Salt on the Uranyl Binding with Carbonate and Calcium Ions in Aqueous Solutions. *J. Phys. Chem. B* **2017,** *121*, 8171-8178.
(98) Lashley, M. A.; Mehio, N.; Nugent, J. W.; Holguin, E.; Do-Thanh, C.-L.; Bryantsev, V. S.; Dai, S.; Hancock, R. D. Amidoximes as Ligand Functionalities for Braided Polymeric Materials for the Recovery of Uranium from Seawater. *Polyhedron* **2016,** *109*, 81-91.
(99) Suzuki, T.; Saito, K.; Sugo, T.; Ogura, H.; Oguma, K. Fractional Elution and Determination of Uranium and Vanadium Adsorbed on Amidoxime Fiber from Seawater. *Anal. Sci.* **2000,** *16*, 429-432.
(100) Collier, R. W. Particulate and Dissolved Vanadium in the North Pacific-Ocean. *Nature* **1984,** *309*, 441-444.
(101) Abbasse, G.; Ouddane, B.; Fischer, J. C. Determination of Trace Levels of Dissolved Vanadium in Seawater by Use of Synthetic Complexing Agents and Inductively Coupled Plasma-atomic Emission Spectroscopy (ICP-AES). *Anal. Bioanal. Chem.* **2002,** *374*, 873-878.
(102) Davies, R. V.; Kennedy, J.; McIlroy, R. W.; Spence, R.; Hill, K. M. Extraction of Uranium from Sea Water. *Nature* **1964,** *203*, 1110-1115.

(103) Sadoc, A.; Messaoudi, S.; Furet, E.; Gautier, R.; Le Fur, E.; Le Polles, L.; Pivan, J. Y. Structure and Stability of VO_2^+ in Aqueous Solution: A Car-Parrinello and Static ab initio Study. *Inorg. Chem.* **2007,** *46*, 4835-4843.
(104) Tirler, A. O.; Hofer, T. S. The Structural Influence of Ca^{2+} Counter-Ions on Uranyl(VI) Tricarbonate in Aqueous Solution. *Dalton Trans.* **2016,** *45*, 4983-4988.
(105) Mehio, N.; Ivanov, A. S.; Ladshaw, A. P.; Dai, S.; Bryantsev, V. S. Theoretical Study of Oxovanadium(IV) Complexation with Formamidoximate: Implications for the Design of Uranyl-Selective Adsorbents. *Ind. Eng. Chem. Res.* **2016,** *55*, 4231-4240.
(106) Mehio, N.; Johnson, J. C.; Dai, S.; Bryantsev, V. S. Theoretical Study of the Coordination Behavior of Formate and Formamidoximate with Dioxovanadium(V) Cation: Implications for Selectivity towards Uranyl. *Phys. Chem. Chem. Phys.* **2015,** *17*, 31715-31726.
(107) Turner, D. R.; Whitfield, M.; Dickson, A. G. The Equilibrium Speciation of Dissolved Components in Fresh-Water and Seawater at 25-Degrees-C and 1 Atm Pressure. *Geochim. Cosmochim. Acta* **1981,** *45*, 855-881.
(108) Wu, F.; Qin, T.; Li, X. F.; Liu, Y.; Huang, J. H.; Wu, Z. Q.; Huang, F. First-principles Investigation of Vanadium Isotope Fractionation in Solution and during Adsorption. *Earth Planet. Sci. Lett.* **2015,** *426*, 216-224.
(109) Bühl, M.; Parrinello, M. Medium Effects on 51V NMR Chemical Shifts: A Density Functional Study. *Chem. Eur. J.* **2001,** *7*, 4487-4494.
(110) Kuo, L.-J.; Gill, G. A.; Tsouris, C.; Rao, L.; Pan, H.-B.; Wai, C. M.; Janke, C. J.; Strivens, J. E.; Wood, J. R.; Schlafer, N., et al. Temperature Dependence of Uranium and Vanadium Adsorption on Amidoxime-Based Adsorbents in Natural Seawater. *ChemistrySelect* **2018,** *3*, 843-848.